TECHNISCHE
UNIVERSITÄT
MÜNCHEN

WALTHER-MEISSNER-
INSTITUT FÜR
TIEFTEMPERATUR-
FORSCHUNG

BAYERISCHE
AKADEMIE DER
WISSENSCHAFTEN

Simultaneous Electrical and Optical Detection of Zero Effective Magnon Damping in a Magnetic Insulator

Master's thesis

Maria Sigl

Supervisor: Prof. Dr. Rudolf Gross
Advisor: Dr. Matthias Althammer
Garching – November 10, 2023

Contents

1 Introduction

With the constantly increasing amount of data, also the data storage and transport has to increase. This exponential growth of modern information technology following Moore's law has its limitations. Devices are getting smaller and smaller, reaching scales of a few nanometer, where quantum effects start to matter [1]. Further this also causes the problem of static and dynamic power consumption and heat production due to higher operational frequencies [2]. With that different approaches for information processing, storage and transport become more relevant. One promising field is the utilization and manipulation of the spin of an electron for information technologies, called spintronics [3]. We can realize this by making use of pure spin currents, carrying a spin information without any accompanied charge current and therefore dimensional down-scaling and reduction of energy dissipation via Joule heating effects is possible. For transport of spin momentum, magnons, the quantized bosonic exciations of the magnetic lattice, instead of mobile electrons can also be used. Magnons are quasiparticles with finite lifetimes and thus decay on a certain length scale which is determined by the magnetic Gilbert damping [4, 5]. To avoid spurious charge current flow and utilize low Gilbert damping, magnetic insulators are typically used for magnon-mediated spin transport. The most common material for this kind of research experiments is yttrium iron garnet ($Y_3Fe_5O_{12}$) due to its low magnetic damping properties [6], which makes it possible to realize magnon transport over long distances [7, 8]. For applicability of magnon based devices in existing and present electronic technologies it is expedient to use electrical injection and detection, where the process of the Spin Hall Effect and the inverse Spin Hall Effect can be applied [9, 10]. As an important task for the realization of spintronic devices based on magnons it is necessary to be able to further reduce and control the magnetic damping in the used material. For this spin-orbit torques in normal metal/ magnetically ordered insulator heterostructures can be used [11, 12]. Several groups already realized a control of incoherently generated magnons by applying a charge current to a normal metal on top of a magnetically ordered insulator and achieved a damping compensation above a critical current [4, 5, 13, 14]. This kind of modulation experiments is also a major part of this thesis. Here, we successfully reproduced previous measurements on YIG films grown by pulsed laser deposition with a $22\,\mathrm{nm}$ YIG thin film grown via liquid phase epitaxy for the first time in our group. These first experiments require a detailed analysis of the used samples in regards to their magnon spin transport properties as a further part of this thesis.

In regards to the control of magnon damping research utilized up to now either all-electrical magnon transport experiments or optical probing of the magnon state. On the all-electrical magnon transport side, spin transport can be analysed with respect to electrical and thermal magnon generation, varying distances between the normal metal electrodes, the impact of different magnetic field magnitudes and orientations and the temperature on the magnon decay length and we can furthermore investigate the modulation of the magnon conductivity via spin transfer torque effects in YIG [4, 7, 13, 15, 16]. As a disadvantage, we are not able to analyse the magnon population in the material with this all-electrical experimental technique. Via optical measurements for example with Brillouin Light Scattering or Raman spectroscopy we can analyse this magnon population with respect to different magnon modes, magnon density or the chemical potential [17–21]. But also this experimental technique doesn't cover all magnon related factors and we can not describe the magnon transport and its related parameters with this detection technique. As the third major part of this thesis we want to combine both methods to get a better understanding of the correlation between magnon population and magnon spin transport. To this end, we realized simultaneous optical and electrical measurements in cooperation with the AG Weiler of the RPTU Kaiserslautern. In this experiment, electrical magnon transport is conducted via lock-in detection and the magnon state is probed via microfocused Brillouin Light Scattering (BLS) measurements. Our goal is to characterize the magnon population while modulating the magnon transport via spin transfer torque. Through this scheme, we obtain a much deeper understanding of the zero effective damping state [4] by comparing the critical currents necessary to compensate magnon damping extracted from the electrical magnon transport signals and the BLS spectrum.

In the following an overview of the topics covered in this thesis is given. We start with the theoretical concepts of the electrical magnon transport in Section 2, where we cover electrical charge and spin currents and the generation process of the latter via Spin Hall Effect, followed by a description of the transport accross a normal metal/magnetically ordered insulator interface, the involved Spin Hall Magneto-resistance and the Spin Seebeck Effect. The theoretical concepts are concluded by a description of the all-electrical magnon transport and the electrical modulation of the magnon spin transport. In Section 3 we introduce the experimental details. First we describe the steps of fabrication for our LPE-YIG samples. Then the setup and the sample layout including the electrical connection of our two- and three-strip structures is described and we also explain the DC and AC detection technique we used for our all-electrical magnon transport experiments. As a final part of this section we give a short introduction into the theory of Brillouin Light Scattering (BLS) and the used microfocused BLS setup and discuss the difficulties on the realization of the sample installation. With that we can investigate the experimental results in Section 4. In the beginning we have a look at all-electrical magnon transport measurements in two-terminal YIG/Pt heterostrucues for a detailed characterization. We investigate the electrical and thermal magnon transport with regard to the dependence on the distance between the two electrode strips, the magnetic field magnitude and the temperature. Next we discuss the electrical modulation of the magnon transport signal and the zero effective damping on three-terminal structures. These measurements are also employed as a precharacterization for the in the following discussed simultaneous electrical and optical modulation measurements, where we compare the electrical magnon transport signal and the simulataneously conducted BLS signal. This part is followed by a consideration of the impact of an applied charge current and laser illumination due to the BLS measurements on the electrical magnon transport signal and the performance of our device. We further add an investigation of the magnon transport signal at high modulator currents above the critical current and the change in device performance due to that. This thesis is concluded with a short summary on the experimental results in Section 5 and an outlook on further measurements based on the results of this thesis in Section 6.

2 Theory

On the following pages the theoretical concepts for the experiments are described. We start with the definition of charge and spin currents. This is then followed up by the concepts of the Spin Hall Effect and Inverse Spin Hall Effect, the description of Spin Hall Magnetoresistance and Spin Seebeck Effect. Finally, all-electrical magnon transport and the modulation of this one are discussed.

2.1 Pure Spin Currents

For understanding all the upcoming concepts it is first of all necessary to understand electrical charge and spin currents. Moving electrons carry charge and spin information. For that, every electric charge current is also accompanied by a spin current. For a given quantization axis there are two spin eigenstates for the electron: spin-up $|\uparrow\rangle$ and spin-down $|\downarrow\rangle$. It is common to describe the charge current j_c as the sum of the charge current for electrons with spin-up $j_\uparrow$ and the charge current for electrons with spin-down $j_\downarrow$ [12]:

$$\boldsymbol{j}_c = \boldsymbol{j}_\uparrow + \boldsymbol{j}_\downarrow. \tag{1}$$

The spin current $\boldsymbol{j}_s$ on the other hand is described as:

$$\boldsymbol{j}_s = \frac{\hbar}{2e}\left(\boldsymbol{j}_\uparrow + \boldsymbol{j}_\downarrow\right), \tag{2}$$

with $\hbar$ the reduced Planck constant and e the electron charge. Futhermore the two-spin-channel model can be used to describe the simultaneously emerging spin currents. Apart from the charge current density there is now also a spin current density, which is the amount of spin that is transportet by electrons in the two-spin-channel model [22].

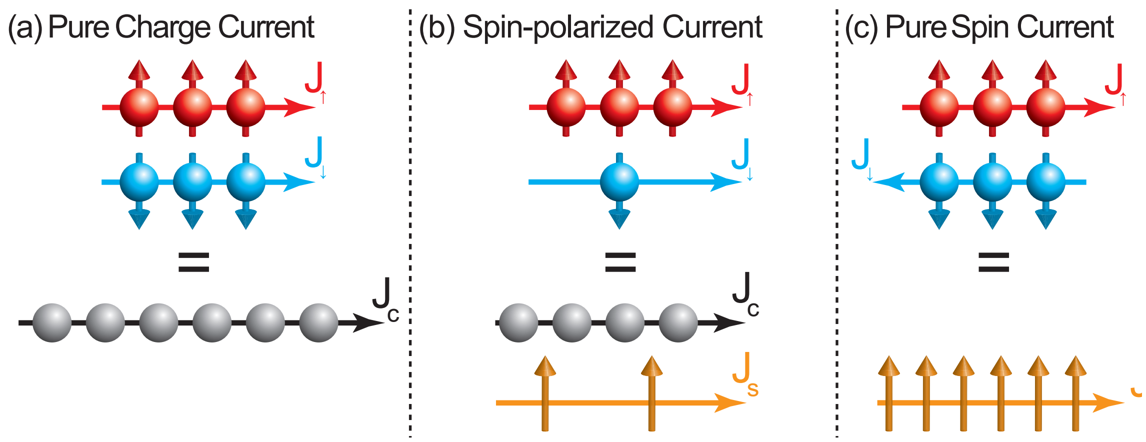

Figure 2.1: Spin and charge currents shown in the two-spin-channel model. (a) Pure charge current: Equal current densities in the same direction for both spin states. (b) Spin-polarized current: Different current densities in the same direction for the two spin states. (c) Pure spin currents: Equal current densities in different directions for the two spin states. Taken from [23]

Fig. 2.1 now shows the three different cases of electrical currents that can appear in the two-spin-channel model. In panel (a) there are two currents for electrons with spin-up and spin-down which flow in the same direction with equal current densities ($\boldsymbol{j}_\uparrow = \boldsymbol{j}_\downarrow$), this case is called a pure charge current $\boldsymbol{j}_c$, because the transported spin vanishes due to the opposite spin directions, while the transported charge of the two spin-species is summed up. This case is typically observed in normal metals with vanishing spin-orbit coupling [24]. Panel (b) shows two different current densities for the two spin states flowing in the same direction ($\boldsymbol{j}_\uparrow \neq \boldsymbol{j}_\downarrow$) and therefore a spin-polarized current, which appears in conducting ferromagnets. For two equal current densities in opposite directions for spin-up and spin-down ($\boldsymbol{j}_\uparrow = -\boldsymbol{j}_\downarrow$) in (c), we are talking about pure spin currents, where the total charge current $\boldsymbol{j}_c$ vanishes and the transported spin is finite. It is important to note here that spin currents not only have a flow direction but also a spin orientation direction of the transported spin.

2.2 Spin Hall Effect

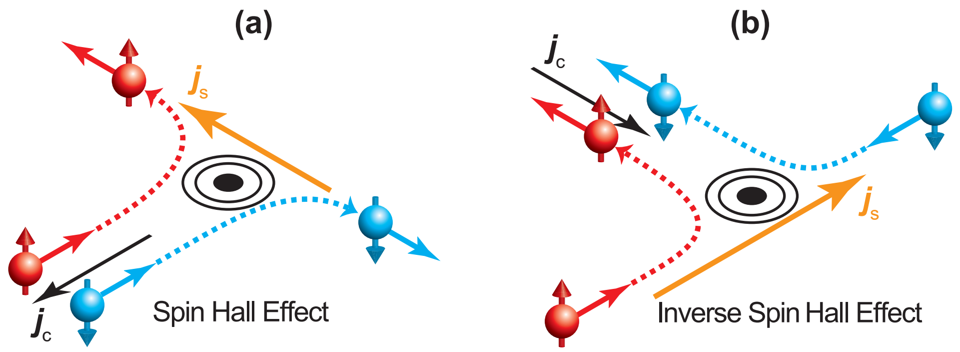

Figure 2.2: (a)The Spin Hall Effect generates pure spin currents $\boldsymbol{j}_s$ from pure charge currents $\boldsymbol{j}_c$. (b) The inverse Spin Hall Effect generates pure charge currents $\boldsymbol{j}_c$ from pure spin currents $\boldsymbol{j}_s$. Taken from Ref. [5]

For our experiments we are using pure spin currents. To generate these pure spin currents we use the Spin Hall Effect (SHE) [10, 25]. If there is a charge current in a normal metal with large spin-orbit-coupling, the electrons with spin-up and spin-down obtain spin-dependent transverse velocities [12], which arise from spin-dependent scattering events, like skew-scattering or side-jump-scattering [26–28] or from intrinsic bandstructure effects [29] (Fig. 2.2 (a)). From Section 2.1 we know that electrons with opposite spins that flow in opposite directions are defined as pure spin currents, so via the SHE we can generate pure spin currents from pure charge currents which are orthogonal to each other [12]:

$$\boldsymbol{j}_s = -\theta_{\mathrm{SH}} \left(\frac{\hbar}{2e} \right) \boldsymbol{j}_c \times \boldsymbol{s}, \tag{3}$$

where θ_{SH} describes the spin Hall angle and $\boldsymbol{s}$ the spin orientation. Fig. 2.2 (b) also shows an inverse effect which is called the Inverse Spin Hall Effect (ISHE). This effect, due to Onsager reciprocity principle [30], converts a pure spin current into a pure charge current, which can be described analougously to the pure spin current in Eq. (3) [12]:

$$\boldsymbol{j}_c = -\theta_{\mathrm{SH}} \left(\frac{\hbar}{2e} \right) \boldsymbol{j}_s \times \boldsymbol{s}. \tag{4}$$

2.3 Spin Current in Magnetically Ordered Insulator/Normal Metal heterostructures

For a normal metal (NM) thin film under an applied charge current, the SHE results in a spin accumulation at the sample edges. Attaching a magnetically ordered insulator (MOI) to the NM the pure spin current can flow accross the interface from the NM into the MOI, this interfacial spin current is given by [14, 31, 32]:

$$\boldsymbol{j}_{\mathrm{s,int}} = \frac{1}{4\pi}\left(\frac{h}{e^2}G_{\mathrm{i}} + \frac{h}{e^2}G_{\mathrm{r}}\boldsymbol{m}\times\right)\mu_s\left(0\right)\boldsymbol{s}\times\boldsymbol{m} + g\mu_s\left(0\right)\left(\boldsymbol{s}\cdot\boldsymbol{m}\right)\boldsymbol{m}, \tag{5}$$

with G_{r} and G_{i} the real and imaginary part of the spin mixing conductance G, μ_{s} the spin-dependent chemical potential parametrizing the electron spin accumulation in the NM, $\mathbf{m} = \frac{\mathbf{M}}{|\mathbf{M}|}$ the direction of the magnetization $\mathbf{M}$ in the MOI and g the spin conductance.

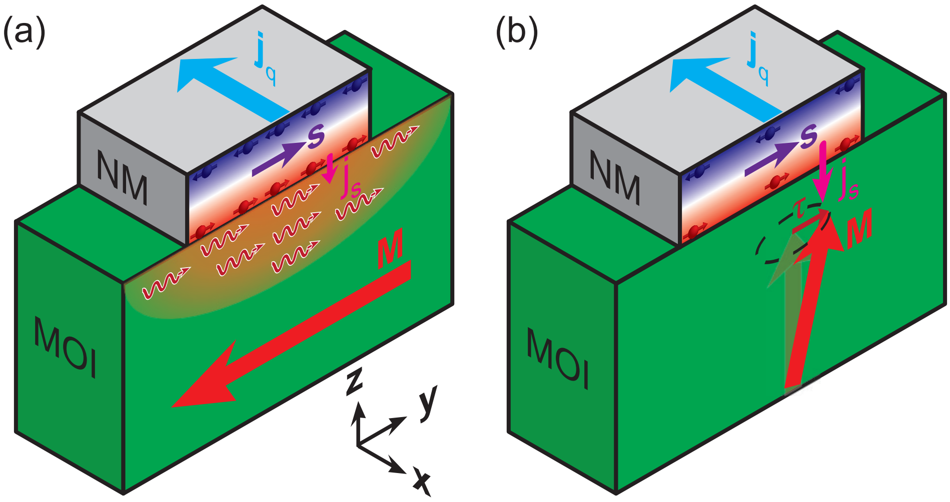

Figure 2.3: Underlying concepts of SMR. (a) Magnetization **M** in the MOI and spin orientation **S** are parallel to each other which results in an magnon accumulation at the interface. (b) Magnetization **M** in the MOI and spin orientation **S** are perpendicular to each other which results in an exerted spin transfer torque in the MOI. Taken from Ref. [12].

Fig. 2.3 shows the two cases that can be observed for a MOI/NM heterostructure. In panel (a) the magnetization $\boldsymbol{M}$ in the MOI is oriented parallel to the spin orientation $\boldsymbol{S}$ in the NM, in (b) the magnetization $\boldsymbol{M}$ in the MOI is perpendicular to the spin orientation $\boldsymbol{S}$ in the NM. For the parallel case $\boldsymbol{S} \parallel \boldsymbol{M}$, the first part of Eq. (5) is vanishing and the second term is finite. There is a small spin current across the interface and therefore magnons accumulate in the interface. For $\boldsymbol{S} \perp \boldsymbol{M}$ we find a finite spin current flowing across the interface due to G [12]. The Spin Polarization $\boldsymbol{S}$ exerts a spin transfer torque across the interface onto $\boldsymbol{M}$. For both magnetization orientations with respect to $\boldsymbol{S}$, the parallel and the perpendicular case, the resistance can be measured, we get $R_{\parallel} < R_{\perp}$. So the resistance changes with the orientation of the magnetization $\boldsymbol{M}$ according to the spin orientation $\boldsymbol{S}$. This is called the Spin Hall Magneto resistance (SMR) [33], this value is proportional to the spin diffusion length. The SMR is used in this thesis for precharacterization and to compare measured structures. The resistance of the NM thin film is given by [34, 35]:

$$R = R_0 + \triangle R(1 - m_{\mathrm{t}}^2), \tag{6}$$

where R_0 is the intrinsic electric resistivity of the NM, $\triangle R = R_{\|} - R_{\perp}$ and m_{t} is the projection of the magnetization direction onto t, which is the transverse of the current direction $\boldsymbol{j}$. For m_{t} we observe a $\cos$ dependence of the angle φ between the magnetization $\boldsymbol{M}$ in the MOI and the spin orientation in the NM, so also the resistance as a function of the angle φ is expected to show a $cos^2\varphi$ dependence [34]. For the SMR we can also use the following expression [34]:

$$SMR = \frac{\triangle\rho}{\rho_0} = -\frac{2\theta_{\mathrm{SH}}\lambda_{\mathrm{sd}}^2 \frac{\rho(t,T)}{t} G_{\mathrm{r}} \tanh\left(\frac{t}{2\lambda_{\mathrm{sd}}}\right)}{1 + 2\lambda_{\mathrm{sd}}\rho\left(t,T\right) G_{\mathrm{r}} \coth\left(\frac{t}{\lambda_{\mathrm{sd}}}\right)}, \tag{7}$$

with λ_{sd} the spin diffusion length of the NM and t the thickness of the NM. This expression allows to estimate G from measurements of the SMR if we assume certain values for θ_{SH} and λ_{sd}.

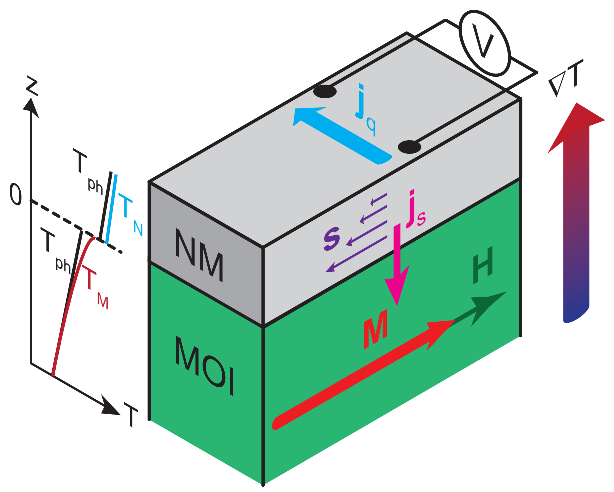

Figure 2.4: Illustration of the Spin Seebeck Effect: The Joule heating associated to an applied charge current, leads to an increase of temperature in the NM and therefore also in the MOI. This temperature gradient causes a pure spin current across the interface. Taken from Ref. [12].

Due to a finite resistance of the NM, an applied charge current results in a Joule heating of the NM. This increased temperature in the NM also causes an increase of temperature in the MOI. Fig. 2.4 shows this process. This temperature gradient between the NM and the MOI causes a pure spin current across the interface [12]. We now have a thermal generation of magnons that is independent of the orientation between $\boldsymbol{M}$ and $\boldsymbol{S}$, it only matters the orientation of the magnetization $\boldsymbol{M}$ in the MOI. This phenomenon is called the Spin Seebeck Effect (SSE) [36, 37]. The charge current can still be described by Eq. (1) and the signal which corresponds from the SSE has a $\cos\varphi$ dependence [12]. For our in Section 3 explained measurements we then get two signals: An electrical signal with magnons caused by the SHE and a thermal signal with magnons caused by the SSE.

2.4 All-electrical magnon transport

Now we understand the important effects and concepts we need for our upcoming experiments. Let's now have a look at how we can make use of it in the magnon transport measurements. Fig. 2.5 shows the structure. For magnon transport experiments, we need two NM strips, which is Platinum (Pt) in our case. These NM strips are attached to a MOI, which is Yttrium Iron Garnet $Y_3Fe_5O_{12}$ (YIG) in our case. We then generate magnons via the SHE and detect magnons via the ISHE at the two strips. We apply a charge current at the first NM-strip, which we call the injector, we then get a spin accumulation at the transverse edges due to the SHE. For the parallel alignment of the magnetization in the MOI and the spin orientation in the NM, $\boldsymbol{M} \parallel \boldsymbol{S}$, there is a non-equilibrium state in the magnonic system [12, 38]. We obtain a magnon accumulation and the magnons diffuse into the MOI, this is driven by the gradient of the magnon chemical potential. When the magnons in the MOI arrive at the second NM-strip, which is called the detector, the magnons inject a spin current into it and this spin current is measureable as an open circuit voltage via the ISHE. For the perpendicular case, $\mathbf{M} \perp \mathbf{S}$, there is no detectable magnon transport signal [38]. It is important to note that the magnon number is not a conserved quantity and magnons exhibit a finite magnon lifetime. This leads to the fact that the spin transport via magnons exhibits a chracteristic magnon decay length, which can be extracted in the experiment by varying the distance between injector and detector strip.

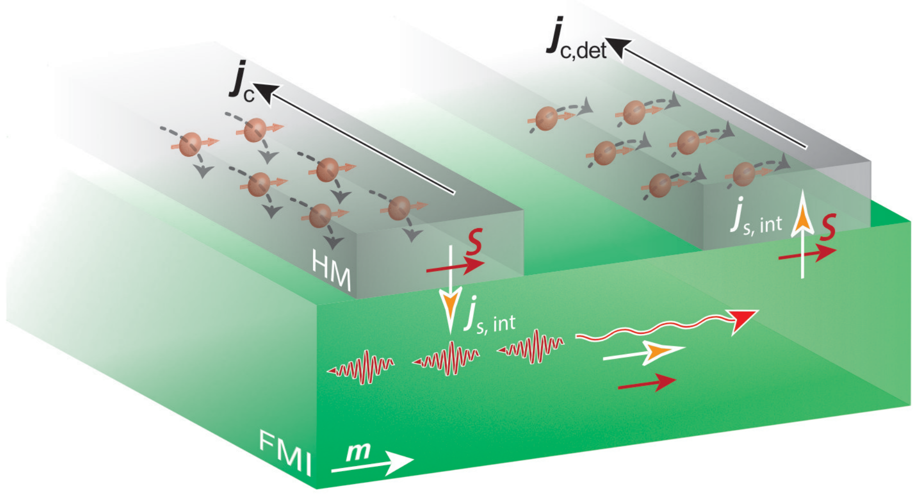

Figure 2.5: Magnon transport in a NM/MOI heterostructure: Magnon generation via the SHE at the first NM-strip (injector) and magnon detection via the ISHE at the second NM-strip (detector). Taken and edited from Ref. [5].

2.5 Electrical modulation of magnon spin transport

In this thesis we not only want to measure simple magnon transport like described in the previous Section 2.4, we also want to modulate this magnon transport. Manipulation of spin currents is an important task for information transport [39, 40]. For that we need a third Pt-strip in the middle of the injector and detector, which is called the modulator. On that strip we can apply an additional DC-charge current and can then control the transport signal, which was first demonstrated by Cornelissen et al. [13]. In the following we introduce the concept of damping compensation, for more details see Ref. [11, 14, 41, 42]. We get an auto-oscillation of the magnetization $\boldsymbol{m}$ in the MOI if intrinsic damping described by the magnon relaxation rate Γ_{mr} is balanced by the spin transfer torque $\Gamma_{\mathrm{ST}} \propto I_{\mathrm{mod}}$ due to spin injection via SHE. The magnon relaxation rate can be written as [14]:

$$\Gamma_{\mathrm{mr}} = \alpha\gamma\mu_0 \left(H + \frac{M_{\mathrm{eff}}}{2} \left(N_{\mathrm{x}} + N_{\mathrm{y}} - 2N_{\mathrm{z}}\right) \right), \tag{8}$$

with the total magnetic damping constant α, the gyromagnetic ratio $\gamma = \frac{g\mu_{\mathrm{B}}}{\hbar}$ (where g is the Landé factor, μ_{B} the Bohr's magneton and μ_0 the vacuum permeability), the external magnetic field H, the effective magnetization M_{eff} in the MOI and the geometry-dependent demagnetization factors N_{x}, N_{y}, N_{z}. We can define the out-of-plane and in-plane magnon relaxation rates using $\alpha = \alpha_{\mathrm{G}} + \alpha_{\mathrm{sp}}$ (with the intrinsic Gilber damping α_{G} and the spin pumping induced Gilbert damping α_{sp} [43, 44] as the MOI is interfaced with a NM). For the out-of-plane magnetized thin film along z ($N_{\mathrm{x}} = N_{\mathrm{y}} = 0$, $N_{\mathrm{z}} = 1$ we can write:

$$\Gamma_{\mathrm{mr}}^{\mathrm{oop}} = \left(\alpha_{\mathrm{G}} + \alpha_{\mathrm{sp}}\right) \gamma\mu_0 \left(H - M_{\mathrm{eff}}\right), \tag{9}$$

and for the in-plane magnetized thin film in x-y-plane ($N_{\mathrm{x}} + N_{\mathrm{y}} = 1$, $N_{\mathrm{z}} = 0$):

$$\Gamma_{\mathrm{mr}}^{\mathrm{ip}} = \left(\alpha_{\mathrm{G}} + \alpha_{\mathrm{sp}}\right) \gamma\mu_0 \left(H + \frac{M_{\mathrm{eff}}}{2}\right). \tag{10}$$

For our measurements we focus on in-plane magnetized thin films. Further we need the ferromagnetic resonance (FMR) frequency from the Kittel formula for an in-plane magnetized film:

$$\omega_{\mathrm{FMR}}^{\mathrm{ip}}\left(H\right) = \gamma\mu_0 \sqrt{H\left(H + M_{\mathrm{eff}}\right)}. \tag{11}$$

Taking into account the inhomogeneous broadening δH of the FMR linewidth, we define the effective damping parameter as [14]:

$$\alpha_{\mathrm{eff}} = \alpha_{\mathrm{G}} + \gamma\mu_0 \frac{\delta H}{2\omega_{\mathrm{FMR}}^{\mathrm{ip}}}. \tag{12}$$

With that Eq. (10) can be written as [14, 42]:

$$\Gamma_{\mathrm{mr}}^{\mathrm{ip}} = \left(\alpha_{\mathrm{sp}} + \alpha_{\mathrm{G}} + \frac{\delta H}{2\sqrt{H\left(H + M_{\mathrm{eff}}\right)}} \right) \gamma\mu_0 \left(H + \frac{M_{\mathrm{eff}}}{2}\right), \tag{13}$$

for the MOI thin film. Due to the inhomogeneous broadening, $\Gamma_{\mathrm{mr}}^{\mathrm{ip}}$ diverges at $H = 0$ for a finite M_{eff}. Furthermore to include the finite spin transparency of the MOI/NM interface is the spin pumping contribution given as $\alpha_{\mathrm{sp}} = g_{\mathrm{eff}} \frac{\hbar\gamma}{4\pi M_{\mathrm{s}} t_{\mathrm{MOI}}}$ with the saturation magnetization M_{s}, the thickness t_{MOI} of the MOI and the effective spin mixing conductance $g_{\mathrm{eff}} = \left(g^{\uparrow\downarrow} \frac{h}{2e^2} \frac{\sigma_{\mathrm{NM}}}{\lambda_{\mathrm{m}}}\right) / \left(g^{\uparrow\downarrow} + \frac{h}{2e^2} \frac{\sigma_{\mathrm{NM}}}{\lambda_{\mathrm{m}}}\right)$ ($g^{\uparrow\downarrow}$ is the normal spin mixing conductance). For zero effective damping $\Gamma_{\mathrm{mr}}^{\mathrm{ip}} = \Gamma_{\mathrm{ST}}$ has to be fulfilled. The applied DC-current at the NM modulator I_{mod} excites a spin chemical potential μ_{s} below the electrode due to the SHE which exerts a spin-transfer torque Γ_{ST} on the magnon modes and thermal fluctuations of the magnetization $\boldsymbol{m}$ in the MOI. This anti-damping spin torque rate can be written in the macrospin approximation [14, 42]:

$$\Gamma_{\mathrm{ST}} = \frac{\hbar}{2e}\frac{\gamma}{M_{\mathrm{S}} t_{\mathrm{MOI}} t_{\mathrm{NM}} w_{\mathrm{NM}}} \cdot T \cdot \theta_{\mathrm{SH}} I_{\mathrm{mod}}, \tag{14}$$

with t_{NM}, w_{NM} and θ_{SH} thickness, width and spin Hall angle of the NM, while the interface spin transparency for spin currents is described by T:

$$T = \frac{g^{\uparrow\downarrow}\tanh\eta}{g^{\uparrow\downarrow}\coth(2\eta) + \frac{h}{2e^2}\frac{\sigma_{\mathrm{NM}}}{\lambda_{\mathrm{NM}}}}, \tag{15}$$

with $\eta = \frac{t_{\mathrm{NM}}}{2\lambda_{\mathrm{m}}}$ and σ_{NM} the conductivity of the NM [14, 45]. The anti-damping spin torque rate exactly cancels the intrinsic magnetic damping $\Gamma_{\mathrm{ST}} = \Gamma_{\mathrm{mr}}^{\mathrm{ip}}$ at the critical current I_{crit}, which can then be written as:

$$I_{\mathrm{crit}} = \frac{\hbar}{e}\frac{\sigma_{\mathrm{NM}}}{2\lambda_{\mathrm{m}}}\frac{t_{\mathrm{NM}} w_{\mathrm{NM}}}{\theta_{\mathrm{SH}}\tanh\eta}\left(1 + 4\pi M_{\mathrm{s}} t_{\mathrm{MOI}}\frac{\alpha_{\mathrm{eff}}}{\hbar\gamma g_{\mathrm{eff}}}\right)\gamma\mu_0\left(H + \frac{M_{\mathrm{eff}}}{2}\right). \tag{16}$$

Thus, we expect a chracteristic magnetic field-dependence of I_{crit}. For $H \to 0$, I_{crit} diverges to large values, while at large magnetic fields we expect a linear dependence of I_{crit} on H. After deriving the critical current I_{crit} at which damping compensation occurs, we now discuss the influence of an applied modulator current on the diffusive magnon transport from injector to detector as introduced in Section 2.4. Thus we first take a look on the change in the magnon conductivity σ_{m} in the MOI due to the applied charge current at the modulator. The magnon conductivity in the limit of short distances between injector and detector as compared to the magnon decay length is given as [4, 5]:

$$\sigma_{\mathrm{m}} = \frac{3\hbar n_{\mathrm{m}}\tau_{\mathrm{m}}}{m_{\mathrm{m}}}, \tag{17}$$

where m_{m} is the effective magnon mass, n_{m} the magnon density and τ_{m} the magnon relaxation time. The magnon density and the magnon relaxation time can be changed via the additionally applied charge current to the modulator [13, 46]. Due to the charge current we get a finite spin chemical potential μ_{s}^{0} at the NM/MOI interface caused by the SHE which leads to an interfacial pure spin current of:

$$\boldsymbol{j}_{\mathrm{s,int}}^{\mathrm{z}} = \left[g\left(\mu_{\mathrm{m}}^{0} - \mu_{\mathrm{s}}^{0}\boldsymbol{s}\cdot\boldsymbol{m}\right) + S\delta T\right]\boldsymbol{m}, \tag{18}$$

with μ_{m}^{0} the magnon chemical potential, introduced in the equlibrium Bose-Einstein distribution [31, 38], $\boldsymbol{m}$ the unit vector of the magnetization in the MOI and δT the interfacial temperature difference between electrons and magnons. From the spin diffusion equations we can obtain the magnon chemical potential polarized along $\boldsymbol{m}$, for parallel orientation $\boldsymbol{s}\cdot\boldsymbol{m} = +1$ and antiparallel orientation $\boldsymbol{s}\cdot\boldsymbol{m} = -1$ (for detailed calculation for the following equations see [5]):

$$\mu_{\mathrm{m}}^{\pm}(z) = \frac{\left(\pm g j_{\mathrm{s}}^{\mathrm{SH}}\left(\delta_{\mathrm{ms}} - \lambda_{\mathrm{m}} l_{\mathrm{s}}\right) - \alpha_{\mathrm{ms}} S\delta T\right)\left(e^{-z/\lambda_{\mathrm{m}}} + e^{\eta_{\mathrm{m}}} e^{z/\lambda_{\mathrm{m}}}\right)}{g\alpha_{\mathrm{ms}}\left(e^{\eta_{\mathrm{m}}} + 1\right) + g\beta_{\mathrm{ms}}\left(e^{\eta_{\mathrm{m}}} - 1\right) + \gamma_{\mathrm{ms}}\left(e^{\eta_{\mathrm{m}}} - 1\right)}, \tag{19}$$

where $j_s^{SH} = \frac{\hbar}{2e}\theta_{SH} j_{mod}$ is the SHE induced spin current, λ_m the magnon decay length, λ_{sd} the spin diffusion length. The following parameters are defined furthermore:

$$\eta_m = \frac{2t_{MOI}}{\lambda_m}, \tag{20}$$

$$\eta = \frac{t_{NM}}{2l_s}, \tag{21}$$

$$\alpha_{ms} = \lambda_m \sigma_s \sinh(2\eta), \tag{22}$$

$$\beta_{ms} = \sigma_m l_s \cosh(2\eta), \tag{23}$$

$$\gamma_{ms} = \sigma_m \sigma_s \sinh(2\eta), \tag{24}$$

$$\delta_{ms} = \lambda_m l_s \cosh(2\eta). \tag{25}$$

We are especially interested in the average magnon chemical potential $\langle \mu_m^{\pm} \rangle = t_{MOI}^{-1} \int_{-t_{MOI}}^{0} \mu_m^{\pm}(z)\, dz$. With the approximation $e^{\eta_m} = 1$ and $\frac{\lambda_m}{t_{MOI}} \sinh\left(\frac{t_{MOI}}{\lambda_m}\right) \approx 1$ for $\frac{t_{MOI}}{\lambda_m} << 1$ and the fact that the temperature difference δT is proportional to the Joule heating power and therefore $\delta T = -c I_{mod}^2$ with a conversion factor c, we can express $\langle \mu_m^{\pm} \rangle$ as a function of the applied charge current at the modulator strip I_{mod}:

$$\langle \mu_m^{\pm} \rangle (I_{mod}) = \pm \frac{e\varphi l_s \tanh(\eta)}{\sigma_e t_{NM} w_{NM}} I_{mod} + \frac{S}{g} c I_{mod}^2. \tag{26}$$

Shown that the magnon chemical potential has a linear and quadratic contribution in I_{mod} [5, 7, 13], we can now have a look at the non-equilibrium magnon density n_m [5]:

$$n_m(\langle \mu_m^{\pm} \rangle, T) = \int_0^{\infty} d\epsilon_m g(\epsilon_m) n_B(\epsilon_m, \langle \mu_m^{\pm} \rangle, T) = n_m^0 + \frac{\zeta(1/2)}{\Lambda^3 k_B T} \langle \mu_m^{\pm} \rangle = n_m^0 + \Delta n_m, \tag{27}$$

where $n_m^0 = \zeta(3/2)\Lambda^{-3}$ is the magnon density in thermal equilibrium and $\Delta n_m = \frac{\rho_m}{\hbar}$ is the non-equilibrium magnon number density with $\rho_m = \hbar \frac{\zeta(1/2)}{\Lambda^3 k_B T} \mu_m$. With that we know, that the magnon density n_m is dependent on the finite magnon chemical potential μ_m and therefore $n_m \propto I_{mod} + I_{mod}^2$ which means we can influence the magnon chemical potential as well as the magnon density via the applied charge current at the modulator I_{mod} [7, 38]. With that we can write the magnon conductivity in linear response as [5, 13]:

$$\begin{aligned} \sigma_m &= 3\hbar \frac{n_m \tau_m}{m_m} = 3\hbar \frac{\tau_m}{m_m}\left(n_m^0 + \Delta n_m\right) \\ &= 3\hbar \frac{\tau_m}{m_m} + \left(n_m^0 + \frac{\zeta(1/2)}{\Lambda^3 k_B T}\left(\pm \frac{e\varphi l_s \tanh(\eta)}{\sigma_e t_{NM} w_{NM}} I_{mod} + \frac{S}{g} c I_{mod}^2\right)\right) \\ &= \sigma_m^0 \pm \Delta\sigma_{el} I_{mod} + \Delta\sigma_{th} I_{mod}^2, \end{aligned} \tag{28}$$

with σ_m^0 the magnon conductivity in thermal equilibrium, $\Delta\sigma_{el}$ the SHE induced magnon conductivity change and $\Delta\sigma_{th}$ the thermally induced magnon conductivity change. Thus the magnon conductivity is dependent of the charge current at the modulator. The description above fits good for a low bias regime with the magnon chemical potential μ_m below the magnon gap [13]. For other cases we have to include the magnon relaxation time, for that we assume the magnon relaxation time as the inverse of the difference of the damping rate and the spin torque rate for the case that we generate a magnon accumulation underneath the modulator [5] $\tau_{\mathrm{m}} = (\Gamma_{\mathrm{D}} - \Gamma_{\mathrm{ST}})^{-1}$. For constant magnon density n_{m} the magnon conductivity can now be written as:

$$\sigma_{\mathrm{m}} = 3\hbar \frac{n_{\mathrm{m}}}{m_{\mathrm{m}}} (\Gamma_{\mathrm{D}} - \Gamma_{\mathrm{ST}})^{-1} = 3\hbar \frac{n_{\mathrm{m}} \tau_{\mathrm{m}}^{0}}{m_{\mathrm{m}}} \left(1 - \frac{I_{\mathrm{mod}}}{I_{\mathrm{crit}}}\right)^{-1}, \tag{29}$$

with the equilibrium magnon relaxation time $\tau_{\mathrm{m}}^{0} = \frac{1}{\Gamma_{\mathrm{D}}}$. We furthermore defined $\frac{\Gamma_{\mathrm{ST}}}{\Gamma_{\mathrm{D}}} = \frac{I_{\mathrm{mod}}}{I_{\mathrm{Icrit}}}$, which means that for $I_{\mathrm{mod}} \to I_{\mathrm{crit}}$ the magnon conductivity as well as the magnon relaxation time diverges. Due to Ref. [5, 46] the magnon conductivity near I_{crit} for high temperatures close to room temperature or higher can also be written as:

$$\sigma_{\mathrm{m}} = \sigma_{\mathrm{m}}^{0} \left(1 - \frac{I_{\mathrm{mod}}}{I_{\mathrm{crit}}}\right)^{-\frac{1}{2}} + \Delta\sigma_{\mathrm{th}} I_{\mathrm{mod}}^{2}, \tag{30}$$

where the thermally via Joule heating induced quadratic magnon injection is included. We now have two expressions for the modulation of the magnon conductivity due to spin injection that can be separated due to the linear response regime. For the low current bias regime the modulation can be described via Eq. (28), where the linear response is fulfilled. For the non-linear regime with large electrical pumping we need an infinite τ_{m} to describe the divergence of the magnon conductivity via Eq. (30).

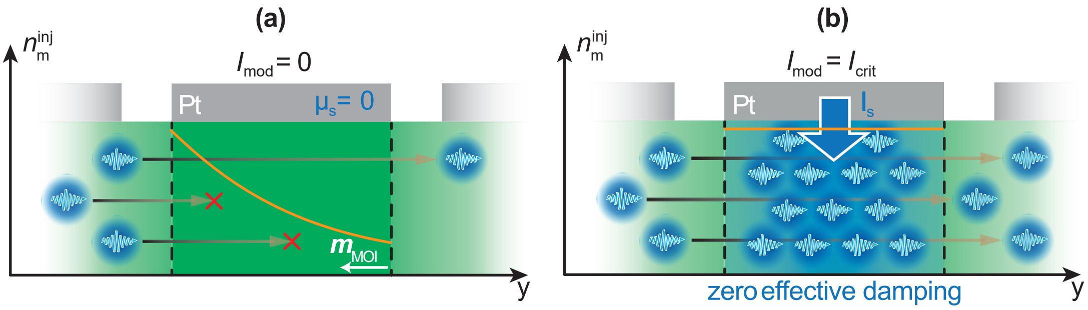

Figure 2.6: Transport for a three-strip structure, with focus on what happens beneath the modulator. (a) For $I_{\mathrm{dc}} = 0\,\mu\mathrm{A}$ Magnons diffuse to the left side. Magnon decay (red crosses) results in a spin diffusion length shown as an exponential decay of the magnon density (orange line) (b) For $I_{\mathrm{dc}} = I_{\mathrm{crit}}$ the threshold current for the damping compensation is reached, magnon accumulation beneath the modulator leads to zero effective damping state. Taken and adapted from [4].

We can now have a look at the physical representation of the device shown in Fig. 2.6 reduced to the picture beneath the modulator electrode. Panel (a) shows the case for $I_{\mathrm{dc}} = 0\,\mu\mathrm{A}$: No DC-charge current is applied at the middle strip and the density of the injected magnons from the injector $n_{\mathrm{m}}^{\mathrm{inj}}$ decays exponentially (orange line) and only a fraction of the injected magnons can be detected at the detector. If the DC-charge current is increased up to a critical current $I_{\mathrm{dc}} = I_{\mathrm{crit}}$ the threshold current for the damping compensation is reached, see panel (b). The modulator injects further magnons, so that the magnon lifetime diverges and we have a transport with effectively vanishing magnon decay that can be described via Eq. (29). This state can be called the zero effective damping state [4].

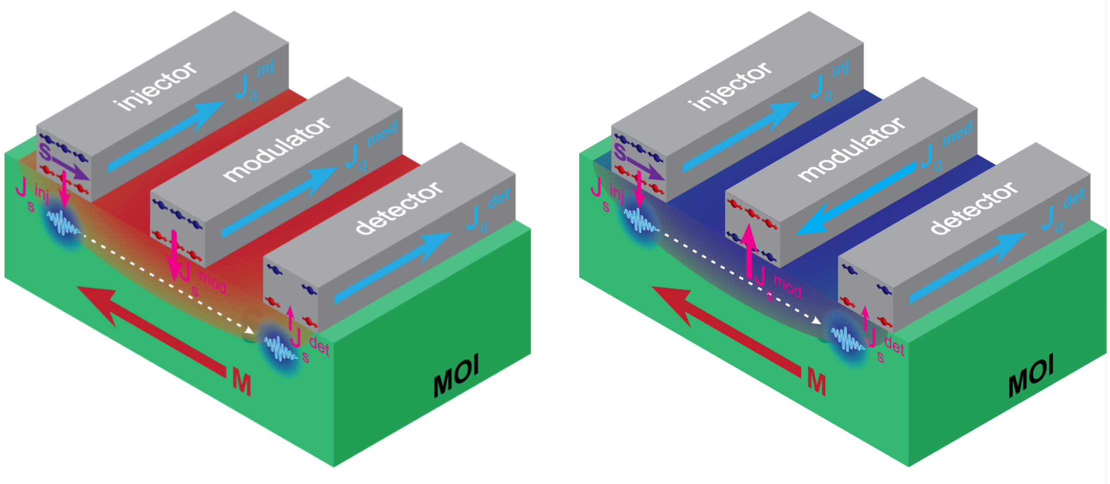

Figure 2.7: Magnon transport modulation for (a) $I_{\mathrm{mod}} > 0\,\mu\mathrm{A}$ and $\varphi = \pm 180°$. Due to the parallel alignment between the magnetization $\boldsymbol{m}$ and the spin polarization $\boldsymbol{s}$ there is an magnon accumulation beneath the modulator and therefore an increased transport signal. (b)Magnon transport modulation for $I_{\mathrm{mod}} < 0\,\mu\mathrm{A}$ and $\varphi = \pm 180°$. Due to the antiparallel alignment between the magnetization m and the spin polarization s there is an reduced magnon density beneath the modulator and therefore an decreased transport signal which is counterbalanced by thermal effects.

Applying a DC-charge current at the modulator electrode influences the magnon conductivity and therefore the magnon transport signal we can detect at the detector. Fig. 2.7 shows what happens for applying positive and negative modulator currents I_{mod} apart from the critical current. In panel (a) we have a positive charge current at the modulator $I_{\mathrm{mod}} > 0\,\mu\mathrm{A}$ and an angle $\varphi = \pm 180°$ which means for the orientation in the external magnetic field: $\boldsymbol{H} \perp I_{\mathrm{inj}}$. Here the relative orientation of the spin polarization $\boldsymbol{s}$ at the interface and the magnetization direction $\boldsymbol{m}_{\mathrm{YIG}}$ is parallel. For this configuration we would expect a maximum of the detected signal either way [7, 40]. That results in a magnon accumulation underneath the modulator, therefore an increased magnon density and we get a larger signal at the detector. For the same orientation but negative current at the moduator $I_{\mathrm{mod}} < 0\,\mu\mathrm{A}$ in panel (b), we have the $180°$ shifted case. The spin polarization $\boldsymbol{s}$ is now antiparallel to the magnetization $\boldsymbol{m}_{\mathrm{YIG}}$, we then have a magnon depletion and decreased magnon density which results in a smaller signal. In Section 4.2 we see that the expected depletion can not be seen because it is counter balanced by thermally injected magnons, that are present due to Joule heating in the modulator.

3 Experimental details

In this section the experimental details are described. We start with the steps of fabrication and the dimensions of the used samples (see Section 3.1). Afterwards the used measurement setup and techniques are described. We conducted measurements on two- and three-strip structures using DC current reversal method and AC lock-in detection method to extract the electrical and thermal magnon transport signal from the detected voltage (see Section 3.2). Finally we describe the basic concepts of Brillouin Light Scattering (BLS) and the used micro-BLS setup (see Section 3.3).

3.1 Sample Fabrication

The $Y_3Fe_5O_{12}$ (YIG) thin films investigated in this thesis are grown via Liquid Phase Epitaxy (LPE) on top of a Gadolinium-Gallium-Garnett (GGG) substrate. The films with a thickness of $t_{\mathrm{YIG}} = 22\,\mathrm{nm}$ were provided by Carsten Dubbs from Innovent. We structure the two- and three-terminal YIG/Pt heterostructures consisting of two and three parallel Pt-strips via electron beam lithography (EBL) and *DC-Magnetron* sputtering of Pt with a subsequent lift-off process. The different fabrication steps are shown in Fig. 3.1.

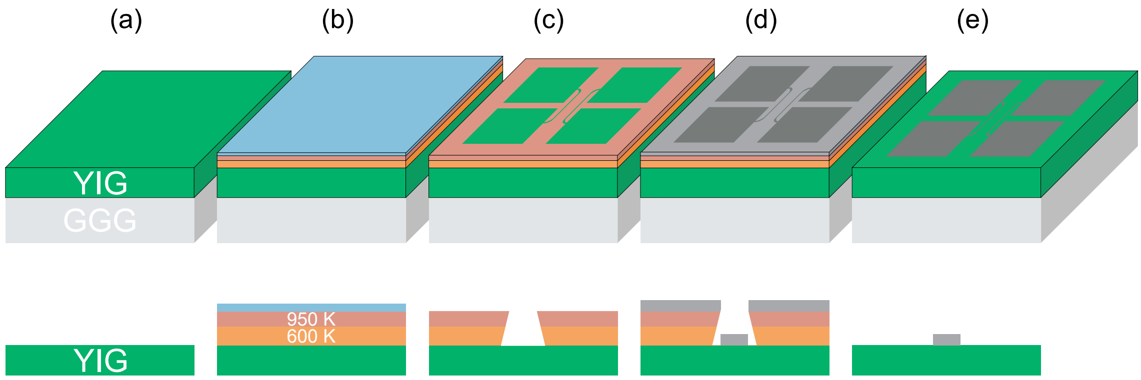

Figure 3.1: Steps of the fabrication process: (a) Cleaned substrate. (b) Spin coated substrate with *AR-600K*, *AR-950K* and a conductive resist (blue). (c) Sample after electron beam lithography. (d) Sputtered sample. (e) Final sample with structure after lift-off. Taken and adapted from [32].

Panel (a) shows the $4\,\mathrm{mm} \times 7\,\mathrm{mm}$ GGG-substrate and the $22\,\mathrm{nm}$ thin LPE-YIG film, which is in a first step cleaned from organic residues with acetone and isopropanol in an ultrasonic bath and a subsequent treatment to ensure a good interface quality, in piranha solution (concentrated H_2SO_4 mixed with $30\,\%$ H_2O_2 by volume). Then the substrate is spincoated with three layers of resist shown in Fig. 3.1(b): First $9\,\mathrm{\mu L}$ of *AR-600K* at $4000\,\mathrm{rpm}$ for $1\,\mathrm{min}$, baked out for $5\,\mathrm{min}$ at $170\,^{\circ}\mathrm{C}$, second $9\,\mathrm{\mu L}$ of *AR-950K* at $4000\,\mathrm{rpm}$ for $1\,\mathrm{min}$, baked out for $5\,\mathrm{min}$ at $170\,^{\circ}\mathrm{C}$ and at last $20\,\mathrm{\mu L}$ of a conductive resist *PMMA-Electra 92* at $4000\,\mathrm{rpm}$ for $1\,\mathrm{min}$, baked out for $2\,\mathrm{min}$ at $90\,^{\circ}\mathrm{C}$. Due to the insulating nature of YIG and the GGG substrate we need the layer of conductive resist to prevent charge accumulations on the surface that can distort the electron beam. The EBL is done using a *NanoBeam nb5* lithography system. After the lithography step the conductive resist is removed in deionized water. The remaining resist is then developed in *AR 600-56* for $2\,\mathrm{min}$. The resist stack is a positive resist. Hence the resist area exposed by the electron beam is removed by the developer as shown in panel (c). In a next step $t_{\mathrm{Pt}} = 7\,\mathrm{nm}$ thin layers of polycristalline Pt is sputtered on top using a *DC-Magnetron* sputtering system as shown in panel (d). In a last step we perform a lift-off to remove the remaining resist and the excessive sputtered material. To this end the sample is put into hot acetone at $70\,^{\circ}\mathrm{C}$ for several times and subsequently into the ultra sonic bath for a few seconds at lowest power. Fig. 3.1 (e) shows the final structure. We repeat this process two times: in the first iteration we structure the Pt-strips and in the second iteration we fabricate the Aluminium pads that are used as contact pads for the electrical contacting via wire bonding.

3.2 Setup and Measurement techniques

On the following pages we want to take a look at the actual sample layout and techniques we used for the measurements. We start with the setup for the two-terminal structures and afterwards we describe the sample and layout for the three-terminal structures.

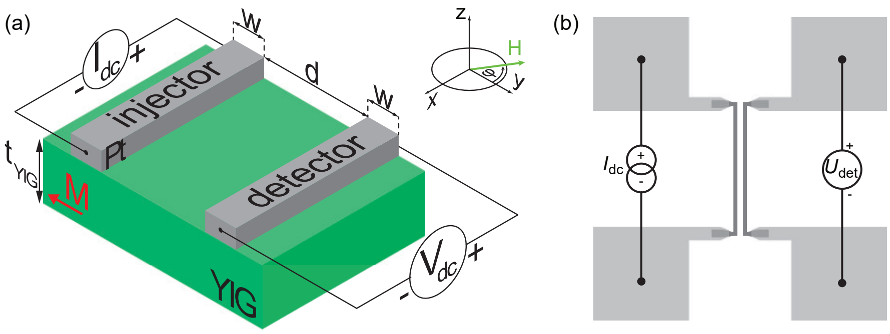

Figure 3.2: Schematic structure of electrical connection of the two-terminal device and the coordinate system for the rotation angle φ of the magnetic field $\mu_0 H$. Two Pt-strips with width $w = 500\,\mathrm{nm}$ are on top of the YIG sample ($t_{\mathrm{YIG}} = 22\,\mathrm{nm}$) with an edge-to-edge distance d. Taken and adapted from [15].

The typical structure to perform all-electrical magnon transport experiments in a two-terminal structure is shown in Fig. 3.2(a). We apply a charge current at the left electrode which we refer to as the injector. Due to the SHE and Joule heating, magnons are injected into the YIG thin film and diffuse towards the detector where they are converted into a measurable voltage signal via the ISHE in an open circuit condition (see Section 2.4). The length and width of the injector and the detector are fixed during this thesis to $l_{\mathrm{inj/det}} = 100\,\mu\mathrm{m}$ and $w = 500\,\mathrm{nm}$ respectively. The distance between the injector and detector electrode d is varied between different structures from $d = 900\,\mathrm{nm}$ up to $d = 3.5\,\mu\mathrm{m}$. For three-terminal structures an additional modulator strip with a width of w_{m} is centered between injector and detector electrode as shown in Fig. 3.3(a). The modulator strip has a length of $l_{\mathrm{mod}} = 120\,\mu\mathrm{m}$ and different widths w_{m}.

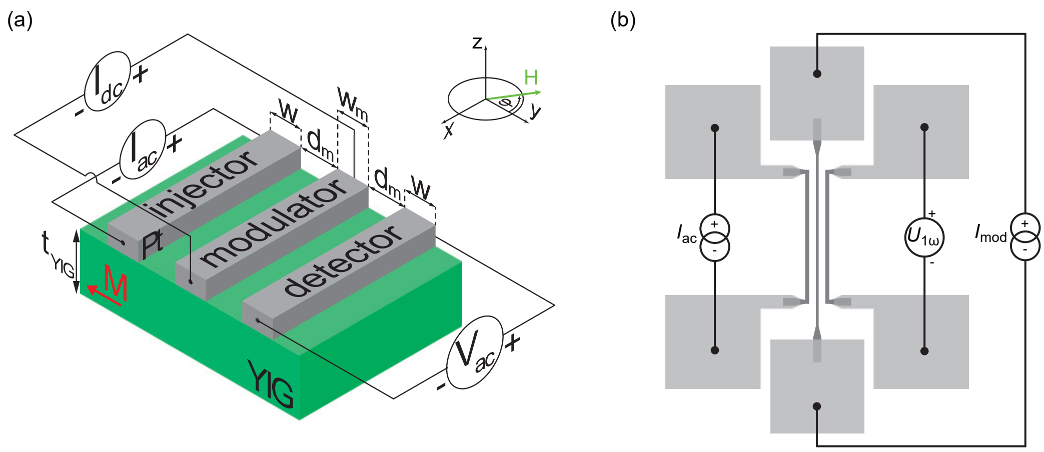

Figure 3.3: Schematic structure of electrical connection of the three-terminal device and coordinate system for the rotation angle φ of the magnetic field $\mu_0 H$. Two Pt-strips with width $w = 500\,\mathrm{nm}$ and a third one in the middle with width w_m are deposited onto the YIG sample ($t_\mathrm{YIG} = 22\,\mathrm{nm}$) with an edge-to-edge distance d_m between the three strips. Taken and adapted from [4].

To investigate the all-electrical magnon transport we perform angle dependent magnetotransport measurements. To this end the sample is placed in a cryostat with a superconducting 3D-vector magnet. The magnetic field is then rotated within the film plane as indicated in the coordinate system in Fig. 3.2 and 3.3. The rotation angle φ is defined between the y-axis and the external magnetic field orientation. Within the cryostat it is furthermore possible to control the temperature T from $4\,\mathrm{K}$ to $300\,\mathrm{K}$ with $\pm 10\,\mathrm{mK}$ precision.

At the injector we apply a charge current of $I_\mathrm{inj} = 100\,\mu\mathrm{A}$ which corresponds to a large current density within the injector of $j_\mathrm{inj} = \frac{I_\mathrm{inj}}{t_\mathrm{Pt} w} = 2.86 \cdot 10^{10}\mathrm{A/m^2}$. For this reason we electrically excite magnons via the SHE but simultaneously excite thermal magnons via Joule heating. To distinguish between electrically and thermally generated magnons the DC current reversal technique or an AC lock-in technique can be used. We explain the two approaches in the following Sections 3.2.1 and 3.2.2, respectively.

3.2.1 DC Detection Technique

We consider a two-terminal structure that is contacted as shown in Fig. 3.2(b). We switch the charge current density at the injector between positive ($+I_\mathrm{inj}$) and negative ($-I_\mathrm{inj}$) polarity and measure the corresponding voltages: U^+_det and U^-_det. The electrical contribution to the magnon transport is proportional to odd powers of I_inj and thus the corresponding voltage contribution $U^\mathrm{el}_\mathrm{det}$ changes sign under polarity change. The thermal voltages on the other hand are even under current reversal. Thus the electrical and thermal magnon transport signals $U^\mathrm{el}_\mathrm{det}$ and $U^\mathrm{th}_\mathrm{det}$ can be calculated via:

$$U^\mathrm{el}_\mathrm{det} = \frac{U^+_\mathrm{det} - U^-_\mathrm{det}}{2}, \tag{31}$$

$$U^\mathrm{th}_\mathrm{det} = \frac{U^+_\mathrm{det} + U^-_\mathrm{det}}{2}. \tag{32}$$

To apply the injector current I_inj as shown in Fig. 3.2(a) we use a *Keithley 2400* Sourcemeter which is furthermore able to detect the local voltage at the injector simultaneously. Thus, we can additionally measure the SMR signal at the injector (see Section 2.4). The open circuit voltage at the detector electrode is measured via a *Keithley 2182* Nanovoltmeter. In order to improve the signal-to-noise ratio and overcome for example thermal drifts we repeat the current reversal measurement five times for each angle φ and then take the arithmetic mean of the five values of the calculated electrical (see Eq. (31)) and thermal (see Eq. (32)) detector voltage. With that we have the final magnon transport signal we can analyze in Section 4.1.

3.2.2 AC Detection Technique

In this thesis we use the AC lock-in detection technique to distinguish between the electrical and thermal magnon transport signals in three-terminal structures as shown in Fig. 3.3. These structures are used to investigate the electrical modulation of magnon transport signals due to an additional DC-charge current applied to the modulator electrode. We apply an AC-current $I_{\mathrm{inj,ac}}$ with a frequency of $f = 7\,\mathrm{Hz}$ using a *Keithley 6221* AC Current Source as shown in Fig. 3.3(b). At the modulator electrode an additional DC-current I_{mod} is applied. The magnon transport signal is then measured at the detector using a *MFLI* Lock-in Amplifier from *Zurich Instruments*.

We apply a sinusoidal AC-current at the injector: $I_{\mathrm{inj,ac}}(t) = I_{\mathrm{max,inj}} \sin(\omega t)$, where $I_{\mathrm{max,inj}} = 100\,\mu\mathrm{A}$ is the injected peak current amplitude and $\omega = 2\pi f$ the angular frequency. According to that, the charge current at the detector has the form: $I_{\mathrm{det}}(t) = I_{\mathrm{max,det}} \sin(\omega t + \phi)$, here $I_{\mathrm{max,det}}$ is the detector peak current amplitude, the frequency ω is the same as for the injector current and ϕ is a phase shift. We can write the detector voltage as:

$$U_{\mathrm{det}}(t) = R_1 I_{\mathrm{det}}(t) + R_2 I_{\mathrm{det}}^2(t) + \mathcal{O}\left(I_{\mathrm{det}}^3(t)\right), \tag{33}$$

where R_1 and R_2 describe conversion processes via the magnon transport between injector and detector electrode. With the lock-in method we can measure the n^{th} harmonic voltage signals $U_{\mathrm{n}\omega}$. We are especially interested in the first and second harmonic signals, which correspond to the electrical and thermal magnon transport signals. The detector voltage U_{det} is multiplied by a $\sin(\omega t)$ and a $\cos(\omega t)$ and integrated over a time intervall T much larger than the period time of the sinusoidal AC-current due to low-pass filtering. We then get a X and a Y component:

$$U_{\mathrm{n}\omega}^{\mathrm{X}} = \frac{\sqrt{2}}{T} \int_t^{t+T} \sin\left(n\omega t'\right) U_{\mathrm{det}}\left(t'\right) dt', \tag{34}$$

$$U_{\mathrm{n}\omega}^{\mathrm{Y}} = \frac{\sqrt{2}}{T} \int_t^{t+T} \cos\left(n\omega t'\right) U_{\mathrm{det}}\left(t'\right) dt'. \tag{35}$$

With that we can now insert Eq. (33) into Eq. (34) for the X components of the first and second harmonic and into Eq. (35) for the Y components of the first and second harmonic:

$$U_{1\omega}^{\mathrm{X}} = \frac{1}{\sqrt{2}} \left(I_{\mathrm{max,inj}} R_1 + \frac{3}{4} I_{\mathrm{max,inj}}^3 R_3 \right) \cos(\phi), \tag{36}$$

$$U_{1\omega}^{\mathrm{Y}} = \frac{1}{\sqrt{2}}\left(I_{\mathrm{max,inj}}R_1 + \frac{3}{4}I_{\mathrm{max,inj}}^3 R_3\right)\sin\left(\phi\right), \tag{37}$$

$$U_{2\omega}^{\mathrm{X}} = \frac{1}{2\sqrt{2}}I_{\mathrm{max,inj}}^2 R_2 \sin\left(2\phi\right), \tag{38}$$

$$U_{2\omega}^{\mathrm{Y}} = \frac{1}{2\sqrt{2}}I_{\mathrm{max,inj}}^2 R_2 \cos\left(2\phi\right). \tag{39}$$

We can see that the first harmonic voltage signals are proportional to odd powers of $I_{\mathrm{max,inj}}$ and thus change sign under change of polarity. These signals correspond to the electrically induced magnon transport signal. The second harmonic contributions on the other hand are even with respect to $I_{\mathrm{max,inj}}$ and thus correspond to the thermally generated magnon signal. As a final step we can now apply a rotation matrix to the X and Y parts in order to get rid of one of the components and have the final detector magnon transport signal in only one quadrature. For the electrical magnon transport signal we want to keep the X component and want to have a ϕ that leads to vanishing signal in the Y component. For the thermal magnon transport signal the goal is to get the full signal in Y and have no finite signal in X. The rotated components can then be written as:

$$\begin{pmatrix} U_{\mathrm{n}\omega}^{\mathrm{X}'} \\ U_{\mathrm{n}\omega}^{\mathrm{Y}'} \end{pmatrix} = \begin{pmatrix} \cos n\phi & \sin n\phi \\ -\sin n\phi & \cos n\phi \end{pmatrix} \begin{pmatrix} U_{\mathrm{n}\omega}^{\mathrm{X}} \\ U_{\mathrm{n}\omega}^{\mathrm{Y}} \end{pmatrix}. \tag{40}$$

For more details on the lock-in detection method see Ref. [5, 14, 47]. When we discuss the results of our measurements in Section 4.2 and 4.3 we use $U_{1\omega}$ for $U_{1\omega}^{X'}$ and $U_{2\omega}$ for $U_{2\omega}^{Y'}$. The used *MFLI* Lock-in Amplifier can simultaneously measure the first and second harmonic voltage signal at the detector electrode. It furthermore triggers the *Keithley 6221* AC Source at the injector electrode to synchronize the AC signals. Before the signal is measured at the detector it is amplified by a *SR560* Low Noise Preamplifier.

3.3 Brillouin Light Scattering

The focus in this section lies on the concepts and the setup of Brillouin Light Scattering that was first theoretically described by Brillouin [48] and which we used for the measurements described in Section 4.3. The introduction here is very brief, for more details see [49–53]. Brillouin Light Scattering (BLS) describes the inelastic scattering of photons with quasiparticles in a solid and can therefore be used to detect coherent and incoherent magnons and acoustic phonons [53, 54]. The laserlight shines on a sample and after inelastic scattering with the quasiparticles, the reflected light has a shift in frequency, which we want to detect in the experiment. Fig. 3.4 shows the scattering processes due to energy and momentum conservation: We can differ between the Stokes process, where a quasiparticle is created (see panel (a)) and the Anti-Stokes process, where a quasiparticle is annihilated (see panel (b)). We get:

$$\hbar\omega_{\mathrm{s}} = \hbar\omega_{\mathrm{i}} \pm \hbar\omega_{\mathrm{m,p}}, \tag{41}$$

$$\hbar k_{\mathrm{s}} = \hbar k_{\mathrm{i}} \pm \hbar k_{\mathrm{m,p}}, \tag{42}$$

where $+$ describes the annihilation or Anti-Stokes process and $-$ the creation or Stokes process, ω and k are the frequency and the wave vector, which are described by their indices: s denotes the backscattered light, i the incident light and m, p the created or annihilated magnon or phonon.

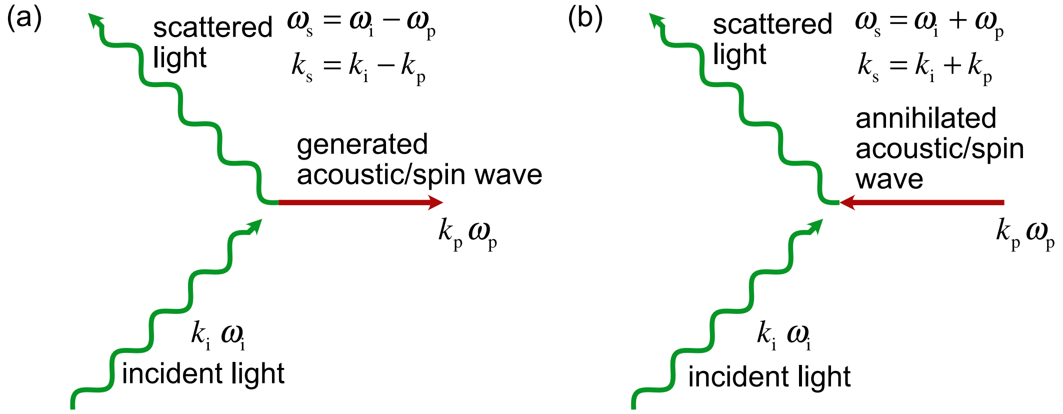

Figure 3.4: Illustration underlying processes of Brillouin Light Scattering. (a) Stokes Process: Creation of a quasiparticle due to energy and momentum conservation, resulting in a shift to a lower frequency. (b) Anti-Stokes Process: Annihilation of a quasiparticle due to energy and momentum conservation, resulting in a shift to a higher frequency. Taken from [49].

As already mentioned, we are escpecially interested in the shift in frequency of the backscattered light. In order to be able to detect the very small frequency shift we us a Tandem Fabry Pérot interferometer (TFPI): two Fabry-Perot interferometer (FPI) that are passed three times each by the backscattered light. First we have a look at a single FPI, which was developed by Sandercock [55]. It consists of two mirrors with distance d on which the light incidents with an angle α, shown in Fig. 3.5 (a), the light is transmitted and reflected. With the phase difference $\Delta\phi$, which depends on α and d of the reflected light we can get the intensity of the transmitted light by Airys' formula [49, 56]:

$$I_t = \frac{I_0}{1 + F \sin^2\left(\frac{\Delta\phi}{2}\right)}, \tag{43}$$

where I_0 is the intensity of the incidenting light and F the finess factor, which correlates to the reflectivity R of the mirrors:

$$F = \left(\frac{2}{\pi}\right)^2 \cdot \frac{c^2}{4l^2 \delta f^2} = \frac{4R}{1 - R^2}. \tag{44}$$

Panel (b) shows the transmission as a function of the phase difference for different finess factors. δf describes the full width at half maximum, which is a measure for the contrast of a FPI. The free spectral range $\delta\lambda = \frac{c_0}{2d}$ (c_0 is the light velocity in vacuum) determines the distance between two maxima in the transmitted spectrum.

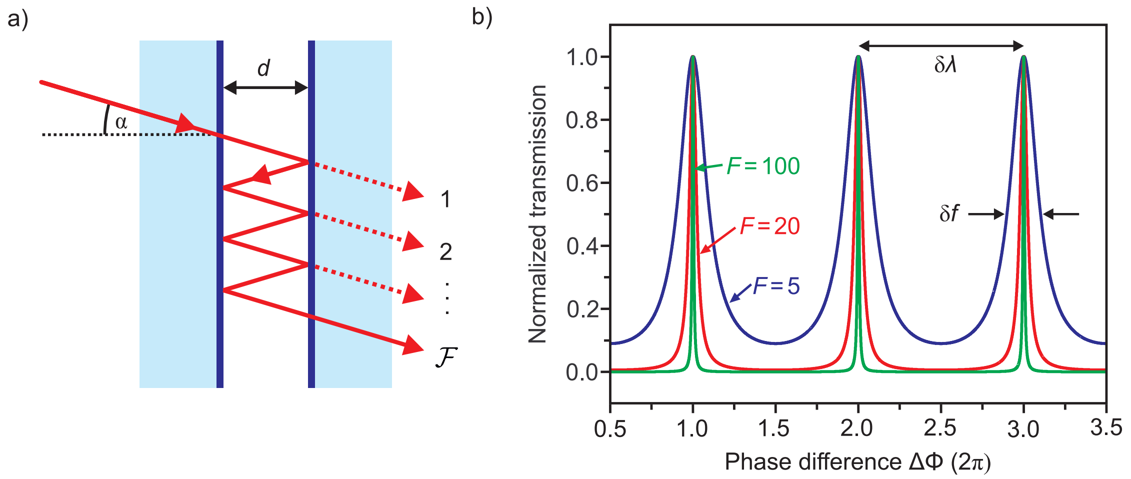

Figure 3.5: (a) Scheme of Fabry Pérot interferometer: light incidents between two mirrors. (b) Normalized transmission of the Fabry Pérot interferometer as a function of the phase difference for different finess factors F. Free spectral range $\delta\lambda$ and full-width-half maximum δf are marked. Taken from [50].

Up to now we discussed one single FPI to understand the usage of a tandem FPI in our experiments, we present in Fig. 3.6 the transmission spectra as a function of d for the scattered light for different FPI configurations. Panel (a) shows the transmission spectra for one FPI. In the transmitted signal we find periodic peaks with the mirror distance d, associated to elastic and inelastic scattered lights and the periodic transmission pattern from the free spectral range of the FPI. Thus a clear identification of peaks associated with the Stokes or Anti-Stokes process is not possible. To avoid that, we need a second FPI with a different free spectral range, i.e. introducing a finite offset to d, its transmission spectrum is shown in panel (b). Combining these two FPI we get a tandem Fabry-Pérot Interferometer (TFPI) and therefore a transmission spectrum, that is the product of the transmission functions of the two single FPIs (see panel (c)). The two FPIs suppress each others higher and lower transmission orders depending on the finess factor and we get a clear assignment of the Stokes and Anti-Stokes process.

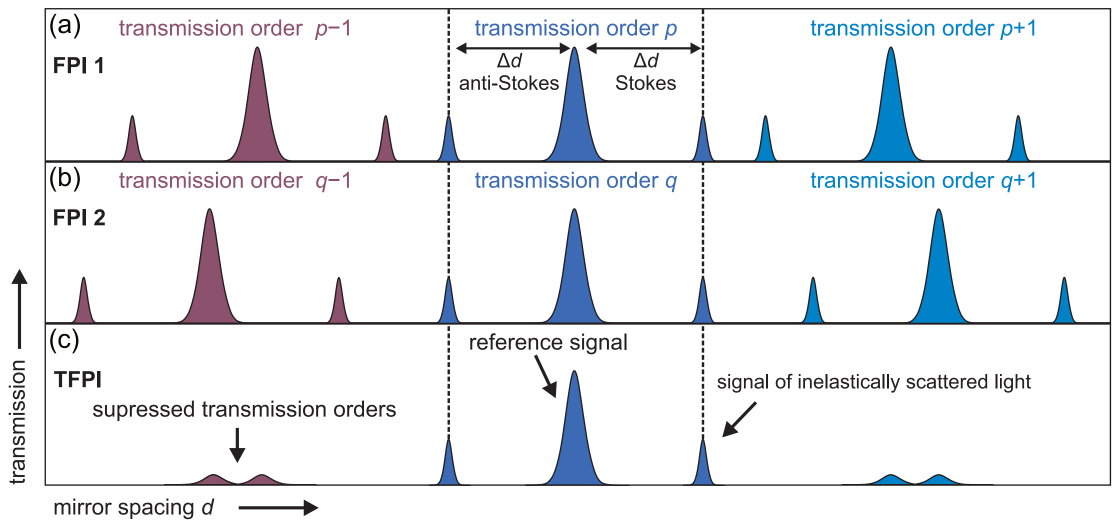

Figure 3.6: Transmission spectra in a TFPI. (a) and (b) Transmission spectra for two separate FPI with different transmission orders. (c) Resulting transmission spectra of a TFPI which is the overlap of the two individual FPI. Taken from [50].

Fig. 3.7 shows the TFPI schematically. The two FPIs are installed with an angle α to each other connected by an additional mirror. Due to the different mirror distances, we get two different transmission spectra and different free spectral ranges and therefore clearly assignable Stokes and Anti-Stokes lines (see Fig. 3.6 (c)). The right mirrors of both FPIs are installed on a translation stage which makes it possible to change the transmitted wavelength via changing the mirror distances:

$$d_1 = d_{1,0} + d_\mathrm{s}, \tag{45}$$

$$d_2 = d_{2,0} + d_\mathrm{s} \cdot \cos(\alpha), \tag{46}$$

where d_1 and d_2 are the final mirror distances, $d_{1,0}$ and $d_{2,0}$ are the mirror distances for position zero of the translational stage and d_s is the translational change of the stage. As seen in Fig. 3.7 the light passes both FPIs three times which leads to a high contrast. Coming out of the TFPI the intensity of the transmitted light is detected by a single photon detector.

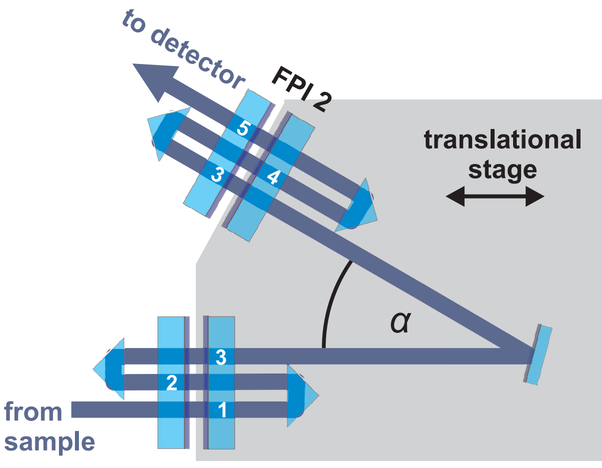

Figure 3.7: Beam path in a TFPI. Two FPI in an angle α to each other connected with an additional mirror. The right mirror of each FPI are installed on a translational stage to be able to vary the mirror distance and therefore be able to change the wavelength of the transmitted laser light. Taken from [50].

In Fig. 3.8 we illustrate the BLS setup used for our measurements made at the group of Prof. M. Weiler at the RPTU in Kaiserslautern. We are using a micro-focused BLS which means via micro-focussing we are able to investigate microstructures. A detailed list of the components can be looked up in Tab. 3.1.

Label	Element	Label	Element
1	$491\,\mathrm{nm}$ Cobolt Samba Laser	10	10:90 beam splitter
2	Optical Isolator	11	Microscope objective
3	Mode filter TCF-2 (self-stabilizing)	12	Dicroic mirror
4	Beam splitter	13	$\lambda/2$ plate (motorized, rotatable)
5	Power meter	14	Periscope
6	Neutral density filter	15	Biconvex lens
7	Telescope	16	LED
8	Periscope	17	CCD Camera
9	50:50 beam splitter	18	Single photon detector

Table 3.1: List of components of the microfocused BLS setup in Fig. 3.8

We used a blue laser (1) with $\lambda = 491\,\mathrm{nm}$. The laser first passes an optical isolator (2) in order to prevent backreflected light. The mode filter (3) behind that, consists of two mirrors, that suppress possible side modes. Afterwards there is a beam splitter (4), where a reference beam for the TFPI is coupled out and the backreflected light from the sample is used for autofocussing (5). The original beam is then passing a neutral density filter (6), where the intensity can be controlled. The telescope (7) increases the laser beams cross section and with the periscope (8) the laser beam is transfered to a higher level above the optical table. Now a beam splitter (9) couples in a LED light (16) (orange) which we need for the illumination of the microscope. The now following beam splitter (10) directs the laser beam through a microscope objective (11) onto the sample. The sample is installed on a stage between two poles of an electromagnet where we can get a field of up to $\mu_0 H = 55\,\mathrm{mT}$. The sample-stage is moveable in x-, y- and z-direction. A dichroic mirror (12) is filtering out the microscope illumination from the sample backreflected light. The filtered microscope illumination is then guided into the CCD camera (17). The laserlight passes a $\frac{\lambda}{2}$-plate (13), which is installed in a motorized cage system and automatized rotates the polarization of the back reflected light. A periscope (14) transfers the laser on the height of the TFPI, where a biconvex lens (15) focuses the laser beam onto the pinhole of the TFPI. The light then passes the TFPI shown in detail in Fig. 3.7 and is detected via a single photon detector (18). We used a $TFPI2HC$ provided by $TableStable$ and controlled it with the software system $TFPDAS6$ from $ThatecinnovationGmbH$ [49].

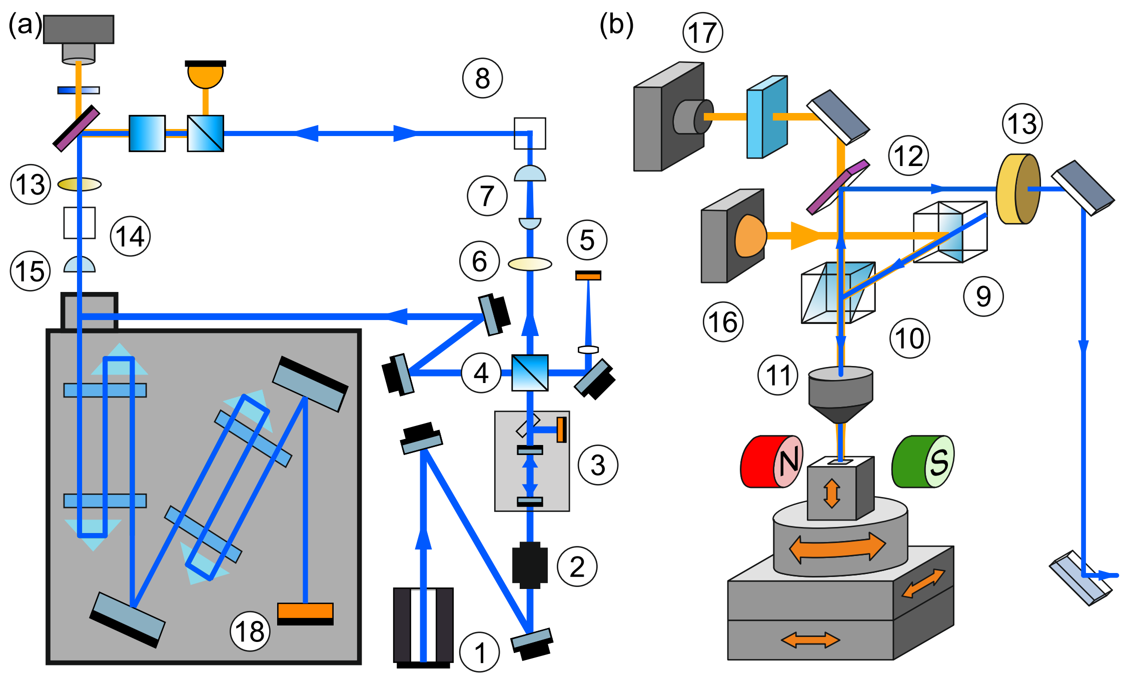

Figure 3.8: Illustration of the microfocused BLS setup. The beampath of the used laser is marked by the blue lines and arrows. The orange lines show the beampath of the light used for the microscope. A detailed list of the used parts is given in Tab. 3.1. Taken and adapted from [49].

The limitation of the used micro BLS is shown in Fig. 3.9. Only quasiparticles up to a wavevector k_{max} can be detected.

$$k_{\text{max}} = 2k_{\text{p}} \cdot \sin(\theta) \, , \tag{47}$$

where k_{p} is the wavevector of the incoming photon and θ the opening angle of the incident light. This wavevector correlates to the numerical aperture of the microscope objective.

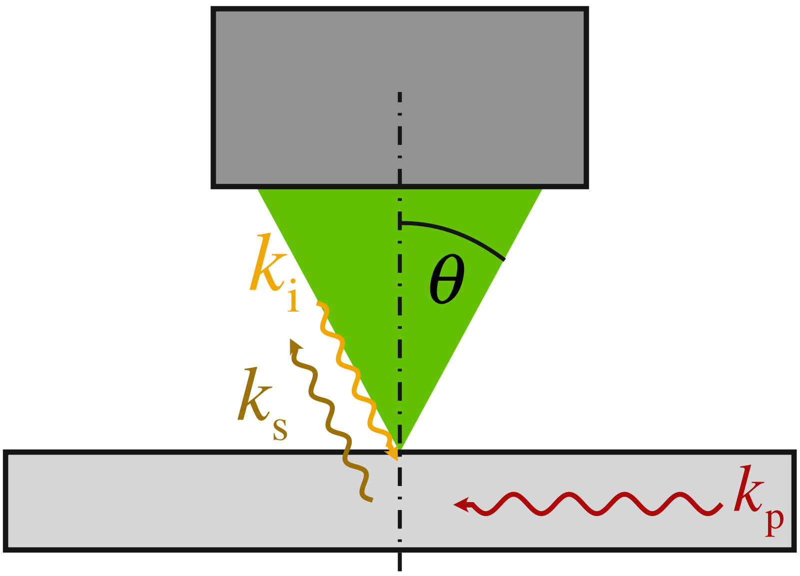

Figure 3.9: Limitation condition of the microfocussed BLS. The wavevector K_{max} of the detected quasiparticles is dependent of the opening angle of the incidenting light due to th microscope objective. Taken from [49].

We are especially interested in simultaneous measurements of BLS and the in Section 3.2.2 discussed magnon transport measurements on three-terminal structures. Fig. 3.10(a) shows the used electrical connection of the sample, for more details on the applied charge currents and the used lock-in detection scheme see Section 3.2.2. For the optical measurement via BLS it was necessary to turn the sample upside down in order to be able to focus the from above coming laser on the interface between the YIG and the Pt of the modulator strip. Measuring our samples in Kaiserslautern was quite challenging because we had to realize a sample installation that also fits into our setup at the WMI for precharacterization, where we were limited in the total height of the sample holder. This limitation is due to our sample rod, we needed for the measurements in our cryostat. Moreover, we had to use our common sample holder with 20 contact pins for the electrical connection. To account for all of these requirements, we designed a special sample holder shown in Fig. 3.10(b) with two printed circuit boards (PCB). This was necessary because at our common sample holder the YIG is mounted on a copper block and thus blocks optical access from the backside. To be able to mount the sample in the two very different setups, we glued and wire bonded the sample on one PCB (1) and soldered the electrical connection pins on a second PCB. We connected the two PCBs with long isolated Cu wires to be able to set the wire bonds on the magnon transport structures in the disassembled state (1). For assembling we placed the PCB with the sample upside down on the other PCB attaching them with four screws. We wrapped the connecting wires around the screws to have a compact sample holder (2) and (3) for installation in the setups. Fig. 3.10(c) shows the sample holder on the moving stage of the micro BLS setup in installation position (1) and in measuring position between the two poles of the electromagnet.

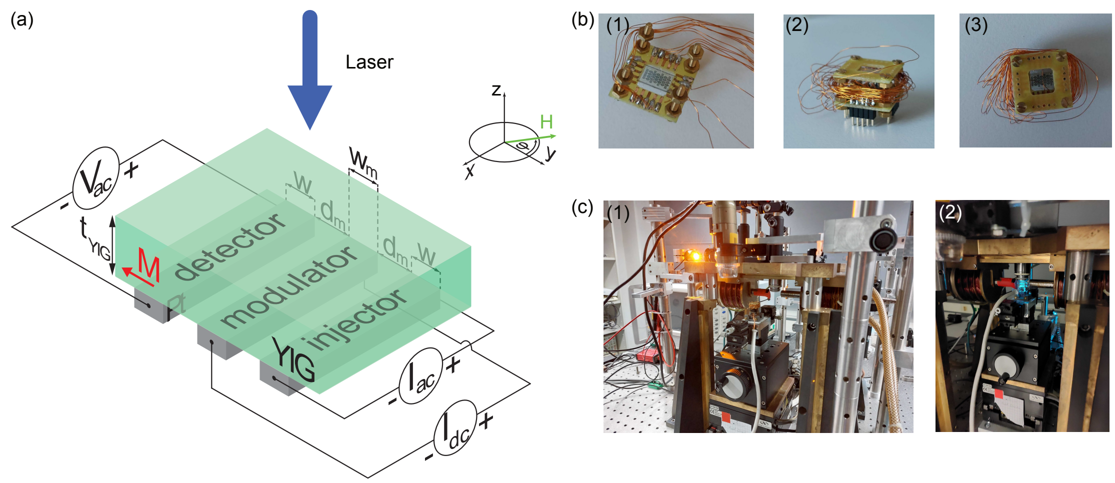

Figure 3.10: (a) Schematic structure of electrical connection of the upside down three-strip device for the BLS setup with coordinate system and laser direction. Taken and addapted from [4]. Two electrodes with width $w = 500\,\mathrm{nm}$ working as injector and detector with a distance $d_\mathrm{m} = 350\,\mathrm{nm}$ to the modulator electrode in the middle that has a width of $w_\mathrm{m} = 300\,\mathrm{nm}$. (b) Pictures of the used sample holder. (c) Pictures of the installed sample in the BLS setup: in installation position (left) and in measuring position (right).

We used a magnetic field at $\varphi = 180°$ corresponding to Fig. 3.10(a) and sweeped the modulator current for different magnetic fields while measuring simultaneuosly the magnon transport signal at the detector electrode via lock-in detection (see Section 3.2.2) and a frequency-resolved BLS spectrum with the laser spot positioned beneath the modulator strip. The direction of the magnetization in these measurements is due to the upside-down orientation of the sample inverted to the all-electrical measurements shown in Section 3.2. The results of these measurements are discussed in Section 4.3.

4 Experimental results

In this section we want to take a look at the experimental results of all-electrical magnon transport in YIG thin films in combination with simultaneous BLS measurements. First we focus on results obtained in two-strip devices (Section 4.1). We discuss the electrical and thermal transport signal measured at the detector electrode and extract several properties from the signals: The magnon decay length and its dependence on the magnetic field and temperature and the spin conductance ot the YIG layer. This kind of measurements were carried out successfully for the first time in $22\,\mathrm{nm}$ LPE-YIG films grown by Innovent. These results are thus important to evaluate the suitability of these thin YIG films for future all-electrical magnon transport experiments and to compare the results to literature values. As a next step we investigate magnon transport and modulation measurements in three-strip devices (Section 4.2). We look into the modulation properties of the modulator electrode by extracting the detector voltage as a function of the magnetic field and the current applied at the modulator. Finally, we show the results obtained for combined all-electrical magnon transport and BLS measurements. This allows us to get a better insight into the magnonic properties in the situation of zero effective damping [4, 5] and infer the influence on all-electrical magnon transport. (Section 4.3).

4.1 All-electrical magnon transport in two-terminal YIG/Pt heterostructures

On the following pages we describe and analyze the magnon transport measurements conducted on two-strip structures on $22\,\mathrm{nm}$ thin YIG films. For all measurements in this section we applied a charge current $I_{\mathrm{inj,dc}} = 100\,\mu\mathrm{A}$ at the injector. At the detector electrode we measure the voltage U_{det}. We can distinguish between electrical and thermal magnon transport by using the current reversal method, described in Section 3. We vary the distances between the two NM electrodes and extract the electrical and thermal magnon decay length from $d = 900\,\mathrm{nm}$ to $d = 3.5\,\mu\mathrm{m}$ between injector and detector, for different magnetic fields from $\mu_0 H = 50\,\mathrm{mT}$ to $\mu_0 H = 2\,\mathrm{T}$ and for different temperatures from $T = 30\,\mathrm{K}$ to $T = 280\,\mathrm{K}$. We also extract the interface spin current transparancy from this signals [57]and compare our findings to literature.

4.1.1 Distance-dependent magnon transport experiments

In the first part of this section we analyze how the variation of the distance d between injector and detector influences the magnon transport signal and extract the magnon decay length. For this reason, we utilize two-terminal Pt structures, discussed in Section 3.1 with different edge-to-edge separations d between the electrodes. At the injector electrode a DC-charge current of $I_{\mathrm{inj}} = 100\,\mu\mathrm{A}$ is applied. The voltage signal measured at the detector can be disentangled into a contribution originating from the electrically generated magnons $U_{\mathrm{det}}^{\mathrm{el}}$ and the thermally generated magnons $U_{\mathrm{det}}^{\mathrm{th}}$ via the current reversal method described in Section 3.2.1. We apply an external magnetic field of $\mu_0 H = 50\,\mathrm{mT}$ to control the direction of the magnetization with respect to the current flow direction within the Pt electrode, described by the angle φ (see Fig. 3.2). In Fig. 4.1 we show the electrical and thermal magnon transport signal as a function of the external magnetic field orientation φ

at a temperature of $T = 280\,\mathrm{K}$ for three different distances d.

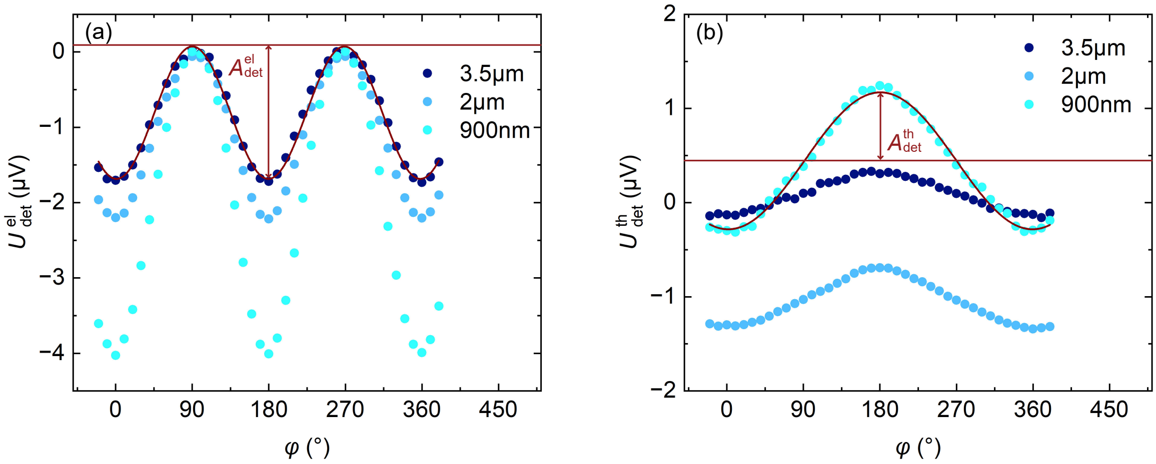

Figure 4.1: Magnon transport signal measured at the detector electrode as a function of the magnetic field orientation. The measurements are conducted at a temperature of $T = 280\,\mathrm{K}$ and a magnetic field strength of $\mu_0 H = 50\,\mathrm{mT}$ for three different distances between injector and detector. (a) Electrical magnon transport signal caused by SHE. Fitted with an $y_0 + A_{\mathrm{det}}^{\mathrm{el}} \cos^2 \varphi$-function (red solid line). The amplitude of the electrical transport $A_{\mathrm{det}}^{\mathrm{el}}$ is indicated exemplarily for $d = 3.5\,\mathrm{\mu m}$. (b) Thermal magnon transport signal caused by SSE. Fitted with an $y_0 + A_{\mathrm{det}}^{\mathrm{th}} \cos \varphi$-function (red solid line) with y_0 accounting for a constant offset. The amplitude of the thermal transport $A_{\mathrm{det}}^{\mathrm{th}}$ is shown exemplarily for one distance.

Panel (a) covers the electrical magnon transport signal $U_{\mathrm{det}}^{\mathrm{el}}$ caused by the SHE (see Section 2) for three distances $d = 3.5\,\mathrm{\mu m}$, $2\,\mathrm{\mu m}$ and $0.9\,\mathrm{\mu m}$ between injector and detector. For all distances we observe a $\cos^2 \varphi$ dependence as a function of the rotation angle φ. For $\varphi = 0°$, $180°$ and $360°$ the detector signal $U_{\mathrm{det}}^{\mathrm{el}}$ exhibits maximum negative values, while the signal vanishes for $\varphi = 90°$ and $270°$. In the latter configuration the applied electrical current is parallel to the magnetization in the YIG thin film ($M \parallel j$) and no magnon spin accumulation is excited below the injector. If the external magnetic field is rotated by $90°$ ($\varphi = 0°$, $180°$ and $360°$) the magnetization vector is oriented perpendicular to the applied charge current ($M \perp j$) and a non-equilibrium magnon accumulation is excited below the injector electrode. As described in Section 2.4 the magnons diffuse in the ferrimagnetic insulator and are converted into a voltage signal in the detector electrode via the ISHE, that can then be detected. Due to the lateral device geometry and the combined action of the SHE and ISHE in Pt, the ISHE induced charge current has the opposite polarity compared to the injector current und we observe a negative voltage. We use

$$U_{\mathrm{det}}^{\mathrm{el}} = y_0 + A_{\mathrm{det}}^{\mathrm{el}} \cos^2 \varphi, \tag{48}$$

where y_0 describes the offset voltage, to describe the angle dependence of the electrical magnon transport signal and extract the amplitude $A_{\mathrm{det}}^{\mathrm{el}}$ of the SHE-generated magnon transport signal (indicated in Fig. 4.1(a)). An exemplary fit to the data is shown for $d = 3.5\,\mathrm{\mu m}$ (red solid line). We observe a clear decrease in $A_{\mathrm{det}}^{\mathrm{el}}$ for increasing electrode separations d. We want to discuss this behaviour in greater detail later in this section.
In Ref. [58] Wei et al. report on a large magnon spin conductance for thin YIG layers ex-

tracted from all-electrical magnon transport experiments. We can compare their results obtained for a $16\,\mathrm{nm}$ thin LPE-YIG film to our values. For the $d = 900\,\mathrm{nm}$ device we find $A^{\mathrm{el}}_{\mathrm{det}} = 3.98\,\mu\mathrm{V}$, which corresponds to an effective resistance of $39.8\,\mathrm{m}\Omega$. Ref. [58] provides a value of $40\,\mathrm{m}\Omega$ for $d = 1000\,\mathrm{nm}$. Thus we conclude that we obtain very similar detector voltage signals for the LPE-YIG layer grown by Innovent and one can expect comparable efficiencies for spin transport via magnons in these layers. This finding highlights that the results obtained by Wei et al. in Ref. [58] are indeed universal for YIG and provide an intriguing perspective for magnon transport experiments in thin YIG layers.
In Fig. 4.1 (b) the thermal contribution to the magnon transport signal $U^{\mathrm{th}}_{\mathrm{det}}$ is shown as a function of the angle φ. In contrast to the electrical contribution, the thermal signal shows a $\cos\varphi$ dependence as a function of the rotation angle φ. The generation of thermal magnons due to Joule heating in the YIG is independent of the angle between the magnetization orientation of the YIG film and the charge current direction in the injector electrode. The spin polarization of thermally injected magnons always points along $\boldsymbol{m}$ and the angle dependence only originates from the ISHE-based detection of the signal [12, 32]. For $\varphi = 0°$ and $360°$ we should observe an electrical charge current, induced via ISHE, flowing in the $-x$ direction (see Fig. 3.2) and thus generating a negative voltage signal, due to Eq. (4). For $\varphi = 180°$ the magnetization is oriented in the opposite direction, resulting in a positive voltage. For $\varphi = 90°$ and $270°$ the thermal magnon transport signal should vanish, as $\boldsymbol{m}$ is oriented parallel to the Pt-strip and no charge current is induced by the ISHE along the Pt-strip.

However for $\varphi = 90°$ and $270°$ still a finite detector voltage is observed due to a constant voltage offset, that is superimposed on the thermal magnon transport signal for each distance shown in Fig. 4.1(b). For this reason, we describe the angle dependence by

$$U^{\mathrm{th}}_{\mathrm{det}} = y_0 + A^{\mathrm{th}}_{\mathrm{det}} \cos\varphi, \tag{49}$$

where y_0 accounts for the constant offset voltage. This constant offset is up to now not fully understood and requires a systematic investigation of different samples and measurement setups. Possible contributions are additional thermopower effects generating a voltage signal in the Pt detector and a finite voltage offset from the measurement device. This goes beyond the scope of this thesis. The red solid line shows an exemplary fit to the data for a electrode separation of $d = 900\,\mathrm{nm}$. Similar to the electrically injected magnons, the thermal magnon transport amplitude shows a clear decrease with increasing electrode separation d. We want to take a closer look at the distance-dependence of the electrical and thermal magnontransport signal in the following.

In Fig. 4.2 we show the extracted electrical $A^{\mathrm{el}}_{\mathrm{det}}$ and thermal $A^{\mathrm{th}}_{\mathrm{det}}$ amplitudes as a function of the edge-to-edge distance d between injector and detector electrode. Panel (a) covers the electrical amplitudes $A^{\mathrm{el}}_{\mathrm{det}}$ on a semi-logarithmical scale. We observe a clear decrease in the electrical magnon transport amplitude for increasing electrode separation d. The red solid line shows a fit for our data with an exponential decay

$$A_{\mathrm{det}} = A_0 \exp\left(-\frac{d}{\lambda_{\mathrm{m}}}\right), \tag{50}$$

here, A_0 is the amplitude of the fit function and λ_m the magnon decay length. Besides an outlier for $d = 3.5\,\mathrm{\mu m}$ the exponential decay describes the measured data very well and we can extract a magnon decay length of $\lambda_\mathrm{m,el} = (2.63 \pm 0.54)\,\mathrm{\mu m}$ at a magnetic field of $\mu_0 H = 50\,\mathrm{mT}$. As the measured data follows an exponential decay we infere that we are in the regime where magnon relaxation limits the magnon propagation distance [14, 38, 59]. If the diffusive transport would limit the magnon propagation length we would expect a $\frac{1}{d}$ dependence [38, 59]. To distinguish between these two regimes more accurately, more measurements for even smaller distances d are required to observe the transition to the $\frac{1}{d}$ regime, but such measurements were left out due to time constraints in this thesis. The extracted electrical magnon decay length of $\lambda_\mathrm{m,el} = (2.63 \pm 0.54)\,\mathrm{\mu m}$ is in good agreement to the findings for LPE-YIG films of approximately $\lambda_\mathrm{m,el} = 3.5\,\mathrm{\mu m}$ and $3\,\mathrm{\mu m}$ for $t_\mathrm{YIG} = 5.9\,\mathrm{nm}$ and $7.9\,\mathrm{nm}$ respectively [58]. In comparison to a $t_\mathrm{YIG} = 12.3\,\mathrm{nm}$ YIG film, grown by pulsed laser deposition (PLD), electrical magnon decay lengths of $\lambda_\mathrm{m} \approx 1\,\mathrm{\mu m}$ were found [5]. While this value is nearly a factor of 3 lower than the one obtained for LPE-YIG samples with comparable thickness, we need to also state that the magnon decay length in Ref. [5] was obtained from four-strip devices, where additional contributions from the Pt-strips may have reduced the magnon decay length. Thus we conclude that the LPE-YIG films from Innovent are very comparable in their performance as compared to LPE-YIG films from other groups. A more systematic comparison for the thin YIG samples grown with different growth methods should be the goal of future studies.

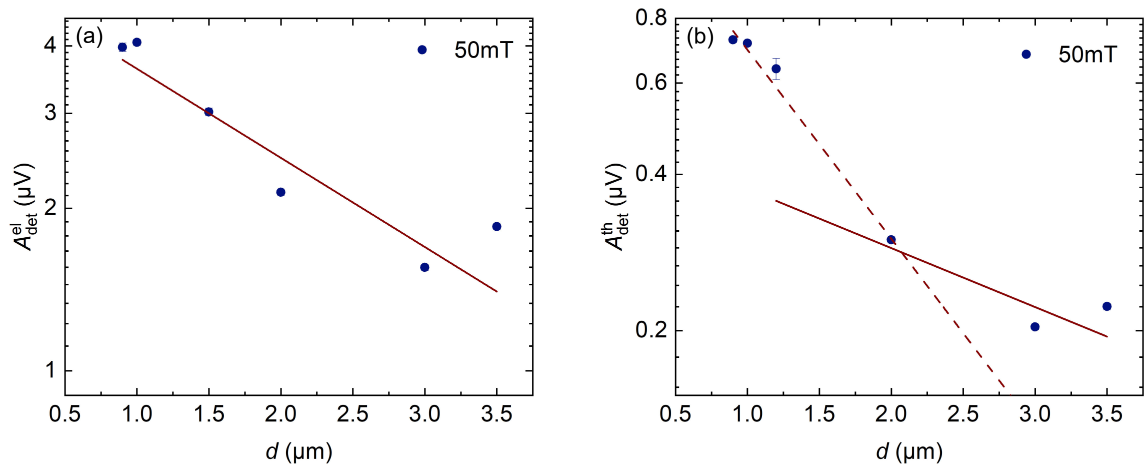

Figure 4.2: Amplitudes of the magnon transport signal measured at the detector electrode as a function of the distance d between injector and detector. The measurements are conducted at a temperature of $T = 280\,\mathrm{K}$ and a magnetic field of $\mu_0 H = 50\,\mathrm{mT}$. (a) The amplitudes $A^{\mathrm{el}}_{\mathrm{det}}$ are extracted from the electrical magnon transport signal and fitted with an exponential decay function Eq. (50) (red solid line). (b) The amplitudes $A^{\mathrm{th}}_{\mathrm{det}}$ are extracted from the thermal magnon transport signal and fitted with an exponential decay function Eq. (50) for a small distance regime (red dashed line) and a large distance regime (red solid line).

In Fig. 4.2(b) the amplitude of the thermal magnon transport signal as a function of the electrode separation is shown on a semi-logarithmic scale. Similar to $A^{\mathrm{el}}_{\mathrm{det}}$ we observe a decrease in the thermal magnon transport amplitude with increasing d. The distance-dependence of the thermal magnons is more complex, as we observe two different regimes, that can both be described by an exponential decay. For electrode separations $d \leq 2\,\mu\mathrm{m}$ the signal decreases much stronger than for larger distances $d \geq 2\,\mu\mathrm{m}$. For the thermally induced magnon transport signal, the actual temperature gradient profile contributes to the detector signal [16, 38]. In the following, we extract the thermal magnon decay length by fitting the datapoints $d \geq 2\,\mu\mathrm{m}$ [16]. We obtain a magnon decay length of $\lambda_{\mathrm{m,th}} = (3.81 \pm 2.21)\,\mu\mathrm{m}$ which is larger by a factor of 1.5 than for the electrical magnon transport signal. However, due to the larger error bars the difference between the extracted values is not significant enough to state any clear differences in the magnon decay length. We want to discuss these findings in the upcoming sections. Our thermal magnon decay length is significantly smaller than for a $t_{\mathrm{YIG}} = 1\,\mu\mathrm{m}$ YIG film at a comparable magnetic field of $\mu_0 H = 100\,\mathrm{mT}$ in Ref. [32], they observed a magnon decay length of $\lambda_{\mathrm{m,th}} = (6.7 \pm 0.2)\,\mu\mathrm{m}$.

4.1.2 Magnetic Field-dependence of magnon transport signals

In this section we focus on the influence of different magnetic field magnitudes on the electrically and thermally excited magnon transport. We use a two-strip structure with an electrode separation of $d = 900\,\mathrm{nm}$ and perform angle dependent magnon transport measurements at a temperature of $T = 280\,\mathrm{K}$. The external magnetic field magnitude is varied from $\mu_0 H = 50\,\mathrm{mT}$ to $2\,\mathrm{T}$. In Fig. 4.3(a) the electrical magnon transport signal $U_{\mathrm{det}}^{\mathrm{el}}$ is shown as a function of the rotation angle φ for four different magnetic field magnitudes. We observe the expected $\cos^2\varphi$ dependence for all magnetic fields. For $\mu_0 H = 2\,\mathrm{T}$ the fit with Eq. (48) is marked exemplarily (solid red line). We observe a strong decrease in the electrical magnon transport amplitude $A_{\mathrm{det}}^{\mathrm{el}}$ for increasing magnetic field magnitudes. This reduction can be explained by the change of the magnon bandstructure of the YIG film with increasing magnetic field. This affects the magnon generation at the YIG/Pt interface as well as the magnon decay length $\lambda_{\mathrm{m,el}}$ [5]. We discuss this two contributions in more detail later in this section.

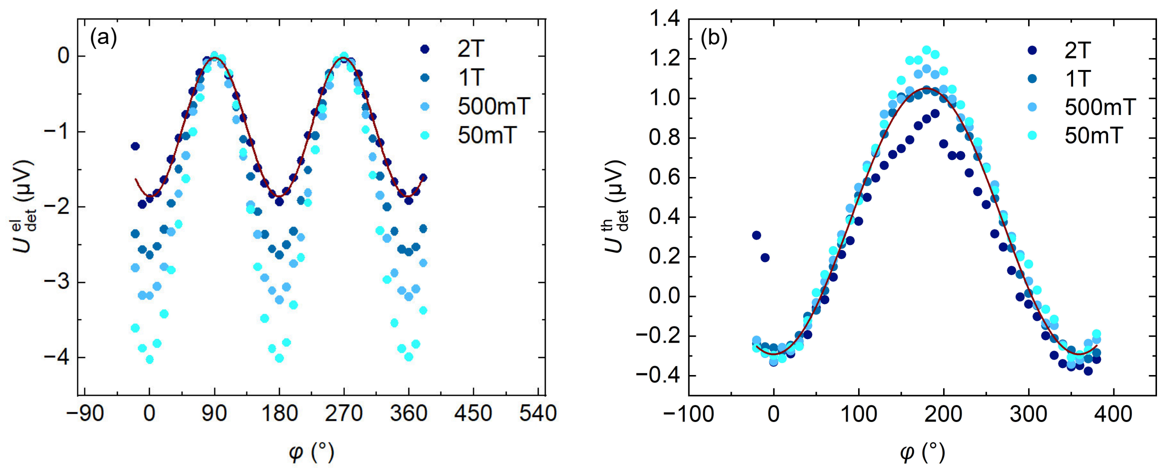

Figure 4.3: Magnon transport signal measured at the detector electrode as a function of the magnetic field orientation. The measurements are conducted at a temperature of $T = 280\,\mathrm{K}$ and a distance of $d = 900\,\mathrm{nm}$ between injector and detector for four different magnetic fields. (a) Electrical magnon transport signal caused by SHE. Fitted with an $\cos^2\varphi$-function (red solid line). (b) Thermal magnon transport signal caused by SSE. Fitted with an $\cos\varphi$-function (red solid line).

In Fig. 4.3(b) the thermal magnon transport signal $U_{\mathrm{det}}^{\mathrm{th}}$ as a function of the rotation angle is shown. The expected $\cos\varphi$ dependence is observed for all magnetic field magnitudes. We see that the thermal magnon transport amplitude is smaller than the electrical one. We extract the thermal magnon transport amplitude $A_{\mathrm{det}}^{\mathrm{th}}$ by fitting with Eq. (49) to the data, exemplarily shown for $\mu_0 H = 1\,\mathrm{T}$. Similar to the electric case we observe a decreasing magnon transport signal for increasing magnetic field magnitude.

In Fig. 4.4 we show the extracted electrical and thermal magnon transport amplitude respecpectively as a function of the electrode seperation on a semi-logarithmic scale. The solid lines are fits to the data using an exponential decay with Eq. (50). We observe that the electrical magnon transport signal can be described by a single exponential decay over the whole distance regime (see Fig. 4.4(a)). Only the datapoint $d = 3.5\,\mathrm{\mu m}$ is significantly larger than the expected exponential evolution for all magnetic field magnitudes. This can be explained by an increased interface transparency for this single structure. To this end we look at the local voltages at the injector U_{inj} and extract a SMR amplitude that is at a magnetic field of $\mu_0 H = 0.05\,\mathrm{mT}$ for $d = 3.5\,\mathrm{\mu m}$ 4% larger than for $d = 3\,\mathrm{\mu m}$ (see Ref. [33] for more details) The SMR amplitudes for $d = 3\,\mathrm{\mu m}$ and $d = 3.5\,\mathrm{\mu m}$ for the magnetic fields can be found in the appendix in Tab. A.1.

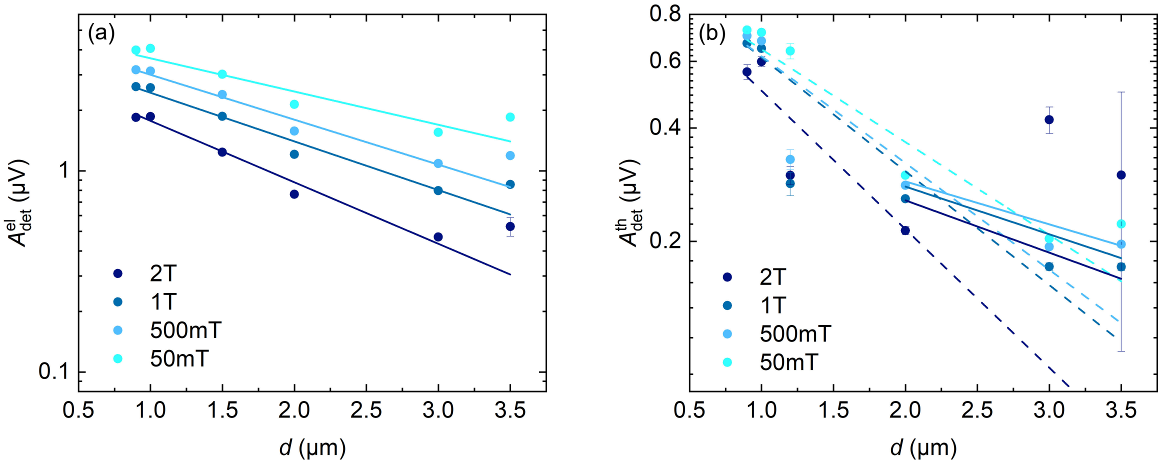

Figure 4.4: Amplitudes of the magnon transport signal measured at the detector electrode as a function of the distance d between injector and detector. The measurements are conducted at a temperature of $T = 280\,\mathrm{K}$ for different magnetic fields. (a) The amplitudes $A_{\mathrm{det}}^{\mathrm{el}}$ are extracted from the electrical magnon transport signal and fitted with an exponential decay function using Eq. (50) (blue solid lines). (b) The amplitudes $A_{\mathrm{det}}^{\mathrm{th}}$ are extracted from the thermal magnon transport signal and fitted with an exponential decay function with Eq. (50) for a small distance regime (blue dashed lines) and a large distance regime (blue solid line).

In contrary in the thermal magnon transport we observe two distinct regimes, which each can be described by an exponential decay with Eq. (50) (see dashed and solid lines). We attribute these two regimes to a combined action of the temperature profile and the actual magnon decay in the YIG layer. To ensure that the magnon transport signal is dominated by the magnon decay length and not by geometric diffusion or a temperature gradient below the detector we only use $d > 1\,\mathrm{\mu m}$ in our fit (see solid lines) [16], which we refer to as the large distance regime. For better comparison, we present the results obtained for the small distance regime (dashed lines) also in the following graphs. The two outliers at $\mu_0 H = 2\,\mathrm{T}$ for $d = 3\,\mu\mathrm{m}$ and $d = 3.5\,\mu\mathrm{m}$ are artifacts from the fit as the noise floor in the angle-dependent measurements was significantly larger compared to the other measurements.

The fit with Eq. (50) to the data allows us to disentangle magnetic field dependent contributions that originate from the injection mechanism at the interface $A_0\,(\mu_0 H)$ and the magnetic field-dependence of the magnon decay length $\lambda_\mathrm{m}\,(\mu_0 H)$ that limits the diffusive magnon transport.

A_0 is shown as a function of the magnetic field magnitude in Fig. 4.5. The extrapolated signal to $d = 0\,\mu\mathrm{m}$ roughly approximates the magnon transport signal that is generated at the injector. For the electrical case we observe a decrease of A_0^el as a function of the magnetic field. A_0^th on the other side seems to be rather independent of the external magnetic field. What can clearly be observed is that A_0^el is by a factor of 5 larger than A_0^th. And A_0^th for the small distance regime ($d \leq 2\,\mu\mathrm{m}$) is by a factor of 1.5 larger than for the large distance regime ($d \geq 2\,\mu\mathrm{m}$). This difference in magnetic field-dependence and magnitude may indicate that different magnon populations dominantly contribute to the detected signal as discussed in Ref. [16].

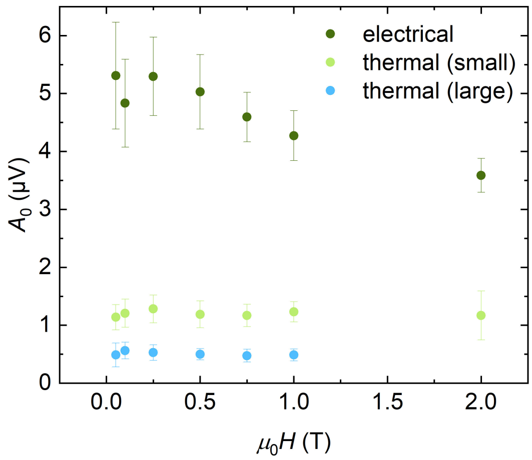

Figure 4.5: Extrapolated electrical A_0^el and small and large distance regime thermal A_0^th amplitudes of the magnon transport signals measured at the detector electrode as a function of the magnetic field. The measurements are conducted at a temperature of $T = 280\,\mathrm{K}$.

In Fig. 4.6 the electrical and thermal magon decay length as a function of the magnetic field magnitude is shown. For $\lambda_\mathrm{m,el}$ we observe a decrease as a function of the magnetic field, which is steep in the beginning and seems to saturate for larger magnetic fields. The thermal magnon decay length shows a rather constant behaviour within the error bars for both distance regimes. Furthermore $\lambda_\mathrm{m,th}$ seems for $d \geq 2\,\mu\mathrm{m}$ to be larger than $\lambda_\mathrm{m,el}$ by a factor of 1.5. The large errorbars in $\lambda_\mathrm{m,th}$ originate from the fact that only 4 distances are used to extract the magnon decay length, which limits the precision of the extracted values. The thermal magnon decay length for $d \leq 2\,\mu\mathrm{m}$ is approximately a third of the large distance regime.

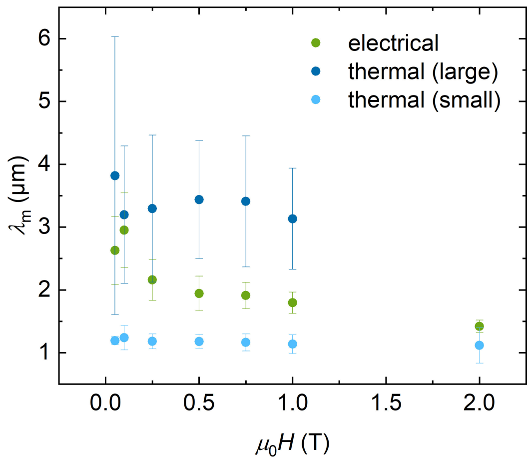

Figure 4.6: Magnon decay length λ_{m} as a function of the magnetic field. Extracted from the exponential decay using Eq. (50) of the electrical and small and large regime thermal amplitudes of the magnon transport detector signal measured at a temperature of $T = 280\,\mathrm{K}$ for different distances between injector and detector at different magnetic fields.

The magnetic field-dependence of the electrical magnon decay length in Fig. 4.6 that we observed for a $22\,\mathrm{nm}$ thick LPE-YIG film is in good agreement with the observations of the group of B.J van Wees [58]. They performed magnon transport measurements for LPE-YIG films with different thicknesses. For LPE-YIG films with a thickness of $t_{\mathrm{YIG}} = 5.9\,\mathrm{nm}$ and $t_{\mathrm{YIG}} = 7.9\,\mathrm{nm}$ they observed a decrease in the electrical magnon decay length with increasing magnetic field. For these ultra thin films they reported $\lambda_{\mathrm{m,el}} \approx 4\,\mathrm{µm}$ and $3\,\mathrm{µm}$ respectively for the magnetic field approaching to small fields which is in good agreement with $\lambda_{\mathrm{m,el}} = 2.63\,\mathrm{µm}$ that we found for our $22\,\mathrm{nm}$ thin YIG film. Also for thicker films of $t_{\mathrm{YIG}} = 1\,\mathrm{µm}$ and $2\,\mathrm{µm}$ a similar decrease with increasing field was observed. Here a magnon decay length of $\lambda_{\mathrm{m,el}} = 2.8\,\mathrm{µm}$ [32] and $\lambda_{\mathrm{m,el}} = 3.2\,\mathrm{µm}$ [16] in the low magnetic field limit was reported. The latter was observed at a lower temperature of $T = 200\,\mathrm{K}$. We want to take a closer look into the temperature-dependence of the magnon decay length in Sec. 4.1.3. These small variation in the magnon decay length for different distances is in good agreement with recent findings in Ref. [58]. They observed that the LPE-YIG thickness has no a large influence on the electrical magnon decay length and it increases only slightly with increasing YIG thickness. For the thermal magnon decay length we observe a rather constant behaviour (see Fig. 4.6) within the errorbars. The extracted value of $\lambda_{\mathrm{m,th}} \approx 3.5\,\mathrm{µm}$ for our $22\,\mathrm{nm}$ thin LPE-YIG film is slightly smaller compared to $\lambda_{\mathrm{m,th}} = 6.7\,\mathrm{µm}$ for a $t_{\mathrm{YIG}} = 1\,\mathrm{µm}$ thick LPE-YIG film and $\lambda_{\mathrm{m,th}} = 9\,\mathrm{µm}$ for a $t_{\mathrm{YIG}} = 2\,\mathrm{µm}$ thick film at $200\,\mathrm{K}$ respectively [16, 32]. Furthermore they observe a decrease of $\lambda_{\mathrm{m,th}}$ for increasing magnetic field, which we do not observe in our measurements. One possible explanation could be that the decrease of $\lambda_{\mathrm{m,th}}$ is not observable within our large error bars. More experiments with larger electrode separations are required to corroborate this assumption.

4.1.3 Temperature-dependence of the magnon transport signals

To conclude this section we want to take a closer look at the temperature-dependence of the magnon transport in our $22\,\mathrm{nm}$ LPE-YIG thin film. To this end, we perform an angle dependent magnon transport experiment over a temperature range from $T = 30\,\mathrm{K}$ to $280\,\mathrm{K}$. The magnetic field is kept constant at $\mu_0 H_{\mathrm{ext}} = 50\,\mathrm{mT}$. In Fig. 4.7 the electrical and thermal magnon transport signals $U^{\mathrm{el}}_{\mathrm{det}}$ and $U^{\mathrm{th}}_{\mathrm{det}}$ are shown as a function of the in-plane rotation angle φ.

Panel (a) shows the electrical magnon transport signals measured at four different temperatures between $T = 30\,\mathrm{K}$ and $T = 250\,\mathrm{K}$. We observe the expected $\cos^2\varphi$ dependence of $U^{\mathrm{el}}_{\mathrm{det}}$ as a function of the magnetic field orientation for $T = 100\,\mathrm{K}$, $200\,\mathrm{K}$ and $250\,\mathrm{K}$. For $T = 250\,\mathrm{K}$ we exemplarily show a fit to the data using Eq. (48). With decreasing temperature the electrical magnon transport signal shows a clear decrease. And for $T = 30\,\mathrm{K}$ the $\cos^2\varphi$ dependence can not be observed anymore. This behaviour is consistent with previous measurements reported in literature [8, 16, 60]. For decreasing temperatures the thermally activated magnon population below the injector electrode decreases, leading to a decreased transfer efficiency for angular momentum accross the Pt/YIG interface [60]. For this reason, a smaller magnon transport signal is observed at the detector electrode for decreasing temperatures [60]. A further contribution to the temperature-dependence of the magnon transport signal could be a temperature-dependence of the spin decay length $\lambda_{\mathrm{m,el}}$. We discuss this in more detail in the upcoming part of this section.

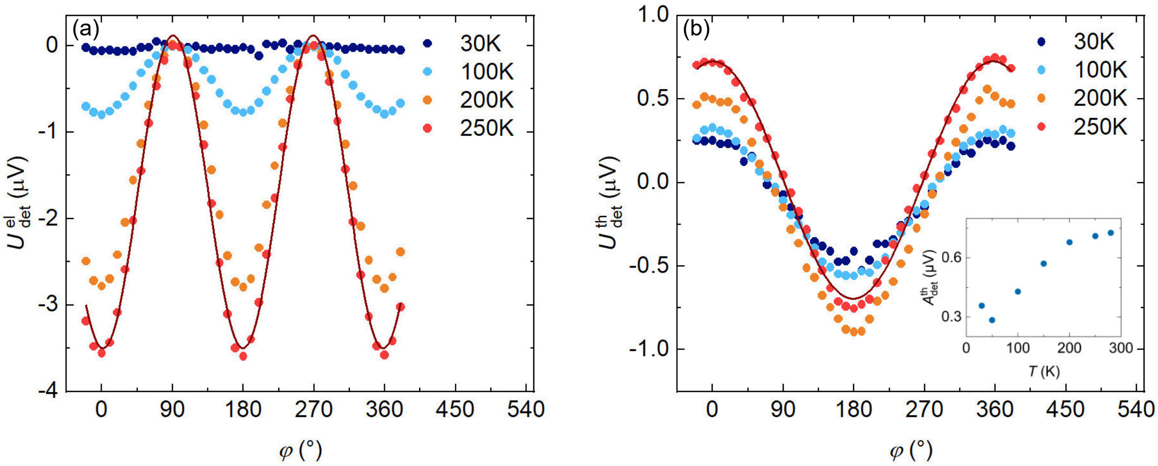

Figure 4.7: Magnon transport signal measured at the detector electrode as a function of the magnetic field orientation. The measurements are conducted at a magnetic field of $\mu_0 H = 50\,\mathrm{mT}$ and a distance of $d = 900\,\mathrm{nm}$ between injector and detector for different temperatures. (a) Electrical magnon transport signal caused by SHE as a function of the magnetic field orientation. The red solid line shows a fit to the data using Eq. (48). (b) Thermal magnon transport signal caused by SSE. The red solid line is a fit to Eq. (49). The inset shows the amplitudes of the thermal magnon transport signal measured at the detector electrode as a function of the temperature.

The thermal magnon transport signals $U^{\mathrm{th}}_{\mathrm{det}}$ are shown in Fig. 4.7 (b). We observe a $\cos\varphi$ dependence for all temperatures in the measured temperature range, even for $T = 30\,\mathrm{K}$ where no electrical contribution is observable anymore. The red solid line shows a fit to the data using Eq. (49) for a temperature of $T = 250\,\mathrm{K}$. In the inset we show the extracted magnon transport amplitude $A^{\mathrm{th}}_{\mathrm{det}}$ as a function of the temperature. Similar to the electric contribution, the amplitudes $A^{\mathrm{th}}_{\mathrm{det}}$ of the thermal magnon transport signal decrease for decreasing temperatures down to $T = 50\,\mathrm{K}$. For even lower temperatures however, the magnon transport amplitude seems to increase again. This behaviour is in contrast to the temperature-dependence of the thermally biased magnon transport amplitude for a $2\,\mu\mathrm{m}$ thick LPE-YIG film at a comparable external magnetic field of $\mu_0 H = 30\,\mathrm{mT}$, reported in Ref. [16]. They observe a monotonous increase of $A^{\mathrm{th}}_{\mathrm{det}}$ for decreasing temperature and a strong increase below $T = 150\,\mathrm{K}$ for all measured electrode separations ($d = 3\,\mu\mathrm{m}$ to $20\,\mu\mathrm{m}$). For smaller distances d the increase in $A^{\mathrm{th}}_{\mathrm{det}}$ seems to be even more pronounced [16]. As the thermal gradient generated by Joule heating at the injector electrode is very sensitive to various parameters such as the specific heat or the thermal conductivity at low temperatures, it is hard to pinpoint what dominates the temperature-dependence of SSE magnon generation. What we can infer from our measurements is that the thickness of the YIG film seems to play an important role for the temperature-dependence of the magnon transport amplitude $A^{\mathrm{th}}_{\mathrm{det}}$. Independent of the magnon generation, also the thermal magnon decay length $\lambda_{\mathrm{m,th}}$ can be temperature dependent.

In the following we want to disentangle the temperature-dependence of magnon generation/detection and magnon propagation for electrically and thermally driven magnons and take a closer look at the corresponding magnon decay lengths $\lambda_{\mathrm{m,th}}$ and $\lambda_{\mathrm{m,el}}$. We also do not observe a strong increase in $A^{\mathrm{th}}_{\mathrm{det}}$ for a larger electrode separation ($d = 3\,\mu\mathrm{m}$ and $d = 3.5\,\mu\mathrm{m}$) and thus can rule out a smaller distance d to cause the discrepancy to literature in our experiments. To this end, we extract the electrical and thermal amplitudes $A^{\mathrm{el}}_{\mathrm{det}}$ and $A^{\mathrm{th}}_{\mathrm{det}}$ from the angle dependent measurements as a function of the electrode separation within a temperature range from $T = 50$ to $280\,\mathrm{K}$. The electrical magnon transport amplitude is shown semi-logarithmically as a function of the edge-to-edge distance d between the injector and detector electrode for three selected temperatures (see Fig. 4.8(a)). In Fig. 4.8(a) we observe an increase in $A^{\mathrm{el}}_{\mathrm{det}}$ for increasing temperature which seems to be equivalent for all measured distances. This becomes clear by fitting the distance-dependence for each temperature with Eq. (50) (solid lines). [1)] As λ_{m} enters only in the exponent of Eq. (50), interface effects are excluded, which allows to disentangle the temperature-dependence of the magnon decay length and the temperature dependent contribution of the interface. As the fits in Fig. 4.8(a) are nearly parallel lines for all three cases the magnon decay length seems to be similar and thus only weakly dependent on the temperature. The offset on the other hand is related to the contribution of the magnon transport signal that is dominated by the Pt/YIG interface.

[1)] Note that as already shown in Fig. 4.4 we observe a deviation from the exponential decay at $d = 3.5\,\mu\mathrm{m}$ and $d = 3\,\mu\mathrm{m}$ for all temperatures. Combined with the magnetic field-dependence results, this confirms that this behaviour is due to the structure itself and is not related to magnon transport.

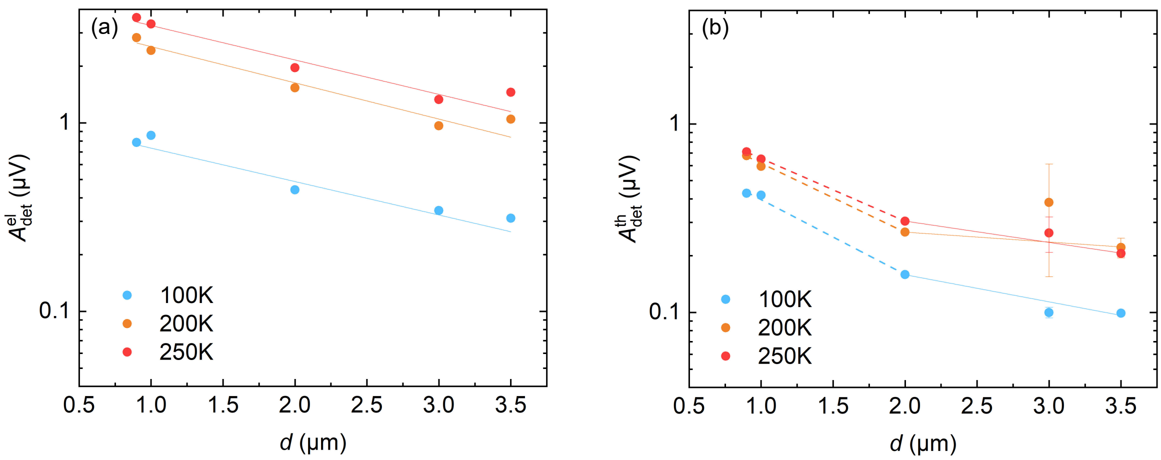

Figure 4.8: Amplitudes of the magnon transport signal measured at the detector electrode as a function of the distance d between injector and detector. The measurements are conducted at a magnetic field of $\mu_0 H = 50\,\mathrm{mT}$ for different temperatures. (a) The amplitudes $A_{\mathrm{det}}^{\mathrm{el}}$ are extracted from the electrical magnon transport signal and the solid lines represent an exponential decay function from Eq. (50). (b) The amplitudes $A_{\mathrm{det}}^{\mathrm{th}}$ are extracted from the thermal magnon transport signal and the solid lines (large distances) and dashed lines (small distances) represent an exponential decay function using Eq. (50).

The latter contribution can be approximated by extrapolating the exponential fits to $d = 0\,\mu\mathrm{m}$. In Fig. 4.9 A_0^{el} is shown as a function of the temperature. We observe a linear decrease in A_0^{el} for decreasing temperature, which is caused by the decreasing number of thermally activated magnons at the Pt/YIG interface as discussed above. The number of magnons should scale with $T^{\frac{3}{2}}$, since we need to account for the injection and detection, one would then naively expect a scaling of A_0^{el} with T^2. This is only in very rough agreement with the observed temperature-dependence. The strong temperature-dependence of A_0^{el} corroborates the assumption that the temperature-dependence of the electrical magnon transport signal $U_{\mathrm{det}}^{\mathrm{el}}$ in Fig. 4.7(a), is dominated by the Pt/YIG interface transparency and not by a change in the magnon decay length λ_{m}.
For the thermal magnon transport signal $A_{\mathrm{det}}^{\mathrm{th}}$ a similar analysis is shown in Fig. 4.8(b). A_{det} decreases for increasing distance d. Here we observe two different regimes, that can both be described by an exponential decay. For electrode separations $d \leq 2\,\mu\mathrm{m}$ the signal decreases much stronger with d than for larger distances $d \geq 2\,\mu\mathrm{m}$. We follow the same procedure as before and extract the thermal magnon decay length by fitting the datapoints for $d \geq 2\,\mu\mathrm{m}$. For more precise extraction of the evolution of the thermal magnon transport signal shown in Fig. 4.8 and the magnon decay length we require measurements at larger distances than $d = 3.5\,\mu\mathrm{m}$. For comparison: The group of B.J. van Wees made measurements up to $d = 10\,\mu\mathrm{m}$ in Ref. [61]. They used different YIG-thicknesses and also observed two exponential decay regimes for thinner YIG layers. The transition from these two regimes is located at around $d = 1.5\,\mu\mathrm{m}$ for a $210\,\mathrm{nm}$ thick YIG film. This is very similar to our observation here. Moreover, this suggests that we need to study even larger distances to extract a representative value for our magnon decay length. Unfortunately that could not be implemented as a part of this thesis. The structures on the samples were also needed to conduct electrical and optical measurements on three-strip structures, such

that the limited number of two-strip devices provided us with a smaller range of distances to investigate. Furthermore by assuming that we are only able to detect an amplitude with minimum $A_{\mathrm{det}} \approx 25\,\mathrm{nV}$ due to the signal to noise in our setup, the maximum distance we would expect to still be able to analyse for the lowest temperature is $d = 6\,\mu\mathrm{m}$. Fig. 4.9 also shows A_0^{th} as a function of the temperature for both analysed distance regimes. The electrical amplitude A_0^{el} is starting at about the same amplitudes for $T = 50\,\mathrm{K}$ like both thermal distance regime amplitudes. For A_0^{el} we observe an increase of about $5\,\mu\mathrm{V}$ with increasing temperatures. Instead of that A_0^{th} has almost no observable change with temperature. As expected from the distance-dependence in Fig. 4.8, A_0^{th} for $d \geq 2\,\mu\mathrm{m}$ is smaller than A_0^{th} for the small distance regime. The datapoint for the thermal amplitudes at $T = 150\,\mathrm{K}$ are not shown because it wasn't possible to fit an exponential decay via Eq. (50) to the thermal amplitudes $A_{\mathrm{det}}^{\mathrm{th}}$ at $T = 150\,\mathrm{K}$.

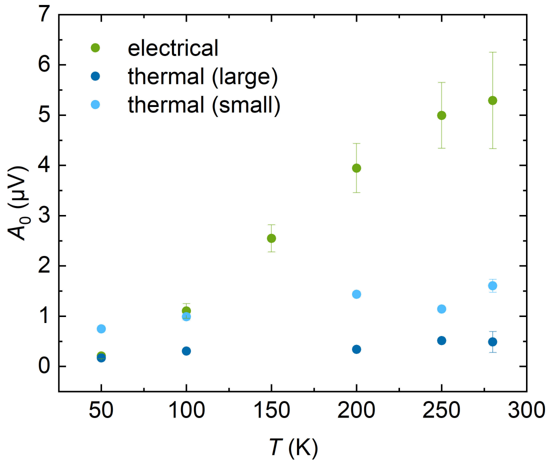

Figure 4.9: Extrapolated electrical and small and large distance regime thermal amplitudes of the magnon transport signals measured at the detector electrode as a function of the temperature. The measurements are conducted at a magnetic field of $\mu_0 H = 50\,\mathrm{mT}$.

In Fig. 4.10 we show the magnon decay length λ_{m} for electrically and thermally induced magnons as a function of the temperature for the whole measured temperature range from $T = 50\,\mathrm{K}$ to $280\,\mathrm{K}$. They are extracted from the fit function Eq. (50) for the different temperatures in Fig. 4.8. Analogous to A_0^{th}, $\lambda_{\mathrm{m}}^{\mathrm{th}}$ could not be extracted for $T = 150\,\mathrm{K}$ and is therefore missing. The thermal magnon decay length for $d \geq 2\,\mu\mathrm{m}$ is by a factor of 1.5 larger than the electrical one. The evolution of $\lambda_{\mathrm{m}}^{\mathrm{th}}$ and $\lambda_{\mathrm{m}}^{\mathrm{el}}$ with temperature is quite similar. Within the errorbars we observe a slight increase for an increasing temperature with a small plateau between $T = 150$ and $200\mathrm{K}$. Analogous to A_0^{th} the thermal magnon decay length for $d \leq 2\,\mu\mathrm{m}$ is smaller than for the large distance regime.

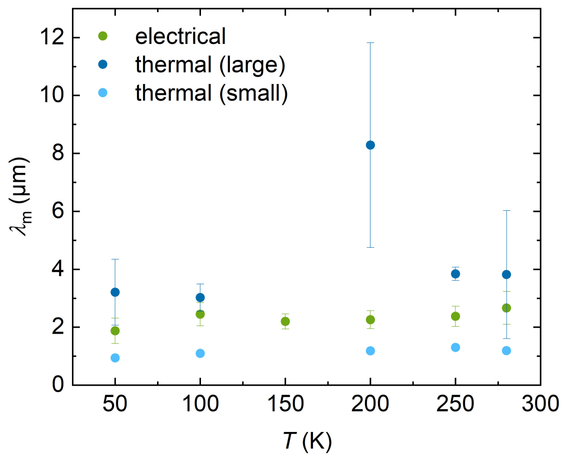

Figure 4.10: Magnon decay length λ_{m} as a function of the temperature. Extracted from the exponential decay fits with Eq. (50) of the electrical and small and large distance regime thermal amplitudes at a magnetic field of $\mu_0 H = 50\,\mathrm{mT}$ for different distances between injector and detector at different temperatures.

The observed temperature-dependence of the electrical magnon decay length is in good agreement with the results for a $5.9\,\mathrm{nm}$ and $7.9\,\mathrm{nm}$ thick LPE-YIG film reported in literature [58] with an comparable external magnetic field of $\mu_0 H = 10\,\mathrm{mT}$. They observed a slight increase of $\lambda_{\mathrm{m,el}}$ with temperature of about $\Delta\lambda_{\mathrm{m,el}} = 0.5\,\mathrm{\mu m}$ from $T = 100\,\mathrm{K}$ to $T = 300\,\mathrm{K}$. For increasing temperature we assume an enhanced magnon-phonon scattering as more phonon states are occuppied due to the higher thermal energy in the system. As magnons are not a conserved quantity in our experiments, magnon phonon scattering can lead to the annihilation of a magnon and thus a decreased magnon lifetime τ_m [60]. As the observed change in the magon decay length with temperature in Fig. 4.10 is rather small we infere that the diffusion constant D_{m} in $\lambda_{\mathrm{m}} = \sqrt{D_{\mathrm{m}}\tau_{\mathrm{m}}}$ increaseses with increasing temperature and nearly compensates the decrease in magnon lifetime τ_{m}. A similar behaviour was observed for a thicker film of $t_{\mathrm{YIG}} = 210\,\mathrm{nm}$ with an increase in $\lambda_{\mathrm{m,el}}$ and $\lambda_{\mathrm{m,th}}$ of about $\approx 2\,\mathrm{\mu m}$ [60]. Within the errorbars they report similar values for electrical and thermal decay length over the measured temperature range and thus observed no indication for different transport mechanisms for the two excitation methods [60]. In contrast, we observe a thermal magnon decay length that is a factor of 1.5 larger compared to the electrical decay length in our ultrathin $22\,\mathrm{nm}$ LPE-YIG film. A discrepancy between electrical and thermal magnon decay lengths was up to now only observed and discussed in a thick LPE-YIG film with $t_{\mathrm{YIG}} = 2\,\mathrm{\mu m}$ [16]. In agreement to our measurements they observed a thermal magnon decay length that exceeds the electrical magnon decay length over the whole measured temperature range from $T = 100\,\mathrm{K}$ to $300\,\mathrm{K}$ and indicates a different diffusion and relaxation mechanism of the thermally and electrically excited magnons, depending on their generation mechanism at the Pt/YIG interface [16]. Their experiments were conducted under an external field of $\mu_0 H = 30\,\mathrm{mT}$ and they report a $\lambda_{\mathrm{m,th}}$ that is about twice the size of $\lambda_{\mathrm{m,el}}$. One possible explanation is, that electrical and thermal magnon transport is carried by different nonequilibrium magnon distribution in terms of their frequency, group velocity and lifetime [16]. Although we assumed from the field-dependence of the magnon decay length in Chapter 4.1.2 that sub-thermal magnons dominantly contribute to the electrical and thermal magnon transport, the difference in $\lambda_{\mathrm{m,th}}$ and $\lambda_{\mathrm{m,el}}$ could be an indication that the non-equilibrium distribution of the magnons depends on their generation mechanism.

4.1.4 Summary

In this section we discussed the measurements for two-terminal structures on the $22\,\mathrm{nm}$ YIG film. We observe an influence of the distance between the injector and detector electrode on the electrical and thermal magnon transport signals: The signal strength is increasing for a decreasing distance (see Section 4.1.1). This distance-dependence remains unchanged for different magnetic fields. Analysing the magnon transport signal also at changing magnetic fields we observed a magnetic field-dependence: By decreasing the external magnetic field the magnon transport signal gets stronger and we get a larger magnon decay length for small magnetic fields (see Section 4.1.2). As a final analysis of the two-strip structures we took a look at the magnon transport at different temperatures which results in an temperature-dependence: At a certain temperature the electrical transport vanishes, increasing the temperature from that point also the magnon transport signal is increasing and we get larger magnon decay lengths for larger temperatures (see Section 4.1.3). These observations, the extracted parameters like the magnon decay lengths and their dependence on magnetic field and temperature for our sample are in good agreement with existing literature values. They underline the suitability of our thin LPE-YIG sample for future all-electrical magnon transport experiments.

4.2 Electrical modulation of magnon spin transport in yttrium iron garnet

In this section we focus on electrical magnon transport measurements conducted on three-strip structures on a $22\,\mathrm{nm}$ thick LPE-YIG films. Magnons are injected at the injector electrode via SHE and propagate to the detector electrode and detected as the first harmonic voltage signal $U_{1\omega}$ via a lock-in detection scheme (see Section 3.2.2). We especially want to discuss the influence of an additional DC-charge current I_{mod} applied at the modulator electrode and have a look at the critical current for different magnetic fields in the range of $\mu_0 H = 10\,\mathrm{mT}$ to $\mu_0 H = 55\,\mathrm{mT}$ (which represents the magnetic field range accessible in the BLS setup).
We start with an angle-dependent measurement at a temperature of $T = 280\,\mathrm{K}$. The width of the injector and detector electrode is $w = 500\,\mathrm{nm}$, the modulator electrode is centered symetrically within the two outer electrodes and has a width of $w_{\mathrm{m}} = 600\,\mathrm{nm}$ and an edge-to-edge distance to injector/detector of $d_{\mathrm{m}} = 200\,\mathrm{nm}$. During the measurements we keep the magnetic field magnitude fixed at $\mu_0 H = 55\,\mathrm{mT}$ and apply different modulator currents I_{mod}. Fig. 4.11 shows the electrical magnon transport signal as a function of the magnetic field orientation. Panel (a) shows the magnon transport signal for positive modulator currents $I_{\mathrm{mod}} > 0\,\mu\mathrm{A}$. For $I_{\mathrm{mod}} = 0\,\mu\mathrm{A}$ we observe a $\cos^2\varphi$ dependent electrical magnon transport signal, which we already discussed in the previous Section 4.1. Compared to the two-terminal structure with similar edge-to-edge distance the electrical magnon tranpsort is slightly decreased by $65\,\%$ as the modulator strip between injector and detector also acts as a magnon sink. The effect is however small enough to allow for magnon spin transport

between injector and detector. For $I_{\mathrm{mod}} = 200\,\mu\mathrm{A}$ to $1\,\mathrm{mA}$ we observe an increase of the magnon transport signal with increasing charge current around $\varphi = 180°$ compared to the $0\,\mu\mathrm{A}$ signal. For the angles $\varphi = 0°$ and $360°$ the magnon transport signal is unchanged for $I_{\mathrm{mod}} = 200\,\mu\mathrm{A}$ and $600\,\mu\mathrm{A}$ and shows a small increase for $I_{\mathrm{mod}} = 1\,\mathrm{mA}$. To understand this behaviour we can consider Fig. 2.7 in Section 2.5. For $\varphi = 180°$ and a positive DC-charge current applied at the modulator the spin orientation in the Pt induced by the SHE is parallel to the magnetization direction in the YIG. In this configuration a magnon accumulation is excited beneath the modulator electrode via the SHE [13]. This results in an increased magnon density, represented by the magnon chemical potential μ, and thus an increased magnon spin conductivity [4]. Furthermore the finite resistance of the Pt electrode leads to Joule heating. Via the SSE and the finite temperature increase thermal magnons are excited below the modulator electrode. For the $180°$-shifted case ($\varphi = 0°, 360°$) we get an antiparallel orientation of spin orientation in Pt and magnetization in YIG, which causes a decrease in the magnon density and thus we would expect a decrease of the magnon transport signal compared to the signal for $I_{\mathrm{mod}} = 0\,\mu\mathrm{A}$. This is not observed in Fig. 4.11. We attribute this observation to the angle independent injection of thermal magnons due to Joule heating that counteract the magnon depletion due to the SHE [4]. For $I_{\mathrm{mod}} = 1\,\mathrm{mA}$ we even observe a dominant Joule heating contribution in Fig. 4.11(a) resulting in an increased magnon spin conductivity and thus a larger magnon transport signal compared to $I_{\mathrm{mod}} = 0\,\mathrm{mA}$.

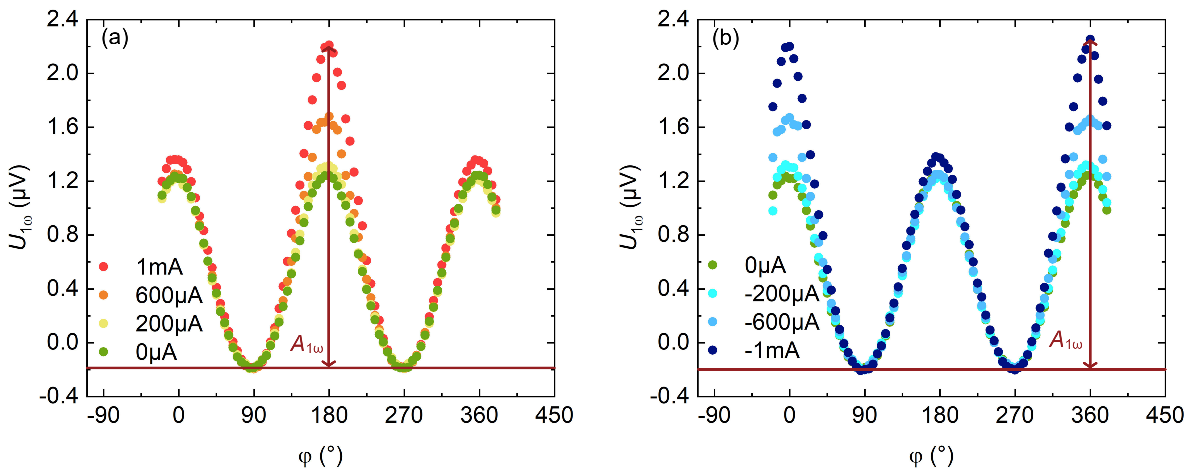

Figure 4.11: Electrical magnon transport signal as a function of the magnetic field orientation. The measurements are conducted at a magnetic field of $\mu_0 H = 55\,\mathrm{mT}$, a temperature of $T = 280\,\mathrm{K}$ and for a modulator width of $w_{\mathrm{m}} = 600\,\mathrm{nm}$ with distance $d_{\mathrm{m}} = 200\,\mathrm{nm}$ to the injector and detector electrode. (a) Magnon transport signal for positive applied charge currents at the modulator, with amplitude $A_{1\omega}$. (b) Magnon transport signal for negative applied charge currents at the modulator, with amplitude $A_{1\omega}$.

Fig. 4.11 (b) shows the electrical magnon transport for negative modulator currents $I_{\mathrm{mod}} < 0\,\mu\mathrm{A}$ as a function of the magnetic field orientation. Analogous to panel (a) the green datapoints show the $\cos^2\varphi$ dependent magnon transport signal for $I_{\mathrm{mod}} = 0\,\mu\mathrm{A}$. For $\varphi = 0°$ and $\varphi = 360°$ we observe an increasing amplitude with increasing negative current I_{mod} while the signal keeps unchanged at $\varphi = 180°$ for $I_{\mathrm{mod}} = -200\,\mu\mathrm{A}$ and $-600\,\mu\mathrm{A}$. Again a small increase can be observed at $\varphi = 180°$ for $I_{\mathrm{mod}} = -1\,\mathrm{mA}$. Panel

(b) is in general shifted by $180°$ in φ as compared to Fig. 4.11(a). Due to the negative polarity of the applied DC-charge current magnons are injected for $\varphi = 0°$ and $360°$ at the modulator electrode, due to SHE and Joule heating, while a magnon depletion via SHE occurs at $\varphi = 180°$ that is counterbalanced by Joule heating. Our results are in good agreement with previous measurements made on $t_{\mathrm{YIG}} = 13.4\,\mathrm{nm}$ PLD-YIG films in Ref. [4, 5, 47]. Their magnon transport signals for positive and negative I_{mod} are $180°$ shifted compared to our data due to an $180°$ rotated coordinate system. The increase of the amplitude for s $\parallel$ $\mathbf{m}_{\mathrm{YIG}}$ with increasing modulator current is consistent. They observed a rather triangular shape of the magnon transport for $I_{\mathrm{mod}} = 0\,\mu\mathrm{A}$ due to the cubic magnetocrystalline anisotropy of the YIG, which was not observed in our $22\,\mathrm{nm}$ thick LPE-YIG film. This can be explained by the extremely small IP magnetocristalline anisotropy of our LPE-YIG film of $\mu_0 H_{\mathrm{ani}} = (1.02 \pm 0.35)\,\mathrm{mT}$, observed in Ferromagnetic Resonance (FMR) measurements. As a comparison, the LPE-YIG film used in Ref [5] has an anasotropy field of $\mu_0 H_{\mathrm{ani}} = (9.54 \pm 2.13)\,\mathrm{mT}$. This difference can be attributed to the two different orientations of the YIG layer. For our LPE-YIG sample we use (111)-oriented YIG, which exhibits vanishing contributions from magnetocrystalline magnetic ansiotropy within the film plane. For the PLD grown YIG in Refs. [4, 5, 47] a (100)-orientation is used, which gives rise to a finite contribution from magnetocrystalline anisotropy in the film plane. By comparing the strength of the magnon transport signal, in our measurements we observe a by a factor of about 4 larger signal for $I_{\mathrm{mod}} = 0\,\mu\mathrm{A}$, which is mainly to the different distances between the injector and detector electrode. While we are using a structure with an edge-to-edge distance between injector/detector and modulator of $d_{\mathrm{m}} = 200\,\mathrm{nm}$, in Ref. [4, 5] a structure with $d_{\mathrm{m}} = 400\,\mathrm{nm}$ was used. For a three-terminal structure with a modulator width of $w_{\mathrm{m}} = 500\,\mathrm{nm}$ they show an enhancement of a factor of 2.7 for $I_{\mathrm{mod}} = 750\,\mu\mathrm{A}$ compared to the case of vanishing applied modulator current. From Fig. 4.11 we can report a modulation factor of only 1.83 for an even higher applied modulator current of $I_{\mathrm{mod}} = 1\,\mathrm{mA}$. To compare these two different devices, we have to use the current density $j_{\mathrm{mod}} = \frac{I_{\mathrm{mod}}}{t_{\mathrm{Pt}} \cdot w_{\mathrm{m}}}$ that is dependent of the dimensions of the modulator. The structure used in Ref. [5] has a $w_{\mathrm{m}} = 500\,\mathrm{nm}$ wide modulator with a thickness of $t_{\mathrm{Pt}} = 3.5\,\mathrm{nm}$. This results in a current density of $j_{\mathrm{mod}} = 4.28 \cdot 10^{11}\,\mathrm{A/m^2}$ for $750\,\mu\mathrm{A}$ modulator current. In contrast, the structure used for the measurements shown in Fig. 4.11 has a modulator with $w_{\mathrm{m}} = 600\,\mathrm{nm}$ and $t_{\mathrm{Pt}} = 7\,\mathrm{nm}$ and thus a current density of only $j_{\mathrm{mod}} = 2.38 \cdot 10^{11}\,\mathrm{A/m^2}$ within the modulator for $1\,\mathrm{mA}$. Thus the corresponding spin current generated in the Pt modulator is in our case about a factor of 2 smaller as in Refs. [4, 5] and might already explain the observed differences in the enhancement factors.

To investigate the modulator current-dependence of the magnon transport signal further we extract the amplitudes $A_{1\omega}$ for s $\parallel$ $\mathbf{m}_{\mathrm{YIG}}$ for positive and negative currents which results in positive and negative magnetic fields from Fig. 4.11 as a function of the modulator current and analyze them with respect to the critical currents. This is done by measuring the magnon transport signal as a function of the modulator current I_{mod} for the external magnetic field oriented along $\varphi = 180°$ for $\mu_0 H > 0\,\mathrm{mT}$ and $\varphi = 0°$ for $\mu_0 H < 0\,\mathrm{mT}$ where we expect the maximum mangon transport signal. Subsequently we subtract the magnon transport signal for the external magnetic field pointing along the x-direction ($\varphi = 270°$) where the magnon transport signal is vanishing to correct for a possible offset unrelated to magnon transport.

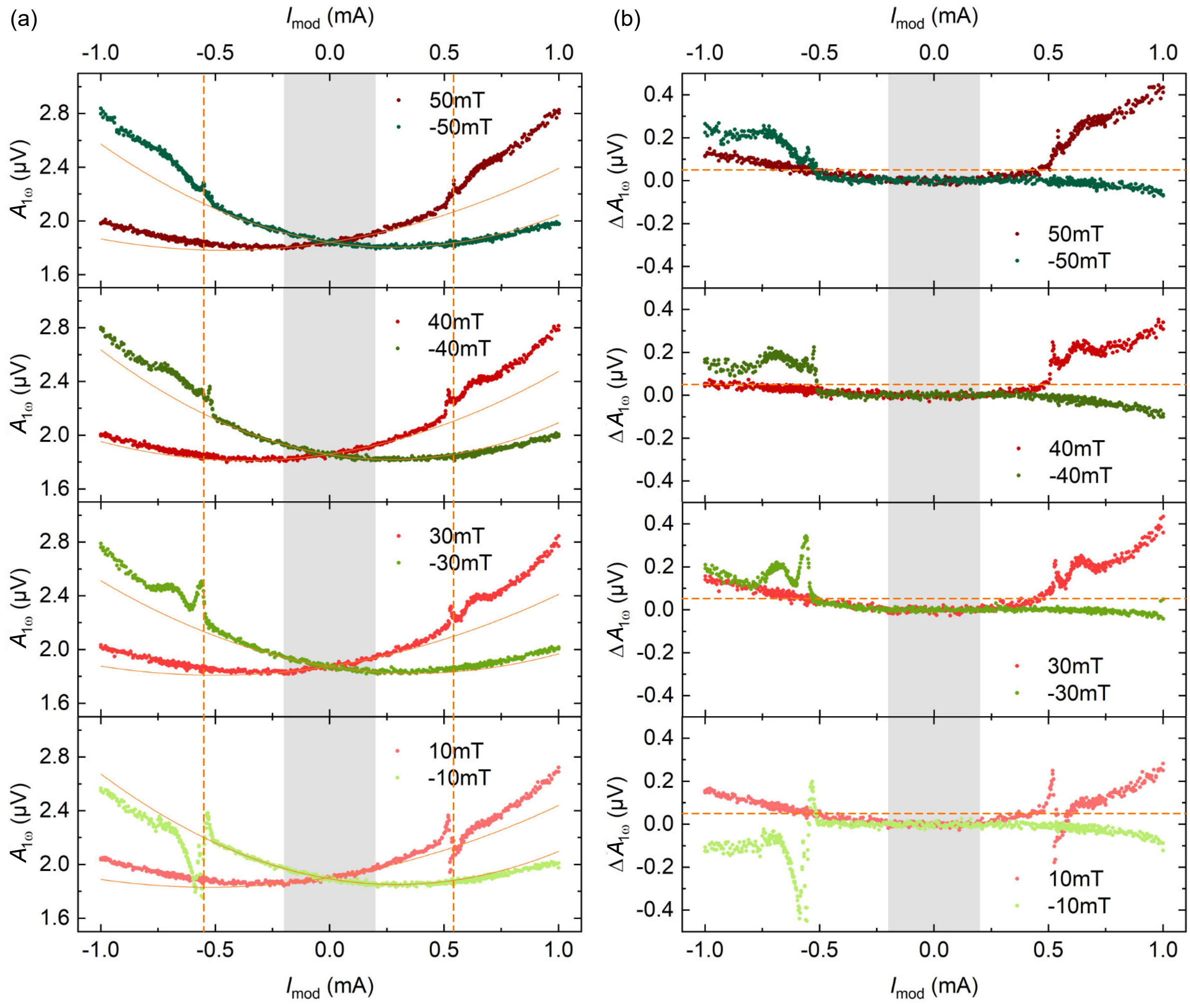

Figure 4.12: (a) Electrical magnon transport signal as a function of the applied DC-charge current at the modulator. For a charge current of $I_{\mathrm{mod}} = -200\,\mu\mathrm{A}$ to $200\,\mu\mathrm{A}$ (grey area) the data is fitted to Eq. (51) shown as orange solid line. The fit curve is extrapolated over the whole measurement range. Vertical dashed orange lines are guides to the eye. (b) Difference between the magnon transport signal and the fit function in (a) as a function of the applied charge current at the modulator. The condition for the critical current is marked (orange dashed line). All measurements are conducted at a temperature of $T = 280\,\mathrm{K}$ for a modulator width of $w_{\mathrm{m}} = 600\,\mathrm{nm}$ with distance $d_{\mathrm{m}} = 200\,\mathrm{nm}$ to the injector and detector electrode for different magnetic fields.

Fig. 4.12 (a) shows the electrical magnon transport amplitude as a function of the modulator charge current at a temperature of $T = 280\,\mathrm{K}$ for different magnetic fields. We again used the three-terminal structure with a modulator width of $w_{\mathrm{m}} = 600\,\mathrm{nm}$, an injector and detector width of $w = 500\,\mathrm{nm}$ and an edge-to-edge distance between the two outer electrodes of $d = 1\,\mu\mathrm{m}$. The electrical magnon transport amplitude $A^{\mathrm{el}}_{\mathrm{det}}$ is shown for positive (red) and negative (green) magnetic fields as a function of the modulator current ranging from $I_{\mathrm{mod}} = -1\,\mathrm{mA}$ to $1\,\mathrm{mA}$. In agreement to the angle dependent measurements we observe a strong increase in the magnon transport signal $A^{\mathrm{el}}_{\mathrm{det}}$ with increasing positive modulator current $I_{\mathrm{mod}} > 0\,\mathrm{mA}$ for $+\mu_0 H$ and an increasing $A^{\mathrm{el}}_{\mathrm{det}}$ with increasing negative modulator current $I_{\mathrm{mod}} < 0\,\mathrm{mA}$ for $-\mu_0 H$. The modulation of $A^{\mathrm{el}}_{\mathrm{det}}\,(\pm I_{\mathrm{mod}})$ seems to be quite symmetric for corresponding magnetic fields $\pm\mu_0 H$. In the low current bias regime

$|I_{\mathrm{mod}}| \leq 0.2\,\mathrm{mA}$ (indicated by the light grey area in Fig. 4.12) the current-dependence can be described by a superposition of a linear (SHE) and a quadratic (Joule heating) contribution (see Section 2.5) [4]. As the magnon transport signal is proportional to the magnon conductivity we fit the data in Fig. 4.12(a) using

$$A_{1\omega} = A_{1\omega 0} + \Delta R_{\mathrm{SHE}} I_{\mathrm{mod}} + \Delta R_{\mathrm{th}} I_{\mathrm{mod}}^2, \tag{51}$$

within the low current bias regime $|I_{\mathrm{mod}}| \leq 0.2\,\mathrm{mA}$. The linear coefficient $\Delta R_{\mathrm{SHE}} = \frac{\Delta\sigma_{\mathrm{SHE}}}{\sigma_{\mathrm{m}}^0} A_{1\omega 0}$ corresponds to the efficiency of the SHE based modulation and the quadratic coefficient $\Delta R_{\mathrm{th}} = \frac{\Delta\sigma_{\mathrm{th}}}{\sigma_{\mathrm{m}}^0} A_{1\omega 0}$ to the efficiency of the thermal modulation effect [4, 5, 47]. The parameter $A_{1\omega 0}$ accounts for the unmodulated magnon transport amplitude at $I_{\mathrm{mod}} = 0\,\mu\mathrm{A}$. This fit is extrapolated for the whole current range and shown for all magnetic fields in Fig. 4.12 (a) (orange solid line) (the fit parameters are shown in the appendix in Tab. A.3). Within $|I_{\mathrm{mod}}| \leq 0.2\,\mathrm{mA}$ the magnon transport signal can be perfectly described with the fitted quadratic and linear dependence very well. For positive fields we observe a distinct deviation from the fit curve for all magnetic field magnitudes in Fig. 4.12(a). Furthermore we observe that the peak value of this deviation seems to shift for different magnetic fields (the vertical orange dashed lines are guides to the eye). For negative fields we observe the same behaviour. This deviation corresponds to a zero effective damping state below the modulator where the magnetic damping of the YIG film is fully compensated by the spin-orbit torque induced at the modulator at a critical current value I_{crit} (see Section 2.5) [4, 47]. Thus the magnon lifetime τ_{m} is diverging and the magnon conductivity is increased [47]. This results in the drastic increase of the magnon transport signal measured at the detector. These observations are consistent with previous measurements on $13.4\,\mathrm{nm}$ and $11.4\,\mathrm{nm}$ LPE-YIG films in Refs. [4, 5] and Ref. [47], respectively. Looking at the orange dashed line in Fig. 4.12(a) for our measurements the value for I_{crit} seems not to show a strong magnetic field-dependence while in Refs. [4, 5] an increase in I_{crit} for increasing magnetic fields was observed. At present we lack enough data to fully explain this discrepancy. Yet, one important difference between our present measurements and the ones in Refs. [4, 5, 47] is the magnetic field range investigated. In the previous works magnetic fields of up to $200\,\mathrm{mT}$ were applied, while we restricted ourselves to a maximum magnetic field of $55\,\mathrm{mT}$, to probe the same field range as available in the BLS setup. When looking into the previous results of Refs. [4, 5, 47], a clear magnetic field-dependence is only observed for large magnetic fields exceeding $50\,\mathrm{mT}$. Thus it may be that measurements with larger magnetic fields will provide a stronger change of I_{crit}.

We now take a closer look on the analysis of the critical current regime. This is done by substracting the fit from the measurement data in Fig. 4.12(a) using:

$$\Delta A_{1\omega} = A_{1\omega} - \left(A_{1\omega 0} + \Delta R_{\mathrm{SHE}} I_{\mathrm{mod}} + \Delta R_{\mathrm{th}} I_{\mathrm{mod}}^2\right). \tag{52}$$

The resulting difference $\Delta A_{1\omega}$ is shown in Fig. 4.12(b) as a funtion of the applied charge current at the modulator electrode I_{mod} for different positive and negative magnetic fields. We observe a vanishing difference $\Delta A_{1\omega}$ for all magnetic fields up to a modulator current of around $I_{\mathrm{mod}} = \pm 0.4\,\mathrm{mA}$ for positive and negative magnetic fields, respectively. Which means we could also have defined the low current bias regime for this structure similar to Ref. [5] by $|I_{\mathrm{mod}}| \leq 0.4\,\mathrm{mA}$. By keeping in mind that we made the described measurement for several structures with different dimensions and want to compare those to each other we adhere to the smaller current range for our fits via Eq. (51). For larger I_{mod} we observe an increase of $\Delta A_{1\omega}$ with following saturation for large (small) currents at positive (negative) magnetic fields (excluding our measurements at $\pm 10\,\mathrm{mT}$. This behaviour is again consistent with the results in Refs. [4, 5, 47]. We define the critical current I_{crit} at which the magnetic damping is compensated as the threshhold $\Delta A_{1\omega}\,(I_{\mathrm{mod}}) > 0.05\,\mathrm{\mu V}$, indicated by the orange dashed lines ins Fig. 4.12(b). We discuss this choice further later in this section. We can see that this threshold is fullfiled in the critical current regime of the respective field direction, but that there is an additional crossing for large negative modulator currents for $+\mu_0 H$ (red datapoints). For this configuration we would expect Joule heating magnon injection at the modulator that is counterbalanced by SHE induced magnons and thus a purely $I_{\mathrm{mod}} + I_{\mathrm{mod}}^2$ behaviour. This should have been captured by the fit to Eq. (51), but as we can see in Fig. 4.12(a) fit and datapoints deviate especially for $I_{\mathrm{mod}} < -0.5\,\mathrm{mA}$ (red datapoints). One possible explanation for this deviation is the small fitting range of $|I_{\mathrm{mod}}| \leq 0.2\,\mathrm{mA}$. This had to be chosen in order to compare different structures whose critical current regimes differed significantly. We do not consider this regimes when we extract the critical current with the threshold $\Delta A_{1\omega}\,(I_{\mathrm{mod}}) > 0.05\,\mathrm{\mu V}$.

In Fig. 4.13 the extracted critical current I_{crit} is shown as a function of the magnetic field for the three-terminal structure shown in Fig. 4.12 and for three additional structures whose dimensions are summarized in Tab. 4.1. For a better signal to noise ratio we show the mean value of the extracted critical currents for positive and negative magnetic field directions. For a separate presentation for positive and negative magnetic fields, see Fig. A.3 in the Appendix. For all four structures we observe a slight increase for the critical current with increasing magnetic field magnitude. Only structure 4 deviates from this trend for $\mu_0 H = 40\,\mathrm{mT}$ and $50\,\mathrm{mT}$. As we can see from Fig. A.3 this deviation is only observed in one field direction and is due to the bad signal to noise ratio and small deviation of $\Delta A_{1\omega}\,(I_{\mathrm{mod}})$ which made it difficult to reliably extract the critical current. We can furthermore observe in Fig. 4.13 that structure 1 and 3 with a modulator of width $w_{\mathrm{m}} = 600\,\mathrm{nm}$ have larger critical currents than the structures with $w_{\mathrm{m}} = 300\,\mathrm{nm}$ and $400\,\mathrm{nm}$. This can be attributed to the smaller modulator current density $j_{\mathrm{mod}} = \frac{I_{\mathrm{mod}}}{t_{\mathrm{Pt}} w_{\mathrm{inj}}}$ [14] due to the larger modulator width w_{m} which is in the end relevant for the SHE magnon injection process. Suprisingly, we observe slightly larger critical currents for structure 4 with a modulator width $w_{\mathrm{m}} = 300\,\mathrm{nm}$ compared to structure 2 with $w_{\mathrm{m}} = 400\,\mathrm{nm}$ although the current density is larger in the former structure. One possible explanation could be the uncertenties that arise from the determination of the critical current via the threshhold $\Delta A_{1\omega}\,(I_{\mathrm{mod}}) > 0.05\,\mathrm{\mu V}$ or fluctuations in the spin current interface transparency at the modulator for the two different devices. Especially for structure 4, the linear and quadratic fit does not capture the data very well which can be seen at the superimposed quadratic dependence that still can be observed for the positive field direction in Fig. A.4.

Structure	w	w_m	d_m
1	500 nm	600 nm	200 nm
2	500 nm	400 nm	300 nm
3	500 nm	600 nm	300 nm
4	500 nm	300 nm	350 nm

Table 4.1: Details on structures in Fig. 4.13

The magnetic field-dependence of the critical current I_crit for the individual structures is in general in good agreement with the results for a $13.4\,\mathrm{nm}$ YIG film and a structure with $d_\mathrm{m} = 400\,\mathrm{nm}$ and $w_\mathrm{m} = 500\,\mathrm{nm}$ in Ref. [5]. For a magnetic field up to $\mu_0 H = 50\,\mathrm{mT}$, which corresponds to the magnetic field range captured in our experiments, they observed only a small increase in I_crit. For fields up to $\mu_0 H = 200\,\mathrm{mT}$ an overall increase of about $\Delta I_\mathrm{crit} \approx 0.3\,\mathrm{mA}$ was shown. As one focus of the measurement is the precharacterization of magnon modulation to later conducted simultaneous micro focused BLS experiments (see Section 4.3), we measured a magnetic field range up to $\mu_0 H = 55\,\mathrm{mT}$ up to which the BLS setup at the RPTU Kaiserslautern is limited.

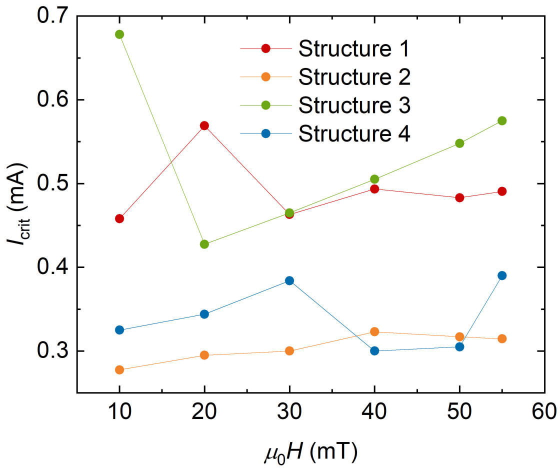

Figure 4.13: Critical current as a function of the magnetic field. The measurements are conducted at a temperature of $T = 280\,\mathrm{K}$ for different structures. For more details of the used structures see Tab. 4.1.

We can include the magnon spin conductivity enhancement into the fitting function Eq. (51) following Refs. [5, 15, 46]. It takes into account the formation of the zero effective damping state in terms of a spin chemical potential μ_s induced via the SHE in the modulator electrode. This results in a divergence of the magnon conductivity near the damping compensation regime $I_\mathrm{mod} \rightarrow I_\mathrm{crit}$ by $\sigma_\mathrm{m} \propto \left(1 - \frac{I_\mathrm{mod}}{I_\mathrm{crit}}\right)^{-1/2}$ (see Section 2.5). In the following we want to assume that the modulation of magnon conductivity is localized below the modulator. The magnon transport signal as a function of the modulator current I_mod can then be described by (See Ref. [5] for a more detailed derivation.):

$$A_{1\omega}\left(\varphi, I_{\mathrm{mod}}\right)=\cos^2\varphi\times \left\{2\left(\Delta U'\right)^{-1}+\left[\Delta U^0_{\mathrm{mod}}\left(1-\frac{I_{\mathrm{mod}}\left(-\cos\varphi\right)}{I_{\mathrm{crit}}}\right)^{-\frac{1}{2}}+\Delta R_{\mathrm{th}}I^2_{\mathrm{mod}}\right]^{-1}\right\}^{-1}. \tag{53}$$

In. Eq. (53) $\Delta U'$ corresponds to the magnon conductivity σ'_{m} to the left and right of the modulator, $\Delta U^0_{\mathrm{mod}}$ and ΔR_{th} correspond to σ^0_{m} and $\Delta\sigma_{\mathrm{th}}$ in Eq. (30). The $\cos^2\varphi$ results from the angle dependence due to the SHE-induced magnon transport from injector to detector electrode. The $\cos\varphi$ in the square root term describes the additional SHE symmetry at the modulator [5, 13, 46]. The contribution of thermally injected magnons at the modulator electrode is independent of the angle and thus the contribution $\Delta R_{\mathrm{th}}I^2_{\mathrm{mod}}$ in Eq. (53) is angle independent. With Eq. (53) we can now describe the distinct enhancement of the magnon transport signal in the critical current regime shown in Fig. 4.12(a). We use $\Delta U'$, $\Delta U^0_{\mathrm{mod}}$ and ΔR_{th} as free fitting parameters and set the angle $\varphi = 180°$ for positive magnetic fields and $\varphi = 0°, 360°$ for negative magnetic fields. We further needed to restrict the fit range to $I_{\mathrm{mod}} > I_{\mathrm{crit}}$ for negative magnetic fields and $I_{\mathrm{mod}} < I_{\mathrm{crit}}$ for positive magnetic fields because of the diverging character of Eq. (53) for $I_{\mathrm{mod}} \to I_{\mathrm{crit}}$.

In the following analysis we use two different methods for extracting the critical current I_{crit} and compare how good they agree on the measurement data, for each magnetic field separately. Fig. 4.14 (a) shows the electrical magnon transport amplitudes for the three-strip structure with modulator width $w_{\mathrm{m}} = 600\,\mathrm{nm}$ and edge-to-edge distance between the three electrodes of $d_{\mathrm{m}} = 200\,\mathrm{nm}$ (structure 1 previously shown in Fig. 4.12) as a function of the applied modulator charge current I_{mod}. The blue solid lines correspond to fits using Eq. (53) in which the critical current I_{crit} is determined due to the condition $\Delta A_{1\omega}\left(I_{\mathrm{mod}}\right) > 0.05\,\mu\mathrm{A}$ as explained above (marked by orange arrows in Fig. 4.14(a)). We see that this phenomenological model of the modulation enhancement of the magnon transport signal agrees well with the measurement data including the critical current regime up to I_{crit} for all shown magnetic field magnitudes. We can see that for the negative field direction the critical current was defined at the onset of the peak structure and the data is perfectly represented by the fit curve, including a steep increase close to I_{crit}. For the positive field case the critical current condition is fullfilled below the peak well described by the phenomenological model.

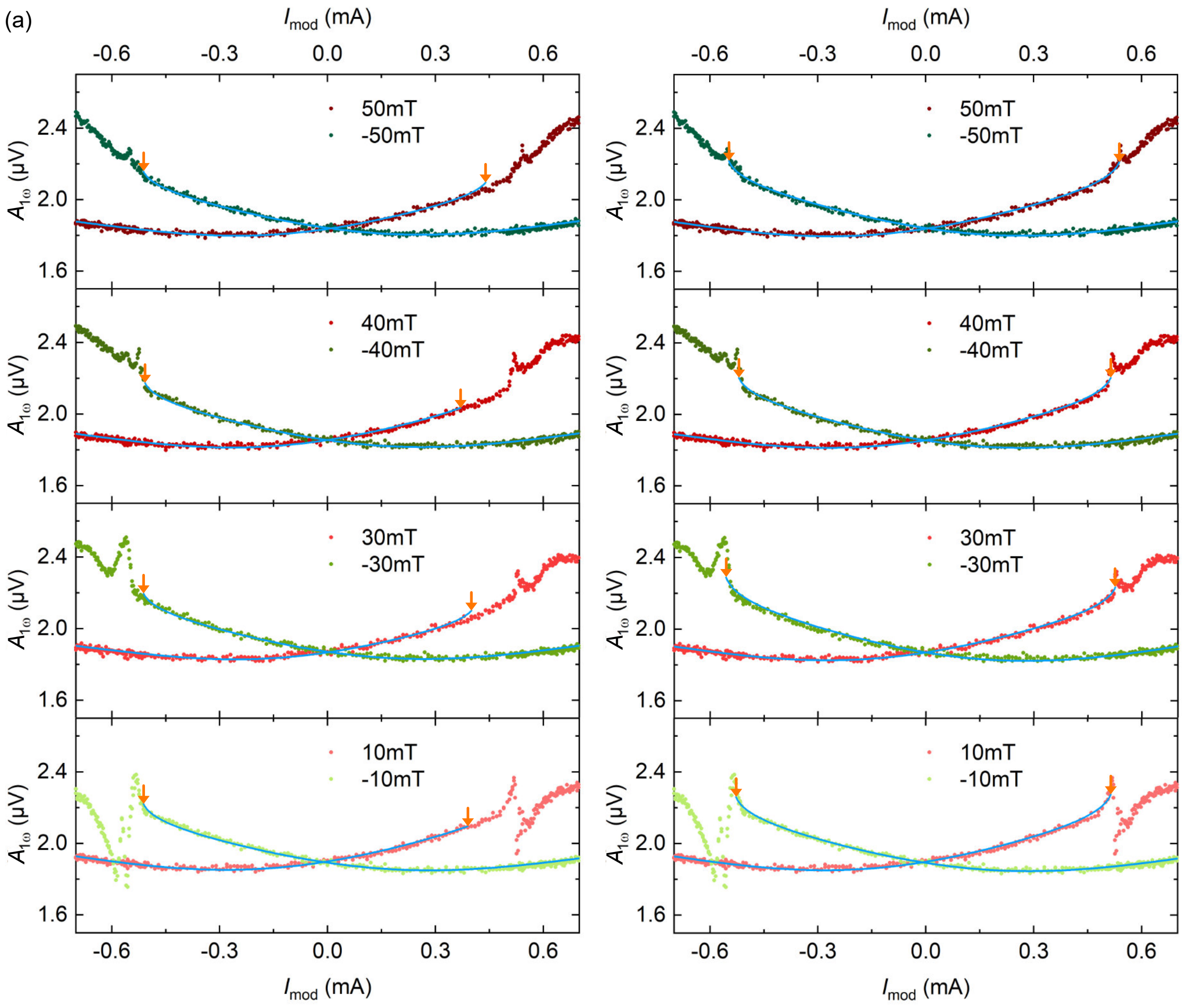

Figure 4.14: Electrical magnon transport signal as a function of the applied DC-charge current at the modulator. The measurements are conducted at a temperature of $T = 280\,\mathrm{K}$ for a structure with modulator width $w_\mathrm{m} = 600\,\mathrm{nm}$ and distance $d_\mathrm{m} = 200\,\mathrm{nm}$ between the three electrodes. The used critical currents are marked with orange arrows. (a) Magnon transport data fitted with Eq. (53) (blue solid line) with the critical currents taken from Fig. 4.13. (b) Magnon transport data fitted with Eq. (53) (blue solid line) with critical currents manually extracted from the maximum peak for $A_{1\omega}$ in Fig. 4.12(a).

Last but not least we want to compare the I_crit extracted from the condition $\Delta A_{1\omega}\,(I_\mathrm{mod}) > 0.05\,\mu\mathrm{V}$ to the critical current values manually extracted from the maximum of $A_{1\omega}$. These values are indicated by an orange arrow in Fig. 4.14(b). The blue solid lines are fits to the data using Eq. (53) and the manually extracted critical currents I'_crit again restricting the fit range as $I_\mathrm{mod} < I'_\mathrm{crit}$. We can see that the phenomenological model describes the measurement data to the steep increase of the mangon transport signal around I'_crit. Above the critical current we can not describe the modulation process via Eq. (53). This behaviour was also observed by T. Wimmer in Ref. [5]. They also extracted the values for the critical current manually from the maximum peak and did also observe a good agreement of their fit with the experimental data. We have to mention that not all of the investigated structures showed a clear peak in $A_{1\omega}$ for all magnetic fields in the critical current regime (see Appendix Fig. A.5). Thus we decided to use the condition $\Delta A_{1\omega}\,(I_\mathrm{mod}) > 0.05\,\mu\mathrm{V}$ to determine I_crit instead of manually extracting I_crit from the peak position for the sake of comparability between all measurements in this thesis.

4.2.1 Summary

In this section we discussed the modulation of the magnon conductivity via SHE induced spin currents generated by an additional DC-charge current at the modulator strip of a three-terminal magnon transport structure. We analysed the dependence on the modulator currents with respect to the low current bias regime and the critical current regime and extracted the critical current I_{crit} via the condition for $\Delta A_{1\omega}\left(I_{\mathrm{mod}}\right) > 0.5\,\mu\mathrm{V}$ and manually from the electrical magnon transport signal. Our results for the modulation behaviour and the critical currents is in good agreement with literature in Refs. [4, 5, 14, 15, 47] and we could define conditions for the critical currents which can be used in the following section. Where we nevertheless cover another method to show the modulation and determine the critical current based on BLS measurements combined with simulataneous magnon transport measurements via lock-in detection scheme on our three-strip structures.

4.3 Electrical modulation of magnon spin transport with simultaneous Brillouin Light Scattering measurements

In this section we have a look at magnon transport measurements on three-terminal structures measured simulatenously electrically via the lock-in detection scheme (see Section 3.2.2) and optically via microfocused BLS (see Section 3.3). We used structure 4 from the previous section with a modulator width $w_{\mathrm{m}} = 300\,\mathrm{nm}$, an injector and detector width of $w = 500\,\mathrm{nm}$ and an edge-to-edge distance $d_{\mathrm{m}} = 350\,\mathrm{nm}$ between the three electrodes. For simultaneous measurements we had to install the sample upside down in the BLS setup described in Section 3.3 with the magnetic field pointing in y-direction (see Fig. 3.10) and using a laser with $\lambda = 491\,\mathrm{nm}$ focused on the modulator strip with a spot diameter of $350\,\mathrm{nm}$ at the sample. The sample was additionally electrically contacted as described in Section 3.2.2, using an AC-charge current $I_{\mathrm{inj,ac}}$ with a maximum value of $100\,\mu\mathrm{A}$ to generate magnons via SHE and variable DC-modulator currents I_{mod} for modulation of the electrical magnon transport analogous to the already discussed measurements in Section 4.2. The following measurements were made during two visits at Prof. Dr. M. Weiler's group at the RPTU in Kaiserslautern. Due to the existing micro BLS setup we made our measurements at room temperature and for different magnetic fields in the range of $\mu_0 H = 10\,\mathrm{mT}$ to $55\,\mathrm{mT}$. Fig. 4.15 shows the simultaneous electrical (on the left) and optical (on the right) measurements at a magnetic field of $\mu_0 H = 40\,\mathrm{mT}$. The left side shows the electrical magnon transport measurement as a function of the applied charge current at the modulator I_{mod}. The right side shows the BLS spectrum for the applied charge currents I_{mod} as a function of the frequency. For the electrical measurement we observe the already in the previous Section 4.2 for Fig. 4.12 discussed evolution. We get an increasing magnon transport signal for negative I_{mod} and a flattening for about $I_{\mathrm{mod}} = 0.5\,\mathrm{mA}$. The optical measurements on the right show two very large peaks (red) in the middle which result from the laser and the reference signal which we don't discuss in more detail here. Apart from that we see a Stokes and Anti-Stokes peak for modulator currents $I_{\mathrm{mod}} \leq -270\,\mathrm{mA}$ that shifts towards higher (Anti-Stokes) and lower (Stokes) frequencies with increasing

I_{mod}. The orange dashed line can be used to compare the modulator current where the BSL spectrum starts to increase and the electrical current at the detector electrode. For the electrical magnon transport signal we can also observe a small plateau for the same I_{mod}. But compared to our previous measurements discussed in Section 4.2 the evolution shows no clear peak indicating the critical current regime (see Fig. A.7 in the Appendix). For a more detailed analysis of the evolution of the electrical magnon transport signal it would have been necessary to measure with smaller steps for I_{mod}. This would have taken a lot more time due to the simulataneous BLS measurements where we ned to focus the laser and average the frequency spectrum several times for each I_{mod}. Conducting such time consuming measurements was not possible due to the limited time we had for our measurementre at the Micro-BLS setup in Kaiserslautern. The observed maxima in the BLS spectrum correspond to the increase in magnonpopulation we expect due to the zero effective damping state beneath the modulator strip. To check if the observed increase in magnon population is indeed originating from the pure spin current injection via the SHE at the modulator strip, we conducted the same measurements also for $\mu_0 H = -40\,\mathrm{mT}$. Here, we observe the maximums in counts in the BLS spectrum for positive modulator currents instead of the negative I_{mod} for positive magnetic field (see Fig. A.6 in the Appendix). Thus, we find a dependence on current polarity which means the peaks in the BLS spectra result from SHE injected magnons at the modulator strip and not due to some Joule heating effects. In general the BLS spectrum is proportional to the magnon density [17, 18]. Which is in agreement with our considerations on the magnon density beneath the modulator electrode for $I_{\mathrm{mod}} \to I_{\mathrm{crit}}$ in the previous Section 4.2 and Refs. [4, 5, 15]. For a more detailed analysis of the measurements we have a look at a the BLS spectrum at a fixed $I_{\mathrm{mod}} = -450\,\mu\mathrm{A}$ indicated by the green dashed line in Fig. 4.15.

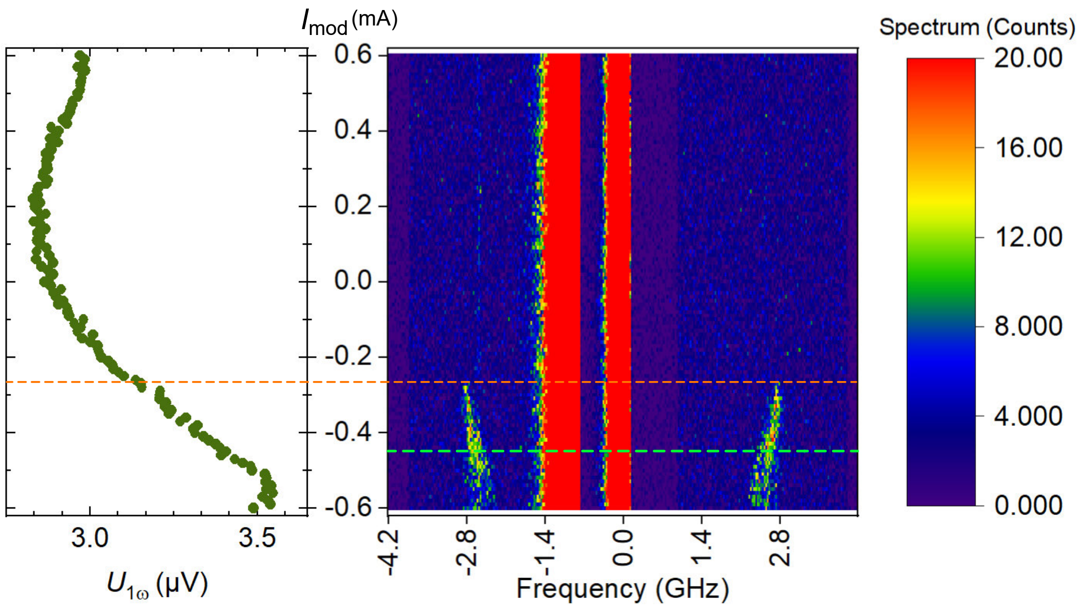

Figure 4.15: Applied charge current at the modulator as a function of the electrical magnon transport signal on the left and the BLS spectrum for different applied charge currents I_{mod} as a function of the frequency on the right. The measurement is conducted at room temperature at a magnetic field of $\mu_0 H = 40\,\mathrm{mT}$ for a modulator width of $w_{\mathrm{m}} = 300\,\mathrm{nm}$ with distance $d_{\mathrm{m}} = 350\,\mathrm{nm}$ to injector and detector.

Fig. 4.16 shows the BLS spectrum we extracted from the spectrum in Fig. 4.15 at $I_{\mathrm{mod}} = -450\,\mu\mathrm{A}$ as a funtion of the frequency. The two large peaks exceeding the plot range between -2 and $0.5\,\mathrm{GHz}$ originate from the reference beam in the TFPI and is not discussed further. We observe two quite symmetric peaks for positive (at around $2.5\,\mathrm{GHz}$) and negative (at around $-2.8\,\mathrm{GHz}$) frequencies that can be assigned to Stokes (positive) and Anti-Stokes (negative) inelastic light scattering processes with the magnons in the YIG layer. For further analysis of the data we can fit the two magnon peaks with:

$$L\,(f) = \frac{A}{(f^2 - f_{\mathrm{r}}^2) + l^2 \cdot f_{\mathrm{r}}^2} + o, \tag{54}$$

with A the amplitude, f_{r} the resonance frequency, l the linewidth and o a finite offset. We can extract this fit parameters for all measured BLS spectra at magnetic fields in the range of $\mu_0 H = 10\,\mathrm{mT}$ to $55\,\mathrm{mT}$ and for modulator currents starting at the optical critical current $I_{\mathrm{crit,op}}$ where the formation of the magnon peak is observed [17]. In the following we analyze the extracted parameters.

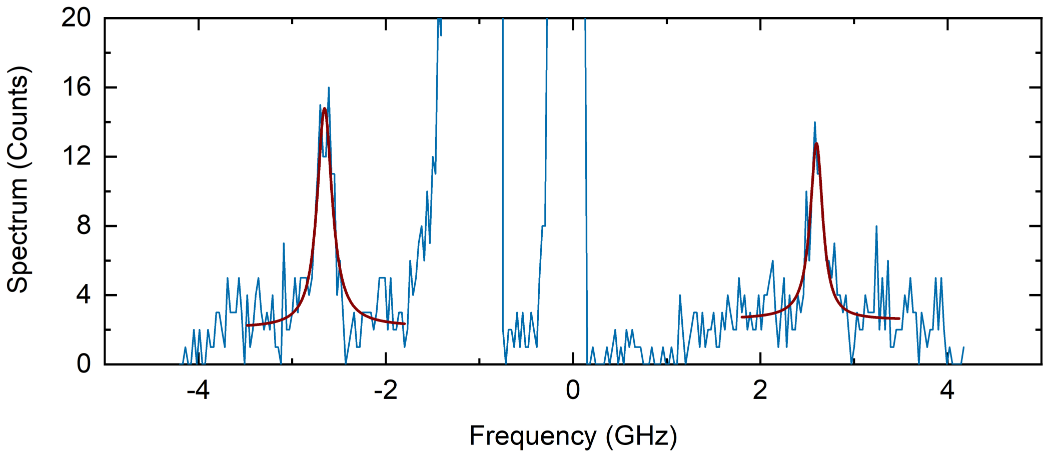

Figure 4.16: BLS spectrum as a function of the frequency. The measurement is conducted for $I_{\mathrm{mod}} = -450\,\mu\mathrm{A}$ at room temperature at a magnetic field of $\mu_0 H = 40\,\mathrm{mT}$ for a modulator width of $w_{\mathrm{m}} = 300\,\mathrm{nm}$ in a distance $d_{\mathrm{m}} = 350\,\mathrm{nm}$ to injector and detector. Fits with Eq. (54) are shown for positive and negative resonance frequency (red solid lines).

Fig. 4.17 therefore shows the extracted positive and negative resonance frequency f_{r} as a function of the modulator current. For positive magnetic fields we fit the BLS spectra via Eq. (54) for negative modulator currents starting at $I_{\mathrm{crit,op}}$. Due to the Spin Hall symmetry we only observe magnon peaks for $I_{\mathrm{mod}} < 0\,\mu\mathrm{A}$ for positive magnetic fields. For negative resonance frequencies (brown) corresponding to Anti-Stokes process we observe for all shown magnetic fields an increase in absolute frequency for increasing I_{mod} up to about $I_{\mathrm{mod,max}} \approx -0.55\,\mathrm{mA}$ and after this a nearly constant frequency with a slight decrease in absolute frequency. For a magnetic field of $\mu_0 H = 20\,\mathrm{mT}$ the magnon peak was visible for lower absolute modulator current values and could therefore also be fitted with Eq. (54) until $I_{\mathrm{mod}} = -210\,\mu\mathrm{A}$. In addition we find that the frequencies shifting with the applied magnetic fields. Starting from around $f_{\mathrm{r}} \approx -3\,\mathrm{GHz}$ at a magnetic field of $\mu_0 H = 50\,\mathrm{mT}$ towards $f_{\mathrm{r}} \approx -1.6\,\mathrm{GHz}$ at a magnetic field of $\mu_0 H = 20\,\mathrm{mT}$. For positive frequencies (turquoise) corresponding to Stokes process we observe the symmetric case: a decreasing resonance frequency with increasing modulator current until $I_{\mathrm{mod,max}}$ and from that a nearly constant frequency value. The observed symmetry of the resonance frequencies is due to the origin of the peaks in the BLS spectra that result from creation and annihilation processes of magnons with the same properties. The shift in frequency with I_{mod} could also be observed in Refs. [17, 18]. In Ref. [17], the BLS measurements were conducted on a $20\,\mathrm{nm}$ thick Bi-doped YIG film ($Bi_1Y_2Fe_5O_{12}$) using a single $1\,\mu\mathrm{m}$ wide Pt-strip with an applied DC-current to inject magnons via SHE which can be compared to our modulator electrode. In Ref. [18] a $500\,\mathrm{nm}$ wide Pt-strip and an additional Au-antenna to apply pulsed DC-currents for spin injection via SHE, which makes it possible to have time-resolved measurements. This shift in the resonance frequency towards smaller $|f_{\mathrm{r}}|$ for increasing $|I_{\mathrm{mod}}|$ is due to Joule heating processes at the Pt modulator and possibly magnon scattering processes associated with the SHE injected magnons. The Joule heating induced shift in resonance frequency is caused by the reduction of the saturation magnetization M_{s} with increasing temperature, which causes a reduction of magnon frequencies at fixed magnetic field following from the $k = 0$ Kittel formula:

$$\omega_{k=0} = \gamma\mu_0\sqrt{H\left(H + M_{\mathrm{s}}\right)}, \tag{55}$$

where γ is the gyromagnetic ratio [17]. Furthermore the increasing resonance frequency with increasing magnetic field is in good agreement with Ref. [17] and expected from the Kittel equation (Eq. (55)).

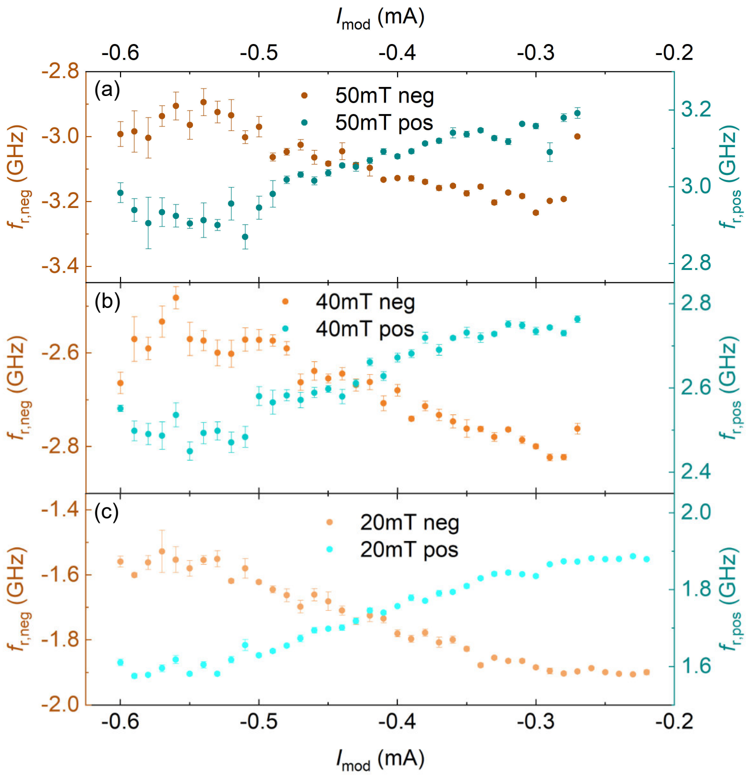

Figure 4.17: Negative (left side) and positive (right side) resonance frequency f_r as a function of the applied charge current I_{mod} at the modulator electrode. The measurements are conducted at room temperature for a modulator width of $w_m = 300\,\mathrm{nm}$ with a distance $d_m = 350\,\mathrm{nm}$ to injector and detector at a magnetic field of (a) $\mu_0 H = 50\,\mathrm{mT}$, (b) $\mu_0 H = 40\,\mathrm{mT}$ and (c) $\mu_0 H = 20\,\mathrm{mT}$.

In the following we want to compare the electrical and optical measurements directly. Fig. 4.18 shows therefore the difference $\Delta A_{1\omega}$ between the magnon transport signal and the linear and quadratic fit of the low current bias regime ($|I_{mod}| \leq 0.2\,\mathrm{mA}$) with Eq. (51) (green) and the sum of the BLS spectra counts integrated over $2\,\mathrm{GHz}$ to $3\,\mathrm{GHz}$ (blue) as a function of the applied charge current at the modulator for different magnetic fields. The evolution of $\Delta A_{1\omega}$ is very similar to the results in Section 4.2: For the low current bias regime $|I_{mod}| \leq 0.2\,\mathrm{mA}$ the linear and quadratic function is in good agreement with the data and therefore $\Delta A_{1\omega}$ shows no significant deviation from zero, towards the critical current regime, we observe a small increase followed by a decrease leading to a deviation of about $0.2\,\mu\mathrm{V}$. For the optical signal we summed up the BLS counts of the magnon peak for a range of $\Delta f = 1\,\mathrm{GHz}$ for each I_{mod} and took the average for positive and negative frequencies. Coming from positive modulator currents the evolution of the BLS spectrum starts for all magnetic fields at about 80 Counts, which can be defined as the background and increases with larger negative values of I_{mod}. As already shown in Section 4.2 we can extract the critical current from $\Delta A_{1\omega}$ by using the condition $\Delta A_{1\omega} > 0.05\,\mu\mathrm{V}$. This determined value for I_{crit} is indicated with orange arrows on the left. For the optical critical current we define the condition as summed counts $\Sigma_{BLS} > 100\,\mathrm{Counts}$, which corresponds to a critical current where the formation of the magnon peaks can be observed [17]. The critical currents due to that condition are shown with the orange arrows on the right. By comparing the electrical signal $\Delta A_{1\omega}$ with our previous measurements in Section 4.2, we first of all need to keep in mind, that the orientation of the magnetic field ist rotated by $180°$ because in the BLS setup the magnetic field direction is defined in the opposite way and we therefore extract negative critical currents for positive magnetic fields. The critical current marks the beginning of the zero effective damping state (see Section 2.5), where we expect the magnon lifetime to diverge resulting in an magnon accumulation and an effectivly vanishing magnon decay beneath the modulator (see Fig. 2.6). Thus, the critical current extracted from the BLS spectra corresponding to a magnon accumulation beneath the modulator should be identical to the I_{crit} determined from the electrical magnon transport experiments. For modulator currents $|I_{\mathrm{mod}}|$ above I_{crit}, the integrated counts in the BLS spectrum as well as the deviation $\Delta A_{1\omega}$ is further increasing. For a magnetic field of $\mu_0 H = 30\,\mathrm{mT}$ the spectrum also seems to decrease again for $I_{\mathrm{mod}} < -580\,\mu\mathrm{A}$. As we expect the optical and electrical critical currents to be identical, as both indicate the zero effective magnon damping state we quantitatively compare I_{crit} in the following.

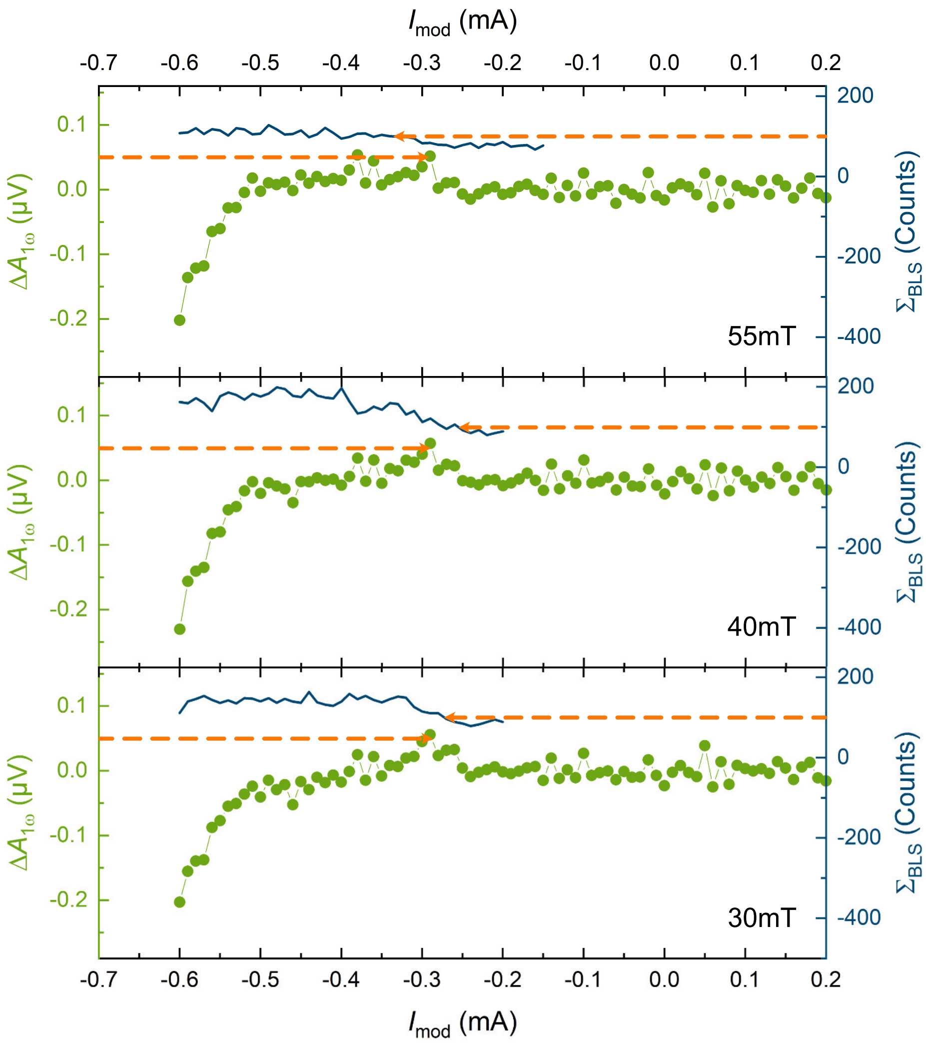

Figure 4.18: Difference between the electrical magnon transport signal and the quadratic and linear fit with Eq. (51) for a modulator current of $I_{\mathrm{mod}} = -200\,\mu\mathrm{A}$ to $I_{\mathrm{mod}} = 200\,\mu\mathrm{A}$ (green) and the integrated intensity sum of the BLS spectrum (blue solid line) as a function of the applied charge current at the modulator electrode. The measurements are conducted at room temperature, for a modulator width of $w_{\mathrm{m}} = 300\,\mathrm{nm}$ with distance $d_{\mathrm{m}} = 350\,\mathrm{nm}$ to injector and detector electrode for different magnetic fields.

Fig. 4.19 shows the extracted critical currents for the electrical magnon transport measurements and the BLS measurements as a function of the magnetic field. The critical currents extracted from the electrical signal show for $\mu_0 H = 10\,\mathrm{mT}$ and $20\,\mathrm{mT}$ the highest $I_{\mathrm{crit,el}}$ and smaller critical currents with no significant change for larger magnetic fields. The optical critical currents show a slight increase of $I_{\mathrm{crit,op}}$ with increasing magnetic fields but are in general slightly lower than $I_{\mathrm{crit,el}}$. For magnetic fields of $\mu_0 H \geq 30\,\mathrm{mT}$ the critical currents for both measurement techniques are in quite good agreement. The magnitude for $I_{\mathrm{crit,op}}$ and $I_{\mathrm{crit,op}}$ of $I_{\mathrm{crit}} \approx 0.3\,\mathrm{mA}$ is also in good agreement with our precharacterization measurements conducted in a superconducting magnet cryostat (see structure 4 in Fig. 4.13). The shift of the critical current and therefore the current at which we are able to observe a magnon peak in the BLS spectrum with the magnetic field is not changing significantly over the investigated magnetic field range. In contrast, the electrical critical current seems to have at least two outliers at $\mu_0 H = 10\,\mathrm{mT}$ and $20\,\mathrm{mT}$. Indeed, we find in the raw data for these two magnetic fields that the magnon transport signal $U_{1\omega}$ does not show a clear peak which would make it easy to define a critical current. Instead we rely on the criterion $\Delta A_{1\omega} > 0.05\,\mu\mathrm{V}$, which is prone to noise in the measurements. This might explain the large increase for I_{crit} at these low magnetic fields. Thus we conclude that extracting the critical current from the BLS spectra is more accurate.

To confirm that our model of the zero effective damping state and thereby induced magnon accumulation is correct we use Eq. (16) for the magnetic field-dependence of I_{crit} derived in Ref. [4]. We can utilize the Gilbert damping parameter and inhomogenous linewidth extracted from independent FMR measurements, the geometry of our structure and the values for the spin Hall angle, spin decay length in Pt and spin mixing conductance of YIG/Pt used in Ref. [4] to calculate the magnetic field-dependence of I_{crit}. The corresping result is plotted in Fig. 4.19 as a orange line. Given the very crude approximation of several values we find very good agreement between I_{crit} determined from optical BLS and electrical magnon transport measurements and the theoretical prediction. This is another confirmation that the observed enhancement in magnon transport signal is indeed connected to a zero effective damping state.

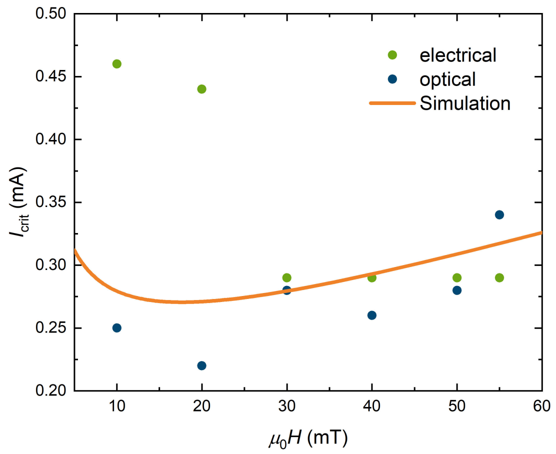

Figure 4.19: Critical modulator current for electrical and optical measurements and simulation of the critical current with Eq. (16) as a function of the magnetic field. The measurements are conducted at room temperature for a modulator width of $w_\mathrm{m} = 300\,\mathrm{nm}$ with distance $d_\mathrm{m} = 350\,\mathrm{nm}$ to injector and detector.

We can compare our critical currents extracted from the BLS measurement with the critical currents in Ref. [17]. They observed a linear dependence on the magnetic fields which seems to be in good agreement with our experimental results. For our analysed magnetic field range they extracted for their $20\,\mathrm{nm}$ thick Bi-doped YIG film a critical current of $I_\mathrm{crit} \approx 0.5\,\mathrm{mA}$ to $0.9\,\mathrm{mA}$ which corresponds to current densities of $\boldsymbol{j}_\mathrm{crit} = 8.33 \cdot 10^{10}\mathrm{A/m^2}$ and $1.50 \cdot 10^{11}\mathrm{A/m^2}$ at a strip width of $w = 1\,\mathrm{\mu m}$ and a thickness of the Pt $t_\mathrm{Pt} = 6\,\mathrm{nm}$. The current density for our optical critical currents $I_\mathrm{crit} \approx 0.25\,\mathrm{mA}$ to $0.34\,\mathrm{mA}$ are in the same range: $\boldsymbol{j}_\mathrm{crit} = 1.19 \cdot 10^{11}\mathrm{A/m^2}$ and $1.62 \cdot 10^{11}\mathrm{A/m^2}$. The increase of I_crit with increasing magnetic field is also observed in Ref. [18]. Our simultaneous measurements further confirm the assumed model of a zero effective magnon damping state, which leads to a vanishing magnon decay time. In our BLS experiments we find a significant magnon accumulation at I_crit, which corroborates the magnon damping compensation picture. Interestingly, our BLS spectra show that with increasing modulator current the magnon peak broadens significantly, which indicates that magnon scattering still plays an important role. In Ref. [17] a very sharp magnon peak was observed over a wide range of charge current values, which then is taken as an indication for the formation of a magnon Bose-Einstein condensate. Here, our results from simultaneous magnon transport and BLS measurments suggest that we can not use the enhancement in the magnon spin transport signal as an indicator for the formation of such a condensate state for magnons. It is important to mention that the Bi-doped YIG investigated in Ref. [17] exhibits a vanishing effective magnetization, i.e. the strain induced out-of-plane uniaxial magnetic anisotropy compensates the thin film shape anisotropy of the magnetic insulator. In our LPE-YIG sample this is not the case: From FMR measurements we obtain a finite value for the effective magnetization. Thus, the precession for in-plane magnetization is elliptical in our sample, while for the Bi-doped YIG film in Ref. [17] it should be nearly perfectly circular. The finite ellipticity of the magnetization precession gives rise to non-linear magnon damping effects, which should also influence our modulation experiments. Thus, further experiments with simultaneous magnon transport and BLS measurements on samples with varying effective magnetization are needed to check if there are also characteristics in the magnon transport signal, which allow to identify the contribution from a sharp magnon accumulation. The critical current seems to fit the optical experiments in this section and related measurements in literature (see Ref. [17–19]).

4.3.1 Influence of BLS measurement and high modulator currents on electrical magnon transport

In this section we compare the magnon transport measurements conducted before our measurements at the BLS setup in Kaiserslautern and afterwards and discuss the impact of laser illumination and high modulator currents. Fig. 4.20 shows the electrical magnon transport signal for different magnetic fields measured before (dark green) and after (light green) the BLS measurements as a function of the modulator current conducted at our cryostat setup. All measurements were recorded at a temperature of $T = 280\,\mathrm{K}$ for a structure with modulator width $w_\mathrm{m} = 300\,\mathrm{nm}$ and edge-to-edge distance between injector and detector of $d = 1\,\mathrm{\mu m}$ (structure 4 in Section 4.2). The solid lines are fits to the $I_\mathrm{mod} + I_\mathrm{mod}^2$ dependence in Eq. (51) within the fit range of the low current bias regime $|I_\mathrm{mod}| \leq 0.2\,\mathrm{mA}$ (grey shaded area) and extrapolated over the shown modulator current range. The extracted fit parameters are shown in the Appendix in Tab. A.4. The magnon transport signal before the BLS measurement shows the characteristic modulator current-dependence and critical current peak described in Section 4.2. After the BLS measurements no clear peak can be identified. Furthermore we observe an increased $A_{1\omega 0}$, given by the offset of the measurement data at $I_\mathrm{mod} = 0\,\mathrm{\mu A}$. This corresponds to an increased magnon transport amplitude without modulation for all shown magnetic field magnitudes. The largest difference in $\Delta A_{1\omega 0} \approx 0.2\,\mathrm{\mu V}$ compared to the measurements before BLS can be observed for $\mu_0 H = 10\,\mathrm{mT}$ (see Tab. A.4). Furthermore for $\mu_0 H = 40\,\mathrm{mT}$ and $50\,\mathrm{mT}$ we can clearly see that the modulation efficiency in the linear regime is reduced, as the light green datapoints show smaller increase as a function of the applied modulator current. This is in good agreement with the extracted fitparameters for the SHE modulation ΔR_SHE and the thermal modulation R_th that are larger for before the BLS measurements (see Tab. A.4). The same applies for the critical current regime. Here the nonlinear increase in $A_{1\omega}$ due to the damping compensation state is only visible in the data before the BLS measurements. Only for $\mu_0 H = 10\,\mathrm{mT}$ a small deviation from the linear and quadratic evolution can be observed.

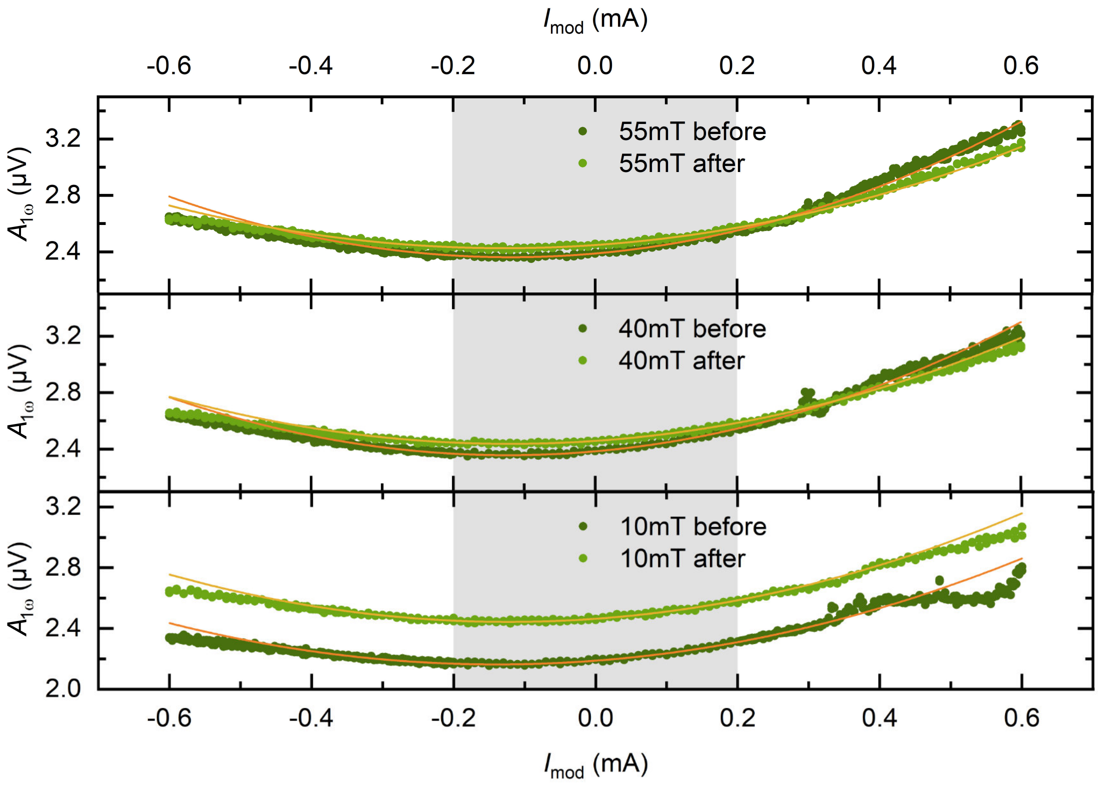

Figure 4.20: Electrical magnon transport signal before laser illumination (dark green) and after (light green) as a function of the applied charge current at the modulator electrode. The measurements are conducted at a temperature of $T = 280\,\mathrm{K}$ for a modulator $w_\mathrm{m} = 300\,\mathrm{nm}$ with a distance $d_\mathrm{m} = 350\,\mathrm{nm}$ to injector and detector at different magnetic fields. The solid lines are fits to the data using Eq. (51). The corresponding fit parameter are shown in Tab. A.4.

We attribute the observed change of the magnon transport signal to changes in the YIG/Pt interface and in the YIG itself underneath the modulator strip induced by heating effects due to the applied large modulator currents and the intense laser illumination. To confirm this conjecture, we have a look at the powerdensity caused by the laser exposure and I_mod. Due the large current densities of up to $2.86 \cdot 10^{11}\mathrm{A/m^2}$ in the used modulator strip with $w_\mathrm{m} = 300\,\mathrm{nm}$, and a length of $l_\mathrm{mod} = 120\,\mathrm{\mu m}$ and thus a power density of $P = \frac{U \cdot I}{w_\mathrm{m} \cdot l_\mathrm{mod}} = 5 \cdot 10^8 \mathrm{W/m^2}$ (corresponding to $I_\mathrm{mod} \approx 600\,\mathrm{\mu A}$) the temperature increase in the modulator strip and at the YIG/Pt interface due to its finite resistance is significant. Thermometry measurements of a modulator of width $w_\mathrm{m} = 150\,\mathrm{nm}$ indicate an increase in temperature of the modulator electrode reaching $T = 550\,\mathrm{K}$ for a modulator current of $I_\mathrm{mod} = 830\,\mathrm{\mu A}$ [14]. The laser on the other hand operates at a laser power of $P_\mathrm{laser} = 3\,\mathrm{mW}$ measured above the sample and assume a laserspot radius of $175\,\mathrm{nm}$ and therefore a spotsize area of $A_\mathrm{laser} = 9.62 \cdot 10^{-14}\mathrm{m^2}$ which results in a power density of $3.12 \cdot 10^{10}\mathrm{W/m^2}$. This value is of course the upper limit and assumes that the laser power is fully absorbed by the sample. More likely, only a few percent of the estimated power density is absorbed by the sample. Both extracted power densities are significant and lead to a considerable temperature increase. Thus, we conclude that heating induced changes to our structures are possible. As the measurements can last up to a few hours this corresponds to high temperature annealing below the modulator induced by the high current and the laser exposure that can significantly influence the modulation properties. In contrast to the high current annealing that takes place over the whole Pt-electrode, the exposed area of the laser is small and we expect a localized temperature increase and thus only a local effect due to the laser annealing. As both annealing techniques lead to similar results it is not possible to disentangle the two effects in the measurement scheme used in Section 4.3. To seperate the two contributions one could think of magnon transport measurements before and after the laser exposure without a simultaneously applied current. To better illustrate this effect, we have a closer look on the impact of the modulator current and especially high modulator currents in the following.

In SMR experiments it was shown that the temperature annealing caused by large modulator current exposure reduces the spin mixing conductance $g^{\uparrow\downarrow}$ and thus the interface transparecy for magnon injection at the modulator electrode. Within this line of argument we can attribute the increased magnon transport signal at vanishing modulator current $A_{1\omega 0}$ observed in Fig. 4.20 to a less transparent interface of the modulator electrode, which has a decreased ability to absorb magnons that are transported from injector to detector [14]. The decreased modulation efficiency in the linear regime for the SHE and thermal modulation contribution is also in accordance with a decreased spin mixing conductance of the interface since both contributions rely on $g^{\uparrow\downarrow}$ [14]. Furthermore it was shown in Ref. [14] that the electrical resistivity of the modulator strips decreased with increasing $\boldsymbol{j}_{\mathrm{mod,max}}$ by a few $10\,\%$ which results in a decreased dissipated power and thus less Joule heating at the electrode. As this change in resistivity was observed to be small we assume that the dominant contribution to the change in thermal modulation efficiency can be attributed to a decreased spin mixing conductance $g^{\uparrow\downarrow}$.

In the critical current regime in Fig. 4.20 for $\mu_0 H = 10\,\mathrm{mT}$ we observe that a larger critical current I_{crit} has to be applied to reach the damping compenstation state due to the reduced interface transparency for the SHE induced magnons. This larger critical current is accompanied by a larger contribution to Joule heating. This is in good agreement with the observations reported in Ref. [14]. They observed a monotonous increase in I_{crit} for successive applied larger maximal modulation currents $I_{\mathrm{mod,max}}$. Additionally we observe a supression of the magnon modulation in the critical current regime with increasing magnetic field magnitude. This is in good agreement to the measurements in Ref. [14] where a strong supression of the magnon modulation was observed in the non-linear current regime with increasing magnetic field at a maximum modulator current of $I_{\mathrm{mod,max}} = 830\,\mu\mathrm{A}$. In contrast to our measurements, in Ref. [14] the non-linear behaviour was observed for all measured magnetic fields.

Last but not least we want to discuss the influence of even higher modulator currents up to $I_{\mathrm{mod}} = 900\,\mu\mathrm{A}$ on the magnon transport signal. To this end, we use structure 4 from Section 4.2 with a modulator width of $w_{\mathrm{m}} = 300\,\mathrm{nm}$ and an edge-to-edge distance of $d_{\mathrm{m}} = 350\,\mathrm{nm}$ between the three electrodes. The measurements were conducted at a temperature of $T = 280\,\mathrm{K}$ and a magnetic field of $\mu_0 H = 55\,\mathrm{mT}$. The measurements were conducted after the BLS measurements and thus without any laser exposure in between so the evolution between the two (red and green) magnon transport signal can be attributed to the high modulator currents only. Once again the modulator current is set to the maximal positive value and is sweeped to the maximal negative value. The maximal modulator current was first measured up to $I_{\mathrm{mod,max}} = 650\,\mu\mathrm{A}$ and afterwards slowly increased up to $I_{\mathrm{mod,max}} = 900\,\mu\mathrm{A}$. The corresponding current sweeps are shown in Fig. 4.21. As a reference we add the magnon transport signal before the BLS measurement (blue datapoints). The electrical magnon transport signal as a function of the modulator current can be described by three different regimes [14]. In Section 4.2 we already covered the first two regimes: The low current bias regime (grey shaded area), which we defined as $|I_{\mathrm{mod}}| \leq 0.2\,\mathrm{mA}$, where the linear and quadratic dependence on I_{mod} can be described via Eq. (51). The critical current regime, which can be describes via Eq. (53), where the magnon transport is dominated by a nonlinear magnetization dynamics (blue shaded area) [14]. The third regime, which we especially want to have a look at in the following is the overcritical current regime (green). The current-dependence for $I_{\mathrm{mod,max}} = 650\,\mu\mathrm{A}$ and $I_{\mathrm{mod,max}} = 900\,\mu\mathrm{A}$ in the low and critical current regime are in good agreement with the measurements after large modulator currents and laser exposure in Fig. 4.20 with a maximum modulator current of $I_{\mathrm{mod,max}} = 600\,\mu\mathrm{A}$. The only difference is that now the magnon transport signal $A_{1\omega}$ at $I_{\mathrm{mod}} = 0\,\mu\mathrm{A}$ is decreased compared to the measurements before the electrical and laser annealing. This behaviour we would not expect if only a deteasing interface transparency at the YIG/Pt interface occurs. One explanation could be that beneath the modulator also the YIG is affected by the annealing at a certain point. This can result in a local increased Gilbert damping α_{G} below the modulator which could explain a decreased magnon transport signal from injector to detector at $I_{\mathrm{mod}} = 0\,\mu\mathrm{A}$ compared to the case before electrical annealing.

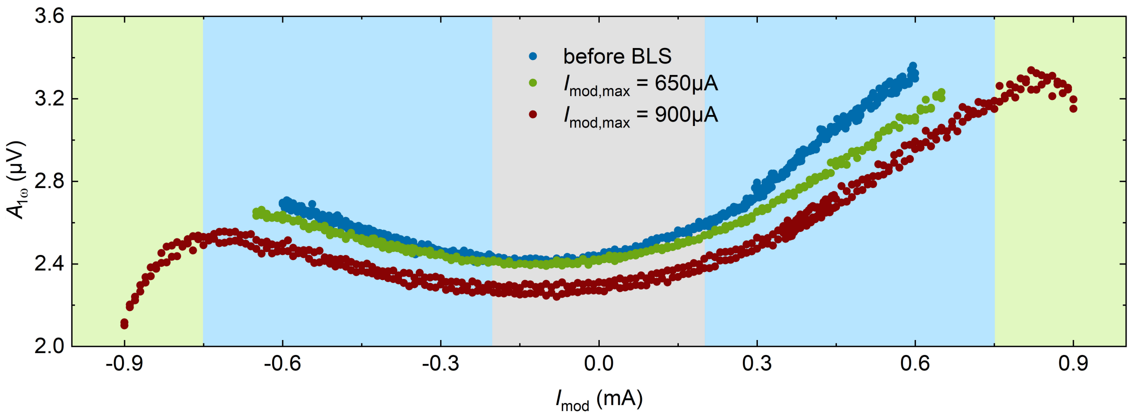

Figure 4.21: Electrical magnon transport signal as a function of the applied charge current at the modulator electrode. The measurements are conducted at a temperature of $T = 280\,\mathrm{K}$ for a modulator width of $w_{\mathrm{m}} = 300\,\mathrm{nm}$ and a distance $d_{\mathrm{m}} = 350\,\mathrm{nm}$ to injector and detector at different magnetic fields. The applied charge current is raised up to $I_{\mathrm{mod,max}} = 900\,\mu\mathrm{A}$ (red) and $I_{\mathrm{mod.max}} = 650\,\mu\mathrm{A}$ (green). The magnon transport signal is divided in three current regimes: Low current regime (grey-shaded), Critical current regime (blue-shaded), overcritical regime (green-shaded).

Such a decrease of $A_{1\omega 0}$ (see therefore the fit to the low current bias regime with Eq. (51)) was also observed for some of the measured structures on a $t_{\mathrm{YIG}} = 13\,\mathrm{nm}$ thick YIG-film in Ref. [14]. They showed that for larger $I_{\mathrm{mod,max}}$ the currents where the zero effective damping state is reached increase and even observed a double-peak structure which indicates also two critical currents and conductivity peaks [14]. We can explain the fact that we couldn't reproduce this by keeping in mind that we were only able to measure up to high modulator currents for this one structure and could also not observe a critical current peak after the BLS measurements for lower $I_{\mathrm{mod,max}}$. So for further measurements it would be necessary to use a structure with an observable peak structure and then check the magnon transport signal for larger modulator currents, which could not be covered as part of this thesis. When entering the overcritical current regime in Fig. 4.21 the magnon transport signal is rapidly decreasing above $|I_{\mathrm{mod}}| \approx 800\,\mu\mathrm{A}$. This decrease is symmetric for positive and negative values of I_{mod} and thus indicates a thermal origin of the observed behaviour [14]. This strong decrease of the magnon transport signal is in good agreement with the observations in Ref. [14]. Here a similar symmetric drop of the magnon transport signal was observed above $|I_{\mathrm{mod}}| \approx 700\,\mu\mathrm{A}$ for a modulator with $w_{\mathrm{m}} = 150\,\mathrm{nm}$. For larger modulator currents the magnon transport signal $A_{1\omega}$ vanishes for positive and negative current polarities. They performed thermometry measurements and showed that the Joule heating induced temperature increase of the modulator electrode follows a I_{mod}^4 dependence in the overcritical modulator current regime and reaches the Curie temperature of YIG $T_{\mathrm{C}} = 560\,\mathrm{K}$ [14]. This results in a magnetic phase transition to the paramagnetic state of YIG below the modulator. Thus the electrical magnon transport is blocked beneath the modulator strip and therefore can not be detected at the detector, resulting in a vanishing magnon transport signal. For this reason we attribute the drop in the magnon transport signal in Fig. 4.21 to a local phase transition of the YIG to the paramagnetic state below the modulator. For even higher modulation currents we would therefore expect the magnon transport signal to vanish.

4.3.2 Summary

In this section we realized simultaneous electrical magnon transport measurements and microfocused BLS measurements for modulation experiments on a three-strip structure. Above a critical current we observed a magnon peak in the BLS spectrum that corresponds to the zero effective damping state. For the critical current where the magnon density and with that the BLS intensity increases we also observe a small plateau in the simultaneously measured magnon transport signal. From a fit to the observed magnon peak in the BLS spectrum we extracted the magnon frequency and investigate it as a function of the applied modulator current. We observe a Joule heating induced shift in frequency towards smaller $|f_{\mathrm{r}}|$ for increasing $|I_{\mathrm{mod}}|$ and also an increasing frequency with increasing magnetic field. We further analysed the electrical and optical critical current extracted due to the threshold condition analogously to Section 4.2 for the electrical magnon transport signal and due to the increase in the summed counts of the BLS spectrum for the optical measurements. As expected from the comparison of the raw magnon transport data and the BLS spectrum both extracted critical currents are in quite good agreements with each other. By adding a fit function that theoretically describes the magnetic field-dependence of the zero effective damping state, we see that the critical current extracted from the BLS spectra fits better to the theory and is therefore more suitable to define the critical current for the zero effective damping state. At last, we analysed the thermal effects due to laser illumination and high applied modulator currents on the modulation efficieny and magnon transport signal which is both decreased. Further we observe a vanishing magnon transport signal for high modulator currents above the critical current, where we reach the Curie temperature of YIG and the magnetic phase transition prevents magnon transport.

5 Summary

In this thesis we investigated magnon transport measurements in two- and three-terminal structures on a $22\,\mathrm{nm}$ LPE-YIG thin film. We used the measurements on two-terminal structures for characterization because this was the first time we conducted all-electrical magnon transport measurements on a thin-film from Innovent with $t_{\mathrm{YIG}} = 22\,\mathrm{nm}$. Further we wanted to compare the results to previous measurements on YIG thin films to evaluate the performance of our YIG-sample. The three-terminal structures were used for modulation of all-electrical magnon transport. We investigated the modulation and the critical currents for the zero effective damping state with respect to the previous measurements [4]. And a second major goal of the measurements on three-terminal structures was the realization of simultaneous measurements of all-electrical magnon transport and BLS measurements.

In Section 4.1 we started the characterization of our $22\,\mathrm{nm}$ LPE-YIG film with electrical magnon transport measurements on two-strip structures. We observed the expected $\cos^2\varphi$ and $\cos\varphi$ dependence for the electrical and thermal magnon transport signal for all conducted edge-to-edge distances between the injector and detector electrode. For the distances d we observed increasing magnon transport signals with decreasing d. The distance-dependence of the thermal magnon transport signal showed two distance regimes and therefore two different thermal magnon decaylengths due to a combination of the temperature profile in the YIG layer and magnon spin transport, that is also known from literature. This was observed for all magnetic fields and temperatures. Also the effective spin resistivity, we exemplarily calculated, fits very well into the expected value from literature. For different magnetic fields we further can summarize the increasing magnon transport signal for increasing magnetic fields and smaller magnon decay lengths at large magnetic fields. We observe decreasing magnon transport signals for decreasing temperatures until at low temperatures where the magnon transport signal vanishes due to a decreasing thermal magnon population beneath the injector. After all, the main outcome of our magnon transport measurements on these two-strip structures is that our results for the distance-, magnetic field- and temperature-dependence are in good agreement with previous measurements on LPE-YIG thin films. Thus, such LPE-YIG samples from Innovent can be used for future magnon transport measurements with on par performance as compared to samples from other sources.

In Section 4.2 we had a look at the modulation of electrical magnon transport measurements in three-strip structures. We investigated the electrical magnon transport measurements as a function of the applied modulator current I_{mod} and observed a linear and quadratic dependence for the low current bias regime. For the critical current regime we observed a deviation from that low current bias regime-fit and used this to define a consistent condition for the critical current and the zero effective damping state. This critical currents showed clear dependence on the used dimensions of the structure and we also observed a magnetic field-dependence that was in good agreement with literature. For some of the measured structures the magnon transport signal as a function of the applied modulator current further showed a clear critical current peak, which lets us extract a second critical current. We used the two determined critcal currents for a fit to the magnon transport for the current range below I_{crit} and observed good agreements with the data for both used values for the critical currents. Our obtained results on the modulation of the magnon transport measurements are in good agreement with previous results in literature and further confirm the already for two-strip structures observed good performance of the used LPE-YIG samples. Moreover we used these measurements as a precharacterization for the simultaneous BLS and magnon transport measurements.

We described these electrical magnon transport measurements with simultaneous measurements on a microfocused BLS setup on three-strip structures in Section 4.3. The main achievement of these measurements was the realization of the simlutaneous optical and electrical detection of the zero effective magnon damping state in cooperation with the AG Weiler of the RPTU Kaiserslautern. The implementation was challenging due to the two separate setups which had to be combined in a practical and functional way. We showed that the modulator current of the observed peak in the microfocused BLS spectrum fits the electrical critical current very well. Above this critical current we observed a shift in frequency for the magnon peak in the BLS spectrum and also for the electrical magnon transport signal we observe a further increasing evolution and above a certain modulator current the signal starts to decrease. The magnon peaks in the BLS spectrum and therefore the critical currents extracted from this optical measurements further show a magnetic field-dependence that is in good agreement with a theoretical fit taken from literature, which shows that the observed magnon peaks result from the zero effective damping state as expected. After the BLS measurements we also discussed the impact of the laser illumination in combination with the applied modulator currents on the performance of our structure over time by comparing the electrical magnon transport signal before we conducted the microfocused BLS measurements and afterwards. Before the laser exposure we observed clear critical current peaks in the electrical magnon transport signal that disappear for the measurements conducted afterwards, but for the low current bias regime we can still observe the linear and quadratic dependence on the modulator current. We further observe a reduced modulation efficiency. The discussed degradation after laser illumination and simultaneously applied high modulator currents is caused by increased temperatures. Applying high modulator currents leads to smaller magnon transport signals and for a certain high modulator current we furthermore reach the Curie temperature in YIG, where a magnetic phase transition takes place and the magnon transport signal is vanishing.

With this thesis we could show that our $22\,\mathrm{nm}$ LPE-YIG from Innovent, which was used for the first time for this kind of magnon transport measurements on two- and three-strip structures, provides comparable results with respect to similar YIG thin films grown by different growth methods and can be used for future measurements. We as well successfully investigated the modulation of electrical magnon transport and the zero effective magnon damping simultaneously via lock-in detection and microfocused BLS, which is quite promising for future studies and opens a new field of experiments, which are covered partially in the upcoming outlook.

6 Outlook

After this thesis there are still a lot of open possibilities to conduct further experiments based on the ones investigated here. We want to give a short outlook on some ideas that can be implemented in the future.

As already mentioned in Section 4.1 we observed two distance regimes for the thermal magnon transport amplitude and can therefore also extract two different magnon decay length from the data corresponding to the small and large distance regime. Within this thesis we only measured edge-to-edge distances between injector and detector up to $d = 3.5\,\mu\mathrm{m}$, while the large distance regime we observed started not before $d = 2\,\mu\mathrm{m}$ we could only utilize three distances to extract the magnon decay length. Other groups for example in Refs. [7, 16] conducted experiments with much larger distances up to $d = 20\,\mu\mathrm{m}$ and even $d = 40\,\mu\mathrm{m}$. So for a more detailed analysis especially of the thermal magnon transport signal in our $22\,\mathrm{nm}$ LPE-YIG thin film, more and larger distances can be measured. Which will also lead to a more detailed characterization of the Innovent sample. The dimensions of the YIG thin film can also be changed. We may reduce the dimensionality by using smaller thicknesses of YIG [61], which would have an impact on several paramters like the magnon decay length λ_m or spin pumping contribution and further the temperature-dependence of the magnon transport signal.

For further measurements on three-strip structures related to our measurements in this thesis we can conduct the simultaneous electrical magnon transport and optical microfocused BLS measurements on more structures with different modulator widths w_m and varying distances between the injector and detector electrode d. Due to the limited time at the BLS setup at the RPTU Kaiserslautern and some problems with synchronizing of our two measurement techniques it wasn't possible to include simultaneous measurements on different structures. With that we could investigate the impact of different device geometries on the magnon peak in the BLS spectrum and may reproduce the structure dependence of the electrical critical current we showed in Section 4.2 for the optical critical current. Due to the good agreement of the optical critical currents in Section 4.3 with the theoretical prediction in literature [4] this measurements seem to be promising.

In Section 4.3 we limited our measurements on a fixed laser spot position beneath the modulator. The moveable stage of the used microfocused BLS (see Fig. 3.8) also allows spatially resolved measurements. We can measure the BLS spectrum along the modulator electrode and investigate how the BLS intensity changes along the modulator strip. We can make an analogous measurement and analysis transverse to the modulator. This is a common method for BLS measurements and was also used in Refs. [17, 18] we compared our results to. Spatially resolved measurements would help us to get a deeper understanding on the zero effective damping state [4]. Up to now we just analysed the critical current which indicates the zero effective damping state, the magnetic field-dependence of this critical current and the frequency shift for increasing modulator currents. With the local resolution we can determine the area of the zero effective damping, analyse the change in the magnon density as a function of the spatial position. We further can have a look at the injector and detector strip and investigate the magnon population beneath the electrodes.

We can also think of using NV^- magnetometry instead of microfocused BLS experiments for spatially resolved measurements [62]. NV^- stands for "negatively charged nitrogen-vacancy" (NV^-) that are color centers in diamond. The NV^- magnetometry is based on the interaction between the NV center in the diamond and the surrounding magnetic field, it can be used for imaging of weak magnetic fields [63] at nanometer-scale spatial resolution [64]. In more detail, the NV^- forms a spin triplet which is splitted by the crystal field and we get the two states $m_\mathrm{s} = \pm 1$ and $m_\mathrm{s} = 0$. The spin states are further quantized along the symmetry axis of the NV^-. The $m_\mathrm{s} = \pm 1$ state experiences due to an external magnetic field an energy splitting. This splitting can be controlled via resonant microwave pulses . The spin states can further be read out optically using the difference on flourescence because for electrons with $m_\mathrm{s} = \pm 1$ the photoluminescence is lower than for $m_\mathrm{s} = 0$ [62, 65]. NV^- magnetometry in contrast to BLS detects the magnetic stray fields generated by magnons [62]. In Ref. [66] the NV^- magnetometry was used for detecting spin waves. This was realized by a diamond chip placed on the YIG thin film, with an average distance of $\approx 1\,\mu\mathrm{m}$ in between. The microwave excited spin waves in the YIG could then be detected via photoluminescence when its frequency coincides to a electron spin resonance frequency of the NV. This kind of measurements of the magnon transport could also be made with our LPE-YIG thin films.

In our simultaneous optical and electrical measurements we further had a fixed magnetic field direction. It would also be interesting to have a look at the magnons especially beneath the modulator and further also the two other electrodes not only with respect to the applied modulator current but also with respect to magnetic field orientation and repeat the measurement shown in Fig. 4.11 with microfocused BLS while simultaneously measuring the electrical magnon transport signal. For a realization of this rotation measurement we would have to think about a different kind of installation. Although the used microfocused BLS at the RPTU Kaiserslautern has a rotational stage we would need a different realization of the lock-in measurements. The poles of the magnet are mounted at a certain fixed position and because our sample holder has to be connected via a cable to a breakout box (see Fig. 3.10(c)) and further the sampleholder itself is quite big compared to the components of the rotational stage we can not realize angle dependent electrical magnon transport measurements without a reconstruction.

Structuring the YIG itself would give us the possibility to further investigate the magnon transport and the zero effective damping state. This can be realized by argon ion milling [67] after the fabrication steps described in Section 3.1. For that a resist is applied where the material should stay and a RF or DC ion source is used to generate an Ar ion beam that is then used to etch the unprotected areas of the thin film. Fig. 6.1 shows a possible layout of this structured YIG for two- and three-strip structures.

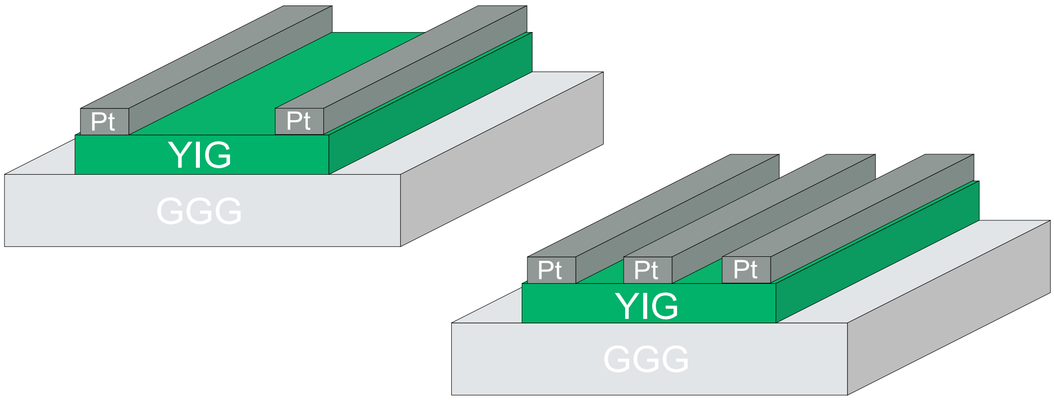

Figure 6.1: Illustration of sample with a two-strip and a three-strip structure with argon milled YIG.

What happens if the magnons are trapped within the "YIG-hills" separated by a trench within the electrode strips or around the whole structure? We would expect the magnons beneath the injector to diffuse in all direction so will the magnon density and with that the detected electrical magnon transport signal increase.

As a last idea for future measurements one can also think of using a different material than YIG for the same measurements. This material would need some preconditions that have to be fulfilled for comparable results. The damping compensation needs to be reached, we would probably keep Pt as the used NM attached on a certain material, because it is necessary to generate a spin current that is large enough for magnon transport measurements, further the magnon linewidth of the MOI should not be too large in order to keep the required critical current for damping compensation low enough and prevent burning of the Pt-strip. A problem of finding an alternative material in thin film form similar in performance as YIG is the lattice mismatch to the substrate that is often not good enough. A possible material, that is already used for magnon transport is the antiferromagnetic insulator hematite (αFe_2O_3) [14, 68]. Yet, the antiferromagnetic nature and changes in the magnonic properties by magnetic anisotropy provide several obstacles to overcome in these experiments.

In conclusion, the characterization of the $22\,\mathrm{nm}$ LPE-YIG film with respect to electrical magnon transport in two-strip structures and simultaneous electrical and optical modulation of magnon transport measurement conducted in this thesis are a solid foundation for further, more detailed and modified measurements in the future.

A Appendix

$\mu_0 H$ (T)	SMR $d_m = 3\,\mu m$	SMR $d_m = 3.5\,\mu m$
1	$(5.48 \pm 0.13) \cdot 10^{-4}$	$(6.77 \pm 1.01) \cdot 10^{-4}$
0.75	$(5.66 \pm 0.07) \cdot 10^{-4}$	$(6.06 \pm 0.13) \cdot 10^{-4}$
0.5	$(5.81 \pm 0.04) \cdot 10^{-4}$	$(6.06 \pm 0.02) \cdot 10^{-4}$
0.25	$(5.78 \pm 0.04) \cdot 10^{-4}$	$(6.00 \pm 0.04) \cdot 10^{-4}$
0.1	$(5.82 \pm 0.05) \cdot 10^{-4}$	$(6.06 \pm 0, 06) \cdot 10^{-4}$
0.05	$(5.83 \pm 0.08) \cdot 10^{-4}$	$(6.06 \pm 0.08) \cdot 10^{-4}$

Table A.1: Comparison of SMR for $d = 3\,\mu m$ and $d = 3.5\,\mu m$

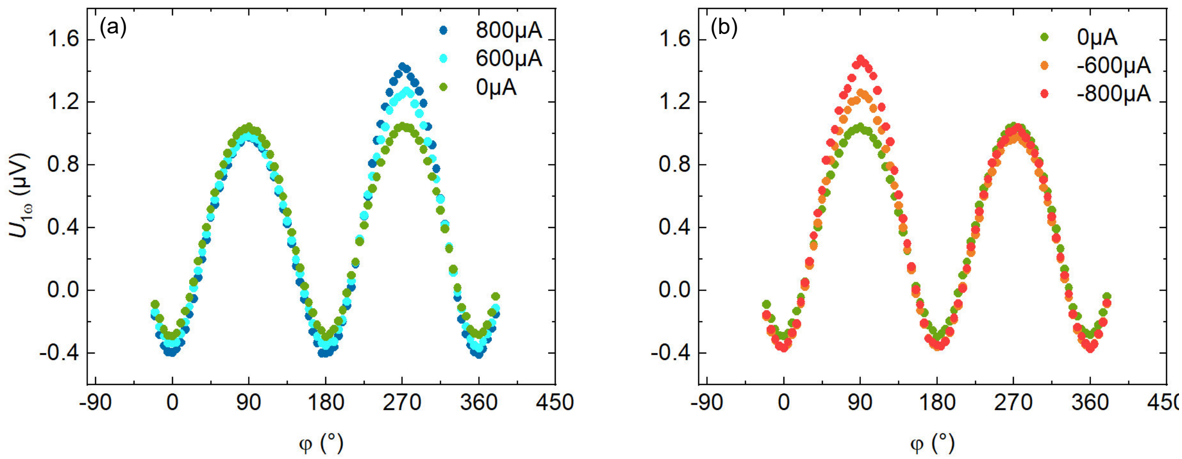

Figure A.1: Electrical magnon transport signal as a function of the magnetic field orientation. The measurements are conducted at a temperature of $T = 280\,K$, a magnetic field of $\mu_0 H = 55\,mT$ for a structure with modulator width $w_m = 600\,nm$ and distance $d_m = 300\,nm$ to the injector and detector electrodes. Modulation of the magnon transport signals via (a) positive charge currents $I_{mod} > 0\,\mu A$ at the modulator and (b) negative charge currents $I_{mod} > 0\,\mu A$ at the modulator.

$\mu_0 H$ (mT)	$A_{1\omega 0}$ (μV)	ΔR_{SHE} (mΩ)	ΔR_{th} ($\frac{\Omega}{A}$)
50	1.842 ± 0.002	0.26 ± 0.01	0.25 ± 0.11
-50	1.842 ± 0.002	-0.26 ± 0.01	0.41 ± 0.10
40	1.860 ± 0.002	0.25 ± 0.01	0.31 ± 0.09
-40	1.856 ± 0.002	-0.26 ± 0.01	0.44 ± 0.09
30	1.88 ± 0.002	0.26 ± 0.01	0.23 ± 0.11
-30	1.88 ± 0.002	-0.26 ± 0.01	0.32 ± 0.11
10	1.90 ± 0.002	0.27 ± 0.01	0.23 ± 0.10
-10	1.894 ± 0.002	-0.28 ± 0.01	0.43 ± 0.11

Table A.2: Extracted parameter from the linear and quadratic fit with Eq. (51) in Fig. 4.12.

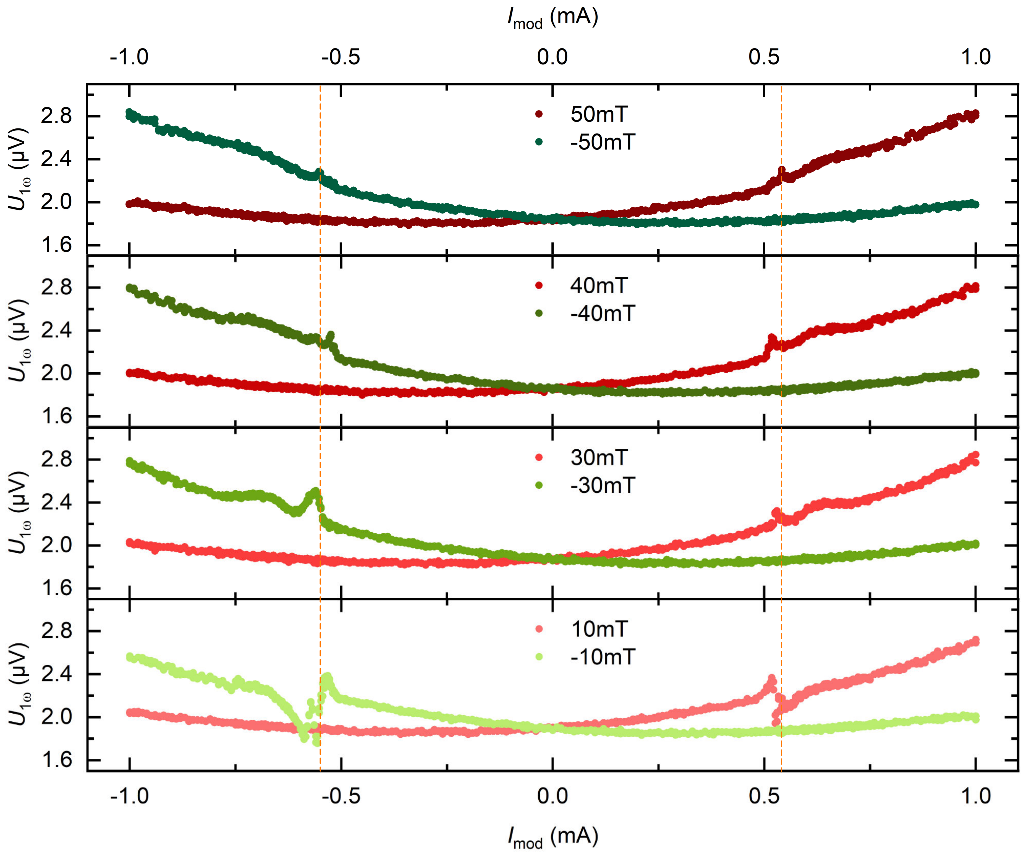

Figure A.2: Electrical magnon transport signal as a function of the applied charge current at the modulator. The measurements are conducted at a temperature of $T = 280\,\mathrm{K}$ for a modulator width of $w_\mathrm{m} = 600\,\mathrm{nm}$ with distance $d_\mathrm{m} = 200\,\mathrm{nm}$ to the injector and detector electrode for different magnetic fields. The peak at $\mu_0 H = 55\,\mathrm{mT}$ is marked for comparison purposes (orange dahed line).

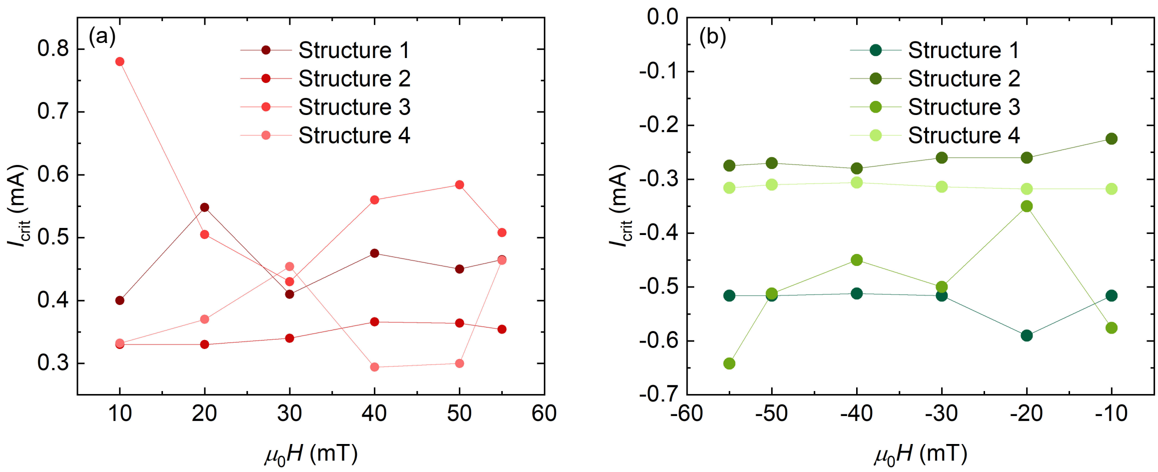

Figure A.3: Critical current as a function of the magnetic field. The measurements are conducted at a temperature of $T = 280\,\mathrm{K}$ for different structures. For more details of the used structures see Tab. 4.1. (a) Critical currents for positive magnetic fields. (b) Critical currents for negative magnetic fields.

$\mu_0 H$ (mT) condition	$\Delta U'$	$\Delta U^0_{\mathrm{mod}}$	I_{crit} (µA)	ΔR_{th}
50	93.12 ± 0.23	0.063 ± 0.001	450	71576.27 ± 1876.78
-50	91.21 ± 0.18	0.057 ± 0.001	-516	58286.17 ± 1168.42
40	90.73 ± 0.31	0.59 ± 0.001	475	59369.30 ± 1677.07
-40	90.46 ± 0.19	0.058 ± 0.001	-512	57655.37 ± 1180.47
30	93.07 ± 0.26	0.071 ± 0.001	410	82130.76 ± 2660.77
-30	89.56 ± 0.18	0.058 ± 0.001	-516	55531.20 ± 1105.06
10	85.46 ± 0.27	0.050 ± 0.001	400	43457.56 ± 891.88
-10	88.58 ± 0.16	0.058 ± 0.001	-516	51598.40 ± 933.51
$\mu_0 H$ (mT) manually	$\Delta U'$	$\Delta U^0_{\mathrm{mod}}$	I_{crit} (µA)	ΔR_{th}
50	88.75 ± 0.15	0.0599 ± 0.0005	542	47339.43 ± 736.93
-50	88.46 ± 0.15	$0.0.0197 \pm 0.0005$	-552	46443.79 ± 760.18
40	89.09 ± 0.18	0.0535 ± 0.0005	518	50702.51 ± 964.37
-40	89.09 ± 0.15	0.0533 ± 0.0006	-524	51625.14 ± 1007.16
30	87.91 ± 0.17	0.0525 ± 0.0005	530	48413.24 ± 879.91
-30	85.58 ± 0.26	0.0468 ± 0.0007	-560	41056.80 ± 1118.71
10	86.29 ± 0.16	0.0524 ± 0.0005	518	47201.88 ± 769.76
-10	86.87 ± 0.16	0.0531 ± 0.0006	-532	45269.66 ± 791.61

Table A.3: Fit parameter for Eq. (53) in Fig. 4.14 due to the condition $\Delta A_{1\omega} > 0.05\,\mu\mathrm{V}$ and manual extraction.

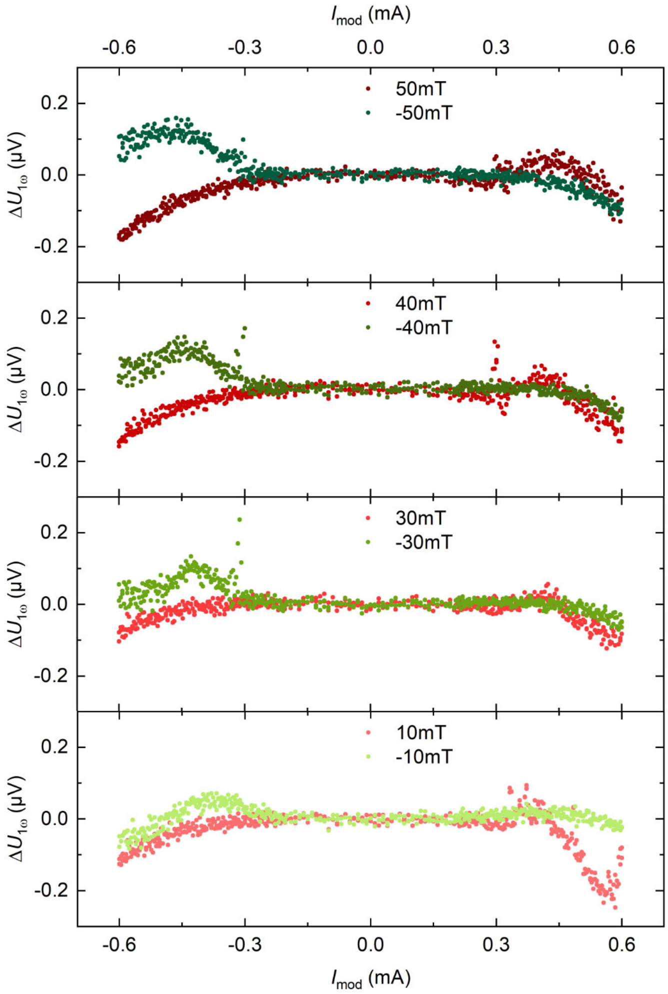

Figure A.4: Difference between the magnon transport signal and the fit with Eq. (51). The measurements are conducted at a termperature of $T = 280\,\mathrm{K}$ for structure 4 (see Tab. 4.1) for different magnetic fields.

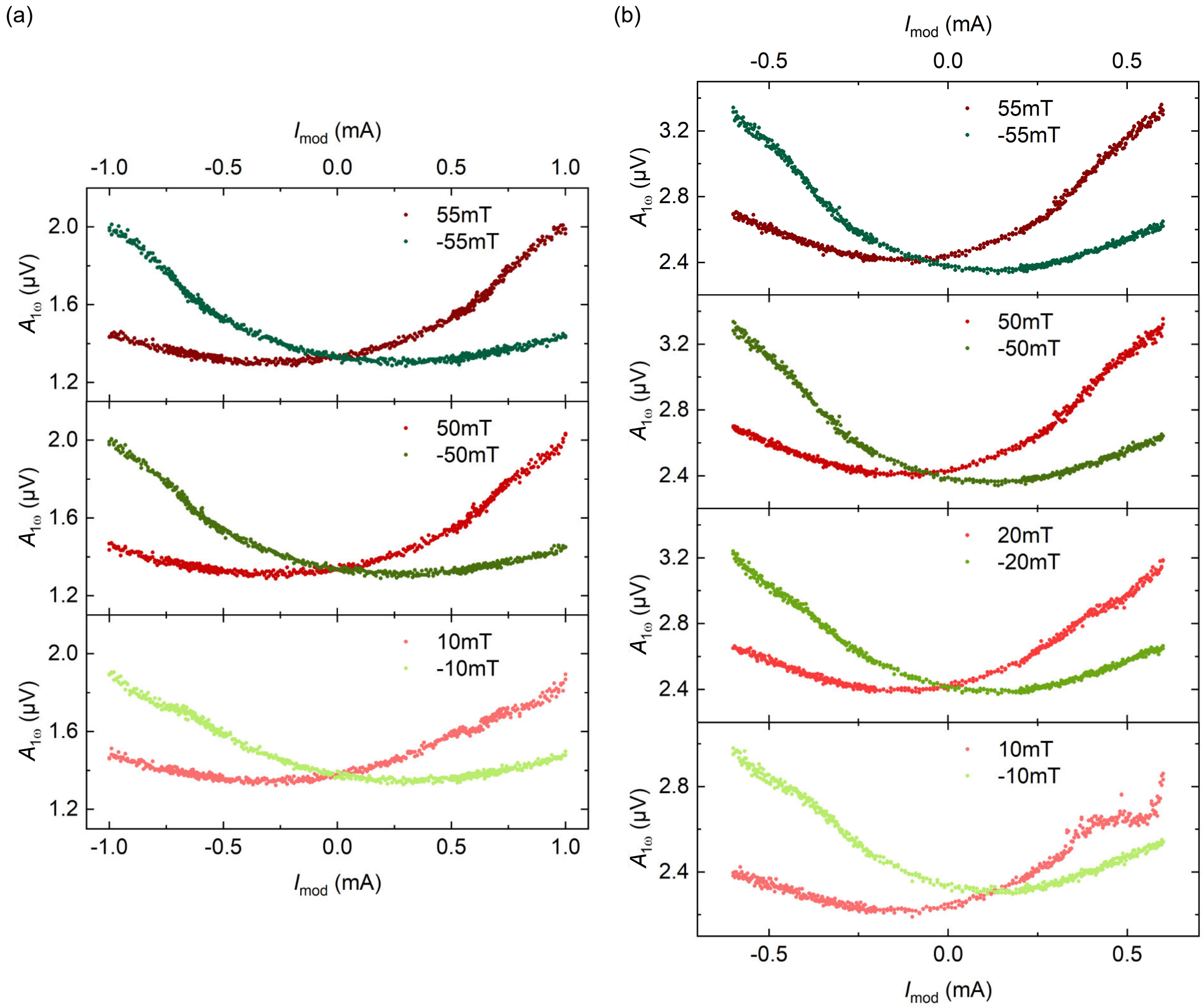

Figure A.5: Electrical magnon transport signal as a function of the modulator current. The measurements are conducted at a temperature of $T = 280\,\mathrm{K}$ for different magnetic fields. (a) Magnon transport signal for structure 3 with a modulator width of $w_\mathrm{m} = 600\,\mathrm{nm}$ and an edge-to-edge distance of $d_\mathrm{m} = 300\,\mathrm{nm}$ between the three electrodes. (b) Magnon transport signal for structure 4 with a modulator of width $w_\mathrm{m} = 300\,\mathrm{nm}$ and distance $d_\mathrm{m} = 350\,\mathrm{nm}$ to injector and detector electrode.

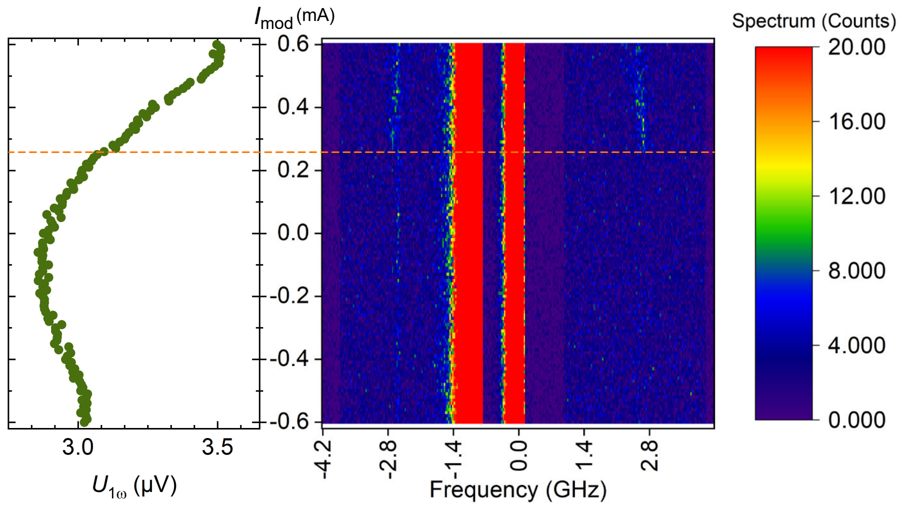

Figure A.6: Modulator current as a function of the electrical magnon transport signal on the left and the BLS spectra for different modulator currents I_{mod} as a function of the frequency on the right. The measurement is conducted on a structure with modulator width $w_{\mathrm{m}} = 300\,\mathrm{nm}$ and an edge-to-edge distance $d_{\mathrm{m}} = 350\,\mathrm{nm}$ between the three electrodes at room temperature at a magnetic field of $\mu_0 H = -40\,\mathrm{mT}$.

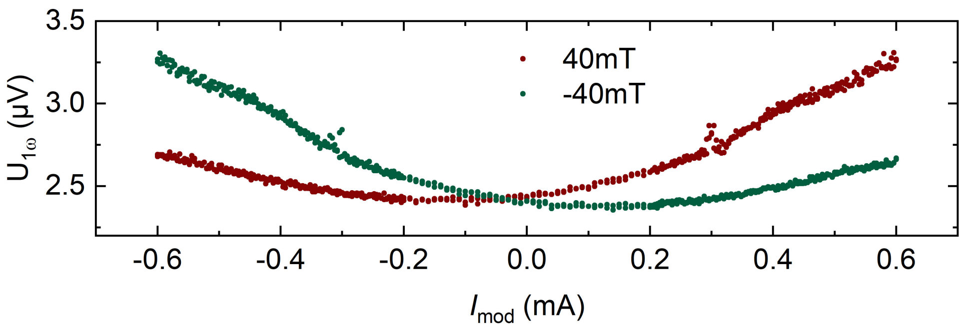

Figure A.7: Electrical magnon transport signal as a function of the applied modulator current. The measurements are conducted at a temperature of $T = 280\,\mathrm{K}$ for a structure with modulator width of $w_{\mathrm{m}} = 300\,\mathrm{nm}$ and a distance $d_{\mathrm{m}} = 350\,\mathrm{nm}$ between the three electrodes and at a magnetic field of $\mu_0 H = \pm 40\,\mathrm{mT}$ (this structure was also used for simultaneous electrical and BLS measurements).

$\mu_0 H$	$A_{1\omega 0}$ (µV)	ΔR_{SHE} (mΩ)	ΔR_{th} ($\frac{\Omega}{A}$)
$55\,\mathrm{mT}$ before	2.388 ± 0.001	0.429 ± 0.007	1.62 ± 0.06
$55\,\mathrm{mT}$ after	2.448 ± 0.002	0.336 ± 0.008	1.18 ± 0.07
$40\,\mathrm{mT}$ before	2.384 ± 0.001	0.430 ± 0.008	1.57 ± 0.07
$40\,\mathrm{mT}$ after	2.458 ± 0.001	0.338 ± 0.008	1.26 ± 0.06
$10\,\mathrm{mT}$ before	2.188 ± 0.002	0.344 ± 0.008	1.11 ± 0.07
$10\,\mathrm{mT}$ after	2.464 ± 0.002	0.326 ± 0.01	1.19 ± 0.08

Table A.4: Extracted parameter from the linear and quadratic fit with Eq. (51) in Fig. 4.20.

References

[1] M. M. WALDROP, Nature , 144 (2016).

[2] N. KIM, T. AUSTIN, D. BAAUW, T. MUDGE, K. FLAUTNER, J. HU, M. IRWIN, M. KANDEMIR, AND V. NARAYANAN, Computer **36**, 68 (2003).

[3] J. PUEBLA, J. KIM, K. KONDOU, AND Y. OTANI, Communications Materials **1**, 2662 (2020).

[4] T. WIMMER, M. ALTHAMMER, L. LIENSBERGER, N. VLIETSTRA, S. GEPRÄGS, M. WEILER, R. GROSS, AND H. HUEBL, Phys. Rev. Lett. **123**, 257201 (2019).

[5] T. WIMMER, Ph.D. thesis, Technische Universität München (2021).

[6] V. CHEREPANOV, I. KOLOKOLOV, AND V. L'VOV, Phys. Rep. **229**, 81 (1993).

[7] L. J. CORNELISSEN, J. LIU, R. A. DUINE, J. B. YOUSSEF, AND B. J. VAN WEES, Nature Physics **11**, 1022 (2015).

[8] S. T. B. GOENNENWEIN, R. SCHLITZ, M. PERNPEINTNER, K. GANZHORN, M. ALTHAMMER, R. GROSS, AND H. HUEBL, Applied Physics Letters **107**, 172405 (2015).

[9] M. DYAKONOV AND V. PEREL, Physics Letters A **35**, 459 (1971).

[10] J. E. HIRSCH, Phys. Rev. Lett. **83**, 1834 (1999).

[11] A. HAMADEH, O. D'ALLIVY KELLY, C. HAHN, H. MELEY, R. BERNARD, A. H. MOLPECERES, V. V. NALETOV, M. VIRET, A. ANANE, V. CROS, S. O. DEMOKRITOV, J. L. PRIETO, M. MUÑOZ, G. DE LOUBENS, AND O. KLEIN, Phys. Rev. Lett. **113**, 197203 (2014).

[12] M. ALTHAMMER, Journal of Physics D: Applied Physics **51**, 313001 (2018).

[13] L. J. CORNELISSEN, J. LIU, B. J. VAN WEES, AND R. A. DUINE, Phys. Rev. Lett. **120**, 097702 (2018).

[14] J. GÜCKELHORN, Ph.D. thesis, Technische Universität München (2023).

[15] J. GÜCKELHORN, T. WIMMER, M. MÜLLER, S. GEPRÄGS, H. HUEBL, R. GROSS, AND M. ALTHAMMER, Phys. Rev. B **104**, L180410 (2021).

[16] J. M. GOMEZ-PEREZ, S. VÉLEZ, L. E. HUESO, AND F. CASANOVA, Phys. Rev. B **101**, 184420 (2020).

[17] B. DIVINSKIY, H. MERBOUCHE, V. E. DEMIDOV, K. O. NIKOLAEV, L. SOUMAH, D. GOUÉRÉ, R. LEBRUN, V. CROS, J. B. YOUSSEF, P. BORTOLOTTI, A. ANANE, AND S. O. DEMOKRITOV, Nature Communications **12**, 2041 (2021).

[18] M. EVELT, L. SOUMAH, A. RINKEVICH, S. DEMOKRITOV, A. ANANE, V. CROS, J. BEN YOUSSEF, G. DE LOUBENS, O. KLEIN, P. BORTOLOTTI, AND V. DEMIDOV, Phys. Rev. Appl. **10**, 041002 (2018).

[19] H. Merbouche, B. Divinskiy, D. Gouéré, R. Lebrun, A. El-Kanj, V. Cros, P. Bortolotti, A. Anane, S. O. Demokritov, and V. E. Demidov, (2023), arXiv:2303.04695 [cond-mat.mes-hall] .

[20] D. J. Lockwood, M. G. Cottam, V. C. Y. So, and R. S. Katiyar, Journal of Physics C: Solid State Physics **17**, 6009 (1984).

[21] J. Li, S. Jin, T. Datta, and D.-X. Yao, Phys. Rev. B **107**, 184402 (2023).

[22] F. D. Czeschka, Ph.D. thesis, Technische Universität München (2011).

[23] T. Wimmer, Master's thesis, Technische Universität München (2016).

[24] E. Karadza, Master's thesis, Technische Universität München (2021).

[25] M. Dyakonov and V. Perel, Soviet Journal of Experimental and Theoretical Physics Letters **13**, 467 (1971).

[26] M. Julliere, Physics Letters A **54**, 225 (1975).

[27] J. Smit, Physica **24**, 39 (1958).

[28] L. Berger, Phys. Rev. B **2**, 4559 (1970).

[29] D. Xiao, M.-C. Chang, and Q. Niu, Rev. Mod. Phys. **82**, 1959 (2010).

[30] P. Jacquod, R. S. Whitney, J. Meair, and M. Büttiker, Phys. Rev. B **86**, 155118 (2012).

[31] S. A. Bender and Y. Tserkovnyak, Phys. Rev. B **91**, 140402 (2015).

[32] B. Cöster, Master's thesis, Technische Universität München (2018).

[33] H. Nakayama, M. Althammer, Y.-T. Chen, K. Uchida, Y. Kajiwara, D. Kikuchi, T. Ohtani, S. Geprägs, M. Opel, S. Takahashi, R. Gross, G. E. W. Bauer, S. T. B. Goennenwein, and E. Saitoh, Phys. Rev. Lett. **110**, 206601 (2013).

[34] Y.-T. Chen, S. Takahashi, H. Nakayama, M. Althammer, S. T. B. Goennenwein, E. Saitoh, and G. E. W. Bauer, Phys. Rev. B **87**, 144411 (2013).

[35] Y.-T. Chen, S. Takahashi, H. Nakayama, M. Althammer, S. T. B. Goennenwein, E. Saitoh, and G. E. W. Bauer, Journal of Physics: Condensed Matter **28**, 103004 (2016).

[36] A. H. e. a. Uchida K., Xiao J., Nature Mater **9**, 894 (2010).

[37] S. M. Rezende, R. L. Rodríguez-Suárez, R. O. Cunha, A. R. Rodrigues, F. L. A. Machado, G. A. Fonseca Guerra, J. C. Lopez Ortiz, and A. Azevedo, Phys. Rev. B **89**, 014416 (2014).

[38] L. J. Cornelissen, K. J. H. Peters, G. E. W. Bauer, R. A. Duine, and B. J. van Wees, Phys. Rev. B **94**, 014412 (2016).

[39] J. Ahopelto, G. Ardila, L. Baldi, F. Balestra, D. Belot, G. Fagas, S. De Gendt, D. Demarchi, M. Fernandez-Bolaños, D. Holden, A. Ionescu, G. Meneghesso, A. Mocuta, M. Pfeffer, R. Popp, E. Sangiorgi, and C. Sotomayor Torres, Solid-State Electronics **155**, 7 (2019), selected Papers from the Future Trends in Microelectronics (FTM-2018) Workshop.

[40] M. Coll, J. Fontcuberta, M. Althammer, M. Bibes, H. Boschker, A. Calleja, G. Cheng, M. Cuoco, R. Dittmann, B. Dkhil, I. El Baggari, M. Fanciulli, I. Fina, E. Fortunato, C. Frontera, S. Fujita, V. Garcia, S. Goennenwein, C.-G. Granqvist, J. Grollier, R. Gross, A. Hagfeldt, G. Herranz, K. Hono, E. Houwman, M. Huijben, A. Kalaboukhov, D. Keeble, G. Koster, L. Kourkoutis, J. Levy, M. Lira-Cantu, J. MacManus-Driscoll, J. Mannhart, R. Martins, S. Menzel, T. Mikolajick, M. Napari, M. Nguyen, G. Niklasson, C. Paillard, S. Panigrahi, G. Rijnders, F. Sánchez, P. Sanchis, S. Sanna, D. Schlom, U. Schroeder, K. Shen, A. Siemon, M. Spreitzer, H. Sukegawa, R. Tamayo, J. van den Brink, N. Pryds, and F. M. Granozio, Applied Surface Science **482**, 1 (2019), roadmap for Oxide Electronics, pushed forward by the TO-BE EU Cost action.

[41] L. Berger, Phys. Rev. B **54**, 9353 (1996).

[42] M. Collet, X. de Milly, O. d'Allivy Kelly, V. V. Naletov, R. Bernard, P. Bortolotti, J. Ben Youssef, V. E. Demidov, S. O. Demokritov, J. L. Prieto, M. Muñoz, V. Cros, A. Anane, G. de Loubens, and O. Klein, Nature Communications **7**, 20411723 (2016).

[43] B. Hillebrands and A. Thiaville, *Spin Dynamics in Confined Magnetic Structures III* (Springer Berlin, Heidelberg, 2006) p. 345.

[44] A. Prabhakar and D. Stancil, *Spin Waves* (Springer New York, NY, 2009) p. 348.

[45] W. Zhang, W. Han, X. Jiang, S.-H. Yang, and S. S. P. Parkin, Nature Physics **11**, 496 (2015).

[46] S. Takei, Phys. Rev. B **100**, 134440 (2019).

[47] J. Gückelhorn, T. Wimmer, S. Geprägs, H. Huebl, R. Gross, and M. Althammer, Applied Physics Letters **117**, 182401 (2020).

[48] L. Brillouin, Ann-Phys **9**, 88122 (1922).

[49] Y. Kunz, Master's thesis, Technische Universität Kaiserslautern (2022).

[50] M. Schneider, Ph.d. thesis, Technische Universität Kaiserslautern (2021).

[51] S. Demokritov, B. Hillebrands, and A. Slavin, Physics Reports **348**, 441 (2001).

[52] M. Merklein, I. V. Kabakova, A. Zarifi, and B. J. Eggleton, Applied Physics Reviews **9**, 041306 (2022).

[53] T. Sebastian, K. Schultheiss, B. Obry, B. Hillebrands, and H. Schultheiss, Frontiers in Physics **3** (2015), doi:10.3389/fphy.2015.00035.

[54] J. Sandercock and W. Wettling, Solid State Communications **13**, 1729 (1973).

[55] R. Mock, B. Hillebrands, and R. Sandercock, Journal of Physics E: Scientific Instruments **20**, 656 (1987).

[56] W. Demtröder, (2014).

[57] M. Althammer, S. Meyer, H. Nakayama, M. Schreier, S. Altmannshofer, M. Weiler, H. Huebl, S. Geprägs, M. Opel, R. Gross, D. Meier, C. Klewe, T. Kuschel, J.-M. Schmalhorst, G. Reiss, L. Shen, A. Gupta, Y.-T. Chen, G. E. W. Bauer, E. Saitoh, and S. T. B. Goennenwein, Phys. Rev. B **87**, 224401 (2013).

[58] X.-Y. Wei, O. A. Santos, C. H. S. Lusero, G. E. W. Bauer, J. Ben Youssef, and B. J. van Wees, Nature Materials **21**, 13521356601 (2022).

[59] J. Shan, L. J. Cornelissen, J. Liu, J. B. Youssef, L. Liang, and B. J. van Wees, Phys. Rev. B **96**, 184427 (2017).

[60] L. J. Cornelissen, J. Shan, and B. J. van Wees, Phys. Rev. B **94**, 180402 (2016).

[61] J. Shan, L. J. Cornelissen, N. Vlietstra, J. Ben Youssef, T. Kuschel, R. A. Duine, and B. J. van Wees, Phys. Rev. B **94**, 174437 (2016).

[62] Y. Xu, W. Zhang, and C. Tian, Photon. Res. **11**, 393 (2023).

[63] L. Rondin, J.-P. Tetienne, T. Hingant, J.-F. Roch, P. Maletinsky, and V. Jacques, Reports on Progress in Physics **77**, 056503 (2014).

[64] M. S. Grinolds, M. Warner, K. De Greve, Y. Dovzhenko, L. Thiel, R. L. Walsworth, S. Hong, P. Maletinsky, and A. Yacoby, Nature Nanotechnology **9**, 279 (2014).

[65] S. Hong, M. S. Grinolds, L. M. Pham, D. Le Sage, L. Luan, R. L. Walsworth, and A. Yacoby, MRS Bulletin **38** (2013), 10.1557/mrs.2013.23.

[66] I. Bertelli, J. J. Carmiggelt, T. Yu, B. G. Simon, C. C. Pothoven, G. E. W. Bauer, Y. M. Blanter, J. Aarts, and T. van der Sar, Science Advances **6**, eabd3556 (2020).

[67] A. Hindmarch, D. Parkes, and A. Rushforth, Vacuum **86**, 1600 (2012), selected papers from the 20th Conference on Ion-Surface Interactions, Zvenigorod, Moscow Region 25 – 29 August 2011.

[68] T. Wimmer, A. Kamra, J. Gückelhorn, M. Opel, S. Geprägs, R. Gross, H. Huebl, and M. Althammer, Phys. Rev. Lett. **125**, 247204 (2020).

Zum Abschluss möchte ich mich noch bei einigen Menschen für das letzte Jahr, das ich in der Magnetiker Gruppe des Walther Meißner Instituts verbringen durfte, bedanken.

- Prof. Dr. Rudolf Gross, vielen Dank für die Möglichkeit diese Arbeit am WMI schreiben zu dürfen.
- Dr. Matthias Althammer, Danke, dass du meine Arbeit betreut hast, dass du mir die Möglichkeit gegeben hast, nach Kaiserslautern zu fahren und mir immer mit Rat und Tat zur Seite gestanden bist. Vielen Dank für deine Hilfe im Labor, deine Geduld mit mir, deine Erklärungen in vielen Gesprächen und Slacknachrichten, deine Unterstützung in Kaiserslautern aus der Ferne über Slack und auch per Videoanruf, deine zahlreichen Korrekturen und gutes Zureden. Ich hätte mir keinen besseren Betreuer wünschen können.
- Dr. Hans Huebl, vielen Dank für deine vielen hilfreichen Anmerkungen und Denkanstöße in Meetings, Seminaren und Gesprächen.
- Dr. Stephan Geprägs, Danke für deine Anregungen im DC-Meeting und in den Seminaren und die netten Gespräche, wenn du deine Masteranden im Büro besucht hast.
- Dr. Matthias Opel, Danke für die Diskussionen und Anregungen im DC Meeting und den Seminaren, die guten Gespräche und dein Vertrauen bei dem Buchorigami für deine Schwester.
- Prof. Dr. Mathias Weiler, Danke, dass ich vier Wochen in Kaiserslautern verbringen durfte und dort an dem BLS-Setup messen durfte und für die vielen Anregungen zu den Messungen.
- Matthias Grammer, Danke, dass du immer versucht hast mit mir eine Lösung zu finden, immer nachgefragt hast, wie es so läuft und Danke, für deine vielen vielen Korrekturen und Unterstützung in der Schreibphase, dass du dich so reingehängt hast, auch wenn du ursprünglich nicht für meine Betreuung zuständig warst und da eher reingerutscht bist. Danke für die vielen witzigen Unterhaltungen.
- Manuel Müller, Danke, dass du dich immer um mich gekümmert hast, auch dann, wenn es gar nicht deine Aufgabe war, dass ich jederzeit zu dir kommen konnte, dass du immer an alles denkst und alles am Laufen hältst, für die vielen witzigen Unterhaltungen, beim Mittagessen, auf der DPG und im Büro.
- Janine Gückelhorn, Danke, dass du mir am Anfang alles gezeigt und erklärt hast, mich mit dem wichtigsten Know-How ausgestattet hast und mir jede Menge Fragen beantwortet hast.
- Niklas Bruckmoser, Danke für deine Einführung ins Bonden, dass ich dich immer um Hilfe bitten konnte, egal ob bei Bonderfragen oder Problemen im Reinraum. Vielen Dank für die Piranha Dips, die du mir gemacht hast und für das Auseinandersägen meiner Probe.

- Korbinian Rubenbauer, Patricia Oehrl, Thomas Luschmann, Danke, dass ihr mich bei meinen vielen Versuchen die Lock-In Messungen zum Laufen zu bringen unterstützt habt.

- Yannik Kunz, Danke, dass du mir das BLS-Setup gezeigt hast, die Messungen mit mir gemacht hast und ich eine so gute Zeit in Kaiserslautern hatte.

- Philipp Schwenke, Danke, dass du dich während meiner Zeit in Kaiserslautern um mich gekümmert hast, mir alles gezeigt hast, mich bei meinen Messungen unterstützt hast, ich bayrisch mit dir reden konnte (zur großen Verwirrung deiner Kollegen) und wir so viel Spaß zusammen hatten.

- Die Werkstatt, die Helium Halle, Andreas Russo, Astrid Habel und Sebastian Kammerer, Danke für eure Unterstützung und jederzeitige, schnelle Hilfe.

- AG Weiler, Danke, dass ihr mich so gut aufgenommen habt und ich eine coole Zeit bei euch hatte.

- Sybilla Plöderl und Maria Botta, Danke für die kleinen Ratschpausen zwischendurch.

- Monika Scheufele, Danke für die immer guten Gespräche zwischendurch, egal ob über Klatsch und Tratsch oder dein gutes Zureden, wenn mal was nicht so gelaufen ist, wie ich es mir vorgestellt habe.

- Franz Weidenhiller, Danke, dass du mich vor allem am Anfang mitgenommen hast und mir die Probenherstellung gezeigt hast und auch danach für Fragen zur Verfügung standest. Richtig schön, dass wir nach unserer gemeinsamen Schulzeit und dem Studium auch noch einen Großteil unserer Masterarbeiten zusammen verbringen konnten, ich hab die Gespräche während der Mittagspausen, im Reinraum, auf der DPG und in unseren Ratschrunden sehr genossen.

- Julian Franz, Danke, dass du immer zur Stelle warst, wenn ich nicht so recht wusste, an wen ich mich wenden soll. Ich hab mich auch immer sehr über deine Besuche gefreut, in denen du mich auf den neuesten Stand zum WMI-Klatsch gebracht hast und mir deine aktuellen Memes gezeigt hast.

- Meine wechselnden Bürokollegen, Lukas Niekamp, Alexander Jung, Christian Mang, Herman Muzychko, Markus Kügle, Sebastiano Covone und Nicolas Jungwirth, Danke für die gute und produktive Büroatmosphäre.

- Simon Gandorfer, Danke für die vielen Bürobesuche und Mittagspausen, bei denen du dafür gesorgt hast, dass wir alle auch irgendwann wieder fertig sind mit Ratschen, dass du dir immer meine Geschichten angehört hast (auch wenns dir der Johannes vielleicht vorher schon in der Kurzfassung erzählt hat) und immer für einen Spaß zu haben bist. Ich werde es sehr vermissen nicht mehr schnell bei dir im Büro vorbeigehen zu können und die Mittagspausen mit dir zu verbringen.

- Johannes Weber, danke für das letzte gemeinsame Jahr, fürs "kurz" Helfen beim Füllen, für die vieeeeeelen Gespräche über unsere Masterarbeiten und Gott und die Welt im

Labor, im Büro, in der Mittagspause, auf der DPG, ... Ich wünsche mir, dass ich in Zukunft so tolle Kolleg*innen wie dich haben werde.

- Meine Freundinnen und Freunde daheim und in der Jugendarbeit, Danke für die schöne Zeit, die wir miteinander haben und die coolen Aktionen, die wir organisieren und die für einen Ausgleich neben der Uni gesorgt haben! Ganz besonders dir, liebe Lena, Danke, dass ich in jeder Lebenslage auf dich zählen kann!

- Meine Schwester Johanna, vielen Dank, dass du die beste Schwester der Welt bist, nicht nur weil du meine private Affinity- und Abbildungs-Hotline bist, auch weil ich dir alles erzählen kann und wir immer füreinander da sind, egal was kommt. Ich hab dich lieb, kleine Schwester und bin sehr stolz auf dich!

- Mein Freund Bene, vielen vielen Dank, dass du in den letzten Jahren immer für mich da warst, mich aufgebaut hast, mich bei allem unterstützt hast und auch zurückgesteckt hast, wenn bei mir Land unter war. Danke, für alles, ich kann mich sehr glücklich schätzen dich an meiner Seite zu haben!

- Meine Familie, Danke Mama und Papa, dass ihr mich immer unterstützt und mir dieses Studium und so vieles andere erst ermöglicht habt, Danke, dass ich immer auf euch zählen kann und mit allem zu euch kommen kann. Liebe Oma, Danke, dass du immer bei allem mitfieberst und mein größter Fan bist. Lieber Opa, ich vermisse dich sehr! Ich weiß, wie stolz du auf mich gewesen wärst und wie gern du im letzten Jahr und noch so viele weitere dabei gewesen wärst. Danke, dass du der coolste und beste Opa auf der ganzen Welt warst und du mir so viel mitgegeben hast.